JOURNAL OF
PETROLOGY

Journal of Petrology, 2018, Vol. 59, No. 1, 11–58
doi: 10.1093/petrology/egy017
Advance Access Publication Date: 16 February 2018
Original Article

OXFORD

Experimentally Derived Intermediate to Silica-rich Arc Magmas by Fractional and Equilibrium Crystallization at 1·0 GPa: an Evaluation of Phase Relationships, Compositions, Liquid Lines of Descent and Oxygen Fugacity

Peter Ulmer[1]*, Ralf Kaegi[1,2] and Othmar Müntener[3]

[1]Institute of Geochemistry and Petrology, ETH, Clausiusstrasse 25, CH-8092 Zurich, Switzerland; [2]Eawag, Swiss Federal Institute of Aquatic Science and Technology, CH-8600 Dübendorf, Switzerland; [3]Institute of Earth Sciences, Géopolis 4897, CH-1015 Lausanne, Switzerland

*Corresponding author. Telephone: +41 44 632 3955. Fax: +41 44 632 1636. E-mail: peter.ulmer@erdw.ethz.ch

Received December 5, 2016; Accepted February 14, 2018

ABSTRACT

Differentiation of hydrous primary, mantle-derived magmas is a fundamental process to generate evolved intermediate to SiO_2-rich compositions forming the bulk of the continental and island arc crust. This study focuses on the results of equilibrium and fractional crystallization experiments at 1·0 GPa using two different primary magmas representing deep (90 km) and shallow (35 km) mantle extraction depths. Experiments on a hydrous high-Mg basalt were conducted at graphite-saturated and more oxidized conditions (NNO to NNO + 2, where NNO is nickel–nickel oxide buffer) to exploit the influence of fO_2 on phase assemblages and the evolution of derivative liquids. The liquid line of descent (LLD) was simulated from liquidus to near-solidus conditions ranging from 1330°C to 720°C. H_2O contents varied from about 2·0 to more than 10 wt %. The LLD covers the entire compositional range from high-Mg basalt to high-silica rhyolite and evolves from metaluminous to peraluminous compositions at 56–60 wt % SiO_2 under oxidizing conditions. The observed crystallization sequences and the LLD reveal contrasting behavior depending on oxidation state, H_2O content and equilibrium versus fractional crystallization. Equilibrium crystallization of high-Mg basalt under reducing conditions is initially dominated by olivine fractionation followed by Cr-rich spinel, clinopyroxene (cpx), and orthopyroxene (opx). Finally, between 1060 and 1000°C, amphibole formed by a peritectic reaction consuming cpx + olivine and forming amphibole + opx, resulting in 16% silica-undersaturated trachy-basaltic liquid. Equilibrium crystallization of the same composition under oxidizing conditions is characterized by strongly enhanced olivine and cpx fractionation and suppression of opx only occurring as a result of the peritectic amphibole-forming reaction at and below 1040°C. The liquid at 980°C is a peraluminous, alkali-poor, high-Al andesite representing ~15% residual liquid. Fractional crystallization of the high-Mg basalt under oxidizing conditions evolves through fractionation of early olivine joined by cpx at 1200°C, followed by opx and hercynitic spinel (1140–1080°C) and amphibole at 1050°C coexisting with cpx (and spinel) to 980°C. At 950°C both garnet and plagioclase (plag) join amphibole as liquidus phases. This paragenesis (plus ilmenite and apatite) persists to 750°C with 16% residual liquid relative to the initial basaltic composition. Liquids evolve continuously from basalt to rhyolite, crossing the metaluminous–peraluminous boundary at about 60 wt % SiO_2. Fractional crystallization of the basaltic andesite starting material differs at high temperature, where opx and cpx are the liquidus phases (1200–1080°C), followed by amphibole at the expense of opx. Below

950°C the phase assemblage is identical except at the lowest temperature (720°C), where quartz saturates in a high-silica rhyolitic liquid representing 20% of the initial basaltic andesite. Liquid compositions of the two starting compositions converge below 950°C, with the exception of K_2O, which behaves incompatibly along the liquid line of descent. The H_2O-undersaturated fractional crystallization experiments on the high-Mg basaltic composition under relatively reducing conditions evolve towards tholeiitic or alkalic compositions owing to early plagioclase (at 1140°C) and abundant opx (at 1110°C) crystallization followed by garnet–cpx–plag–ilmenite at 1080°C. Closed-system equilibrium crystallization under relatively oxidized conditions is characterized by significant expansion of the olivine stability field ($>$250°C, 1280–1000°C) relative to more reducing conditions, causing depletion of the liquid in ferrous iron and increase of ferric iron. The resulting fO_2 of the coexisting basaltic liquids increases by more than 3 log units from about NNO + 2 to NNO + 5·5 over the temperature range $>$1200–1040°C, potentially offering an explanation for the more oxidized character of hydrous arc magmas as opposed to low-H_2O tholeiitic magmas.

Key words: liquid line of descent; equilibrium and fractional crystallization; arc magmatism; lower crustal magma differentiation

INTRODUCTION

The production of magmas at convergent plate margins is an important process forming juvenile island arc and continental crust (e.g. Taylor & White, 1965; Kushiro, 1990; Rudnick, 1995). The formation of intermediate (tonalitic–granodioritic) to granitic rocks forming large batholiths and associated volcanic provinces dominated by intermediate andesite to dacite volcanoes typically occurs in subduction-related settings such as the Patagonian batholith (Chile) (Kay & Ramos, 2006), the Peruvian batholith (Atherton, 1990), the Californian batholith (Lee *et al.*, 2006), the Kohistan batholith (Jagoutz *et al.*, 2009) or, on a smaller scale, the Tertiary Adamello batholith in Northern Italy (Callegari, 1983). A number of processes have been proposed to account for their genesis, including the following: (1) fractional crystallization of mantle-derived basaltic precursors (Bowen, 1928; Cawthorn *et al.*, 1976; Green, 1980; Sisson & Grove, 1993; Grove *et al.*, 2003); (2) additional extensive assimilation of and hybridization with crustally derived partial melts generated by heating of mantle-derived magmas over prolonged time (MASH/FARM) (Hildreth & Moorbath, 1988; Thompson *et al.*, 2002); (3) partial melting of deep crustal lithologies (mafic amphibolites to granulites; e.g. Rapp & Watson, 1995), as well as pelitic micaschists (e.g. Clemens *et al.*, 2011); (4) direct mantle partial melts (andesites; Kushiro, 1974); (5) slab melting (Kay, 1978; Drummond & Defant, 1990). To identify and quantify the relative significance of these processes, phase equilibria constraints, melt fractions and compositions, as well as proportions and compositions of solid residues generated by the proposed endmember processes need to be known. This contribution provides experimental constraints on both the equilibrium and fractional crystallization of primary, mantle-derived, hydrous, arc tholeiitic to calc-alkaline parental melts at pressure conditions corresponding to lower crustal levels (1·0 GPa, 30–35 km). We explored the crystallization-differentiation of two different starting compositions representing variable mantle source extraction conditions—a high-Mg basalt from the Adamello batholith (Italy) (Ulmer, 1988; Hürlimann *et al.*, 2016) and a high-Mg basaltic andesite from Mt Shasta (California) (Baker *et al.*, 1994)—to evaluate the potential influence of the 'mantle input'. Performing both conventional equilibrium and fractional crystallization experiments further allowed us to quantify the relative importance of crystal–liquid separation during crystallization-differentiation. In addition to variable parental magma compositions, we also varied the fO_2 and fH_2O conditions to explore their influence on the liquid lines of descent (LLD). We discuss arguments in favor of, and/or in contradiction to the potential derivation of intermediate silicic magmas by fractional crystallization of precursor basaltic magmas, a subject that is still highly controversial (e.g. Sisson *et al.*, 2005; Clemens *et al.*, 2011; Jagoutz *et al.*, 2011; Melekhova *et al.*, 2013; Keller *et al.*, 2015) but intimately linked to the generation of the continental crust. Our experimental data are relevant for the diversity of magmas fractionating in the lower crust. Upon decompression, these primary magmas will mix in most cases, as is overwhelmingly demonstrated for many arc volcanoes (e.g. Eichelberger, 1975; Hildreth & Moorbath, 1988; and many others). This study provides new experimental data to evaluate the geochemistry and modal proportions of silica-rich magmas generated by equilibrium and fractional crystallization in the lower crust, prior to decompression and mixing in shallow reservoirs. Both geochemically based calculations as well as phase equilibria (experimental and by thermodynamic modeling) constraints imply that in excess of 50% crystallization of ultramafic rocks from initial, mantle-derived magmas must have taken place to produce andesitic liquids at lower crustal conditions (e.g. Arndt & Goldstein, 1989; Kay & Kay, 1991; Müntener & Ulmer, 2006), a hypothesis that is directly tested and quantified by the presented experimental data. The diversity of experimentally derived cumulates and their relevance for the formation of arc lower crust are discussed in Müntener & Ulmer (2018).

EXPERIMENTAL AND ANALYTICAL TECHNIQUES

Experimental strategy

This study encompasses both conventional isobaric equilibrium crystallization as well as isobaric fractional crystallization experiments. Equilibrium crystallization experiments are the classical way to explore the phase relations for a single starting material and involve varying the temperatures from the liquidus down to temperatures where the melt fractions become too small to be measured reliably (e.g. Fig. 1c). Fractional crystallization experiments are very tedious and time consuming, but liquid lines of descent may differ significantly between equilibrium and fractional crystallization. Provided the equilibrium phase diagram is known the LLD can be predicted and calculated, but for hydrous systems involving amphiboles (and potentially micas) phase equilibria are not precisely known and cannot reliably be calculated from thermodynamic data. The details of the procedure to conduct (near) perfect fractional crystallization experiments have been described in previous studies (Villiger *et al.*, 2004; Nandedkar *et al.*, 2014) and are briefly outlined here. The first steps consist of conventional equilibrium experiments conducted with either natural rock powders or synthetic equivalents of primary, hydrous Mg basaltic (Mb) and high-Mg basaltic andesite (ba) magmas to locate the liquidus of the respective composition at 1·0 GPa. Thereafter, the liquid composition coexisting with small to moderate amounts of solid phases was determined by electron probe microanalysis (EPMA), and for any subsequent experiment a new starting material corresponding to the liquid composition of the previous, higher temperature experiment was synthesized. The temperature steps between successive fractional crystallization experiments were mostly 30°C (rarely 50°C). All experiments were evaluated by least-squares regression analysis using the known starting composition and the compositions of all coexisting phases (glass and solid phase) to compute modal proportions, to ensure closed-system behavior, to detect potential disequilibrium, to calculate the correct amount of H_2O to add to the next, lower temperature starting material, and to account for potential alkali deficits in the electron microprobe analyses (mainly caused by Na migration in silicate glasses), and iron loss to noble metal sample containers.

Starting materials

Both natural and synthetic starting materials were employed in this study. Two series of equilibrium crystallization experiments, EQ Mb Pt–C and EQ Mb AuPd, were conducted with a natural high-Mg basalt dyke composition from the southern part of the Tertiary Adamello batholith (RC158c; coordinates 45°57′19·1"N, 10°26′32·5"E; elevation 2366 m); the same was further used as the initial starting composition for two series of fractional crystallization experiments (FC Mb AuPd and FC Mb Pt–C) (Tables 1 and 2). The specific dyke consists of mostly pseudomorphed olivine (Fo 91·1) and clinopyroxene [Mg-number (Mg#) = $Mg/(Mg + Fe_{tot})$ of 0·89] phenocrysts both containing small, idiomorphic Cr-spinel inclusions in a fine-grained matrix composed of amphibole, minor plagioclase and magnetite and some secondary chlorite (Ulmer, 1986). The major element composition is Mg-rich (17 wt % on an anhydrous basis) and rather silica poor (47·4 wt %) and the Fo content and Ni contents of olivine phenocrysts (91·1 and 2800 ppm) and Mg# (0·764), Cr (1240 ppm) and Ni (330 ppm) contents of the whole-rock underline its nature as a primary mantle melt (Hürlimann *et al.*, 2016). The trace element signature clearly reveals the subduction-related provenance (high field strength element depletion; light rare earth element and large ion lithophile element enrichment) of this dyke, which is post-plutonic, cross-cutting the gabbroic to intermediate plutonic rocks of the Southern Adamello batholith (Hürlimann *et al.*, 2016). The original rock powder contains 3·0 ± 0·3 wt % H_2O and 0·05 wt % CO_2 as volatile components. Ulmer (1988) conducted a series of multiple-saturation experiments in graphite–Pt double capsules and established multiply saturated conditions of the high-Mg basalt containing 3·0 ± 0·3 wt % H_2O at 2·8 GPa and 1370°C corresponding to about 90 km depth, where garnet, cpx, opx and olivine join the liquidus within experimental resolution, and identified the melting reaction as peritectic (cpx + gar + opx = ol + liquid). A similar, but less primitive composition (RC156; Hürlimann *et al.*, 2016), an olivine-tholeiite from the same dyke-rock association, has been utilized as starting material for the lower pressure, fractional crystallization experiments at 0·4 and 0·7 GPa (Nandedkar, 2013; Nandedkar *et al.*, 2014) to avoid a large number of experiments that solely crystallize olivine. However, the two compositions RC158c and RC156 are part of the same dyke generation and are directly linked by *c.* 15% olivine fractionation.

An additional series of fractional crystallization experiments were conducted on a primary, mantle-derived, high-Mg basaltic andesite from Mt Shasta (85-44; Baker *et al.*, 1994) with a Mg# of 0·70, olivine phenocrysts with Fo > 90 but higher SiO_2 (52·3 wt %) and lower MgO (10·4 wt %) contents than the high-Mg basalt; 85-44 is multiply saturated with olivine, cpx and opx at 1·0 GPa, with H_2O contents in excess of 3 wt % but less than 6 wt % and a temperature between 1200 and 1270°C (Baker *et al.*, 1994). This composition thus represents a shallow endmember of mantle-extraction depths just beneath a relatively thin continental or juvenile island arc crust (30 km) to investigate the potential influence of the primary magma compositions typically encountered in suprasubduction settings. The crystallization behavior of the same composition was already studied experimentally by Müntener *et al.* (2001)

Table 1: Composition of starting materials (in wt %)

Starting material	SiO_2	TiO_2	Al_2O_3	Cr_2O_3	Fe_2O_3	FeO	MnO	MgO	NiO	CaO	Na_2O	K_2O	P_2O_5	H_2O	Total	ΔNNO	x_{Mg}/x_{An}
FC ba AuPd																	
85-44	52·34	0·64	15·80		1·33	6·75	0·19	10·42		9·91	2·22	0·40		5·00	100·00	–0·12	0·700
F1b	52·07	0·65	15·67		1·47	7·51	0·15	9·60		10·16	2·32	0·41		5·12	100·00	–0·20	0·660
F2b	53·24	0·71	16·40		1·60	6·45	0·20	8·16		10·31	2·46	0·47		5·55	100·00	0·30	0·648
F3b	54·40	0·75	17·07		1·51	5·70	0·18	7·23		10·04	2·61	0·51		5·85	100·00	0·40	0·646
F4b	54·10	0·84	18·13		1·51	5·35	0·19	6·72		9·70	2·82	0·64		6·20	100·00	0·45	0·641
F5b	55·19	0·93	19·75		1·36	5·02	0·19	5·00		8·70	3·13	0·73		7·08	100·00	0·40	0·588
F6b	55·17	0·90	19·89		1·53	5·51	0·22	4·20		8·72	3·11	0·76		7·26	100·00	0·40	0·521
F7b	56·73	0·91	19·18		1·54	5·44	0·23	3·40		8·60	3·16	0·81		7·68	100·00	0·40	0·470
990 ba	55·71	0·90	20·26		1·54	5·35	0·23	3·38		8·46	3·19	0·80	0·18	8·50	100·00	0·00	0·472
950 ba	57·42	0·76	20·46		1·36	5·16	0·23	2·30		8·09	3·20	0·82	0·20	9·00	100·00	0·00	0·390
900 ba	62·19	0·52	19·79		1·03	3·48	0·13	1·06		6·79	3·70	1·05	0·27	9·50	100·01	0·00	0·300
850 ba	65·78	0·51	18·49		0·84	2·55	0·12	0·68		5·55	4·10	1·22	0·15	8·97	100·00	0·00	0·270
800 ba	70·73	0·19	16·83		0·57	1·50	0·11	0·40		3·71	4·20	1·61	0·16	8·24	100·01	0·00	0·262
EQ Mb Pt–C/EQ Mb AuPd																	
RC158c	47·41	0·72	12·80	0·16	3·25	6·44	0·19	17·04	0·04	10·33	1·22	0·40		3·0 (3)	100·00		0·764
FC Mb Pt–C																	
F1	48·59	0·91	15·59		0·00	9·04	0·15	11·01		12·68	1·53	0·51		3·17	100·01		0·685
F2	48·53	1·14	17·87		0·00	9·91	0·18	8·17		11·39	2·06	0·74		4·00	99·99		0·595
F3	48·44	1·19	18·65		0·00	10·24	0·18	7·57		10·74	2·18	0·80		4·32	99·99		0·568
F4	49·56	1·43	19·15		0·00	11·07	0·23	5·78		8·97	2·67	1·13		5·18	99·99		0·482
F5	49·94	2·18	17·78		0·00	14·31	0·33	3·47		6·90	3·29	1·79		10·65	99·99		0·302
FC Mb AuPd																	
F1a	47·65	0·86	14·01		1·69	8·61	0·18	13·30		11·86	1·38	0·48		2·91	100·00	–0·17	0·701
F2a	47·39	0·64	15·21		1·71	8·23	0·22	11·24		13·41	1·38	0·58		3·13	100·00	–0·28	0·672
F3a	47·54	0·76	17·62		2·00	7·87	0·22	9·50		12·08	1·63	0·79		3·85	100·00	0·34	0·637
F4a	47·96	0·86	18·47		2·07	8·35	0·25	8·05		11·15	1·86	0·98		4·27	100·00	0·31	0·584
F5a	50·70	0·93	19·49		1·84	7·79	0·24	6·11		9·42	2·33	1·15		5·92	100·00	0·23	0·535
F5a	51·09	0·94	18·26		1·99	8·32	0·24	6·15		9·50	2·35	1·17		5·92	100·01	0·23	0·520
F6a	53·17	1·00	18·87		1·95	7·47	0·33	4·77		8·56	2·64	1·25		6·95	100·00	0·35	0·480
F7a	55·81	1·03	18·19		1·97	7·44	0·32	3·41		7·63	2·84	1·35		7·64	99·99	0·38	0·398
F8a	58·55	0·97	16·87		1·83	6·29	0·32	3·02		7·61	3·02	1·52		8·14	100·00	0·39	0·404
990 Mb	57·17	0·95	18·74		1·69	6·17	0·31	2·94		7·39	2·95	1·47	0·21	7·46	99·99	0·00	0·405
950 Mb	58·10	0·88	18·98		1·54	5·93	0·29	2·40		7·14	2·99	1·52	0·23	7·80	100·00	0·00	0·369
900 Mb	63·53	0·51	18·94		0·97	3·27	0·14	0·99		6·08	3·39	1·90	0·29	9·15	100·01	0·00	0·299
850 Mb	66·32	0·48	18·31		0·78	2·32	0·09	0·55		5·25	3·66	2·10	0·15	8·88	100·00	0·00	0·244
800 Mb	70·39	0·21	16·78		0·54	1·45	0·09	0·37		3·58	3·80	2·69	0·10	8·21	100·00	0·00	0·254
Seed crystals																	
Plag (nom.)	44·40		35·83							19·20	0·54	0·03			100·00		0·952
Plag (EPMA)	44·70	0·04	36·12			0·64		0·10		19·66	0·60	0·01			101·85		0·948
Garnet (nom.)	37·82	0·05	19·34			37·12	1·55	2·80		0·99					99·67		0·119
Garnet (EPMA)	37·49	0·05	21·80			36·29	1·85	2·88		0·98					101·34		0·124

ΔNNO = log fO_2 – log fO_2(Ni–NiO) at run conditions (Table 2) calculated for the Fe_2O_3/FeO ratio of the starting material. x_{Mg}, Mg-number or Mg# = molar [MgO/(MgO + FeO)]; all Fe as Fe^{2+}; x_{An} applies to plagioclase seed crystals and x_{An} = molar Ca/(Ca + Na + K). RC158c is a natural hydrous high-Mg basalt (Ulmer, 1988); 85-44 is a synthetic analogue of a high-Mg basaltic-andesite (Baker *et al.*, 1994). Plag (nom.), nominal composition of plag crystals from Miyake-Jima volcano (Amma-Miyasaka & Nakagawa, 2002) used as seed crystals (1 wt %) in starting materials 950–800 Mb and ba. Plag (EPMA), average composition of cores of plag crystals in experiments containing plag seed crystals. Garnet (nom.), nominal composition of garnet crystals from Nijar (El Hoyazo volcanic complex, Spain; Munoz-Espadas *et al.*, 2000) used as seed crystals (1 wt %) in starting 990–800 Mb and ba. Garnet (EPMA), average composition of cores of garnet crystals in experiments containing garnet seed crystals.

Table 2: Experimental run conditions

Run no.	*T* (°C)	Starting material	Time (h)	H_2O(n) (wt %)	H_2O(R) (wt %)	Log fO_2 ΔNNO	fO_2 ΔNNO	Capsule(s) (inner/outer)	ΔFe (%)	Run products	Phase proportions (wt %)	$\sum R^2$	*F* rel. (wt %)
Fractional crystallization 85-44 AuPd capsules (FC ba AuPd)													
rk48	1230	85-44	24·0	5·0	4·4 (3)	–0·10		A_5Pd_5/A_5Pd_5	–6·9	liq	100	0·10	100·0
rk50	1200	85-44	24·0	5·1	n.a.	–0·13		A_9Pd_1/A_5Pd_5	–6·0	liq, opx	97·8(6), 2·2(5)	0·11	97·8 (6)
rk56	1170	F1b	29·0	5·6	n.a.	–0·19		A_9Pd_1/A_5Pd_5	6·5	liq, cpx, opx	91·8(9), 3·5(12), 4·7(8)	0·12	89·8 (11)
rk60	1140	F2b	51·0	5·8	n.a.	0·30		A_9Pd_1/A_5Pd_5	1·2	liq, cpx, opx	95·0(12), 3·4(15), 1·6(11)	0·22	85·3 (15)
rk63	1110	F3b	72·0	6·2	n.a.	0·40		A_9Pd_1/A_5Pd_5	6·8	liq, cpx, opx	94·2(8), 4·9(11), 0·9(8)	0·14	80·3 (14)
rk66	1080	F4b	100·0	7·1	n.a.	0·45		A_9Pd_1/A_5Pd_5	–3·2	liq, cpx, opx	87·4(5), 9·9(7), 2·7(5)	0·05	70·2 (9)
rk69	1050	F5b	113·0	7·6	n.a.	0·40		A_9Pd_1/A_5Pd_5	–12·5	liq, cpx, amp	92·7(3), 1·2(4), 6·2(7)	0·10	65·0 (6)
rk70	1020	F6b	126·0	7·8	n.a.	0·40		A_9Pd_1/A_5Pd_5	–2·0	liq, cpx, amp	92·7(11), 0·6(12), 6·7(21)	0·10	60·3 (11)
rk71	990	F7b	150·0	8·6	n.a.	0·40		A_9Pd_1/A_5Pd_5	3·2	liq, cpx, amp	88·6(12), 1·5(15), 10·0(24)	0·20	53·4 (15)
PU1049	990	990 ba	67·0	8·5	10·2 (4)	0·00		Au	1·9	liq, amp, mag	99·0 (8), 0·9 (6), 0·1 (1)	0·40	59·7 (14)
PU1070	980	990 ba	67·5	8·5	9·7 (2)	0·00		Au/Au	11·0	liq, amp	98·2(10), 1·8(10)	0·14	59·2 (15)
PU1062	950	990 ba	48·0	8·5	9·1 (3)	0·00		Au/Au	14·0	liq, amp, (gar), (plg)	90·7(20), 9·3(28), tr., tr.	0·51	54·7 (22)
PU1064	900	950 ba	70·0	9·0	10·2 (2)	0·00		Au/Au	0·9	liq, amp, gar, plg, ilm	76·5(12), 10·4(28), 6·4(23), 6·4(11), 0·3(3)	0·08	41·8 (19)
PU1066	850	900 ba	70·0	9·5	9·5 (3)	0·00		Au/Au	0·0	liq, gar, plg, apa, (ilm)	85·2(9), 6·7/10), 7·8(11), 0·3(3), tr.	0·21	35·6 (14)
PU1068	800	850 ba	114·0	9·0	9·9 (3)	0·00		Au/Au	1·3	liq, amp, gar, plg, ilm, (apa)	75·5(20), 6·7 (33), 0·8(10), 16·6(20), 0·5(4), tr.	0·19	26·9 (21)
PU1072	750	800 ba	144·0	13·2	11·6 (4)	0·00		Au/Au	0·8	liq, plg, mag, apa, (amp, gar)	89·2(7), 9·1(9), 1·3(2), 0·3(2), tr.	0·12	24·0 (19)
PU1072o	720	800 ba	144·0	11·4	11·2 (3)	0·00		Au/Au	0·5	liq, amp, plg, mag, qtz, (apa, gar)	73·1(13), 2·2(4), 20·2(8), 1·2(1), 3·5(6), tr., tr.	0·02	19·7 (20)
Fractional crystallization RC158c AuPd capsules (FC Mb AuPd)													
rk47	1230	RC158c	24·0	2·9	4·2 (2)	2·00	1·5 (3)	A_5Pd_5/A_5Pd_5	–10	liq, ol, sp	89·8(9), 9·3(9), 0·9(4)	0·76	89·8 (9)
rk51	1200	F1a	24·0	3·2	4·3 (2)	–0·17	1·3 (2)	A_9Pd_1/A_5Pd_5	5·0	liq, ol, cpx	92·0(15), 5·2(5), 2·8(15)	0·17	82·6 (17)
rk52	1170	F2a	32·0	3·8	5·2 (2)	–0·18	1·0 (3)	A_9Pd_1/A_5Pd_5	7·6	liq, ol, cpx, (sp)	81·6(37), 2·5(10), 15·9(37), tr.	0·60	67·5 (39)
rk54	1140	F3a	48·0	4·6	n.a.	0·34		A_9Pd_1/A_5Pd_5	–2·6	liq, cpx, sp	84·6(20), 13·8(18), 1·6(6)	0·24	57·1 (37)
rk57	1110	F4a	71·0	5·5	n.a.	0·31		A_9Pd_1/A_5Pd_5	10·5	liq, cpx, opx, sp	76·7(4), 18·8(44), 0·7(2), 3·8(1)	1·18	43·8 (40)
rk58	1080	F5a	100·0	6·7	n.a.	0·23		A_9Pd_1/A_5Pd_5	–1·0	liq, cpx, opx, sp	87·4(22), 9·5(25), 1·7(16), 1·4(5)	0·53	38·3 (39)
rk73	1050	F6a	120·0	7·3	7·3 (3)	0·35		A_9Pd_1/A_5Pd_5	–3·2	liq, cpx, amp	94·9(22), 1·5(23), 3·6(41)	0·35	36·3 (30)
rk 65	1020	F7a	150·0	8·1	n.a.	0·38		A_9Pd_1/A_5Pd_5	0·2	liq, cpx, amp, sp	94·2(14), 2·6(15), 1·5(30), 1·7(3)	0·12	34·2 (25)
rk67	990	F8a	188·0	9·3	n.a.	0·39		Au	0·1	liq, cpx, amp, sp	85·4(9), 6·0(1), 8·3(2), 0·34(26)	0·10	29·2 (15)
PU1048	990	990 Mb	67·0	8·2	8·6 (2)	0·00		Au/Au	21·0	liq, cpx	99·0(10), 1·0(8)	0·69	33·9 (17)
PU1069	980	990 Mb	67·5	8·2	8·3 (2)	0·00		Au/Au	9·5	liq, cpx	99·4 (9), 0·6(6)	0·24	34·0 (14)
PU1061	950	990 Mb	48·0	8·6	8·4 (2)	0·00		Au/Au	11·3	liq, amp, (gar), (cpx)	94·4(8), 5·6(11), tr., tr.	0·06	32·0 (13)
PU1063	900	950 Mb	70·0	9·6	8·4 (3)	0·00		Au/Au	0·8	liq, amp, gar, plg, ilm	78·0(9), 12·0(2), 9·3(2), 1·5(9), 0·3(3)	0·09	24·9 (12)
PU1065	850	900 Mb	70·0	10·1	9·3 (3)	0·00		Au/Au Pt	–0·4	liq, gar, plg, apa, (ilm)	90·2(10), 6·0(11), 3·4(11), 0·4(3), tr.	0·24	22·5 (13)
PU1067	800	850 Mb	114·0	10·8	9·8 (5)	0·00		Au/Au	0·8	liq, amp, gar, plg, ilm, (apa)	80·9(15), 5·1(33), 0·8(10), 12·8(15), 0·4(3), tr.	0·14	18·2 (17)
PU1071	750	800 Mb	144·0	12·2	10·9 (2)	0·00		Au/Au	0·7	liq, plg, mag, (gar)	89·9(10), 8·7(13), 1·4(3), tr.	0·22	16·4 (17)
Equilibrium crystallization RC158c AuPd capsules (EQ Mb AuPd)													
PU910	1200	RC158c	3·8	3·6	4·2 (2)		2·1 (2)	A9Pd1/Pt	–6·0	liq, ol, sp	91·9(9), 7·3(7), 0·9(8)	0·50	
PU908	1200	RC158c	6·3	3·7	4·0 (2)		1·3 (2)	A9Pd1/Pt	–8·6	liq, ol, sp	90·1 (7), 9·4(5), 0·6(5)	0·30	
PU926	1160	RC158c	8·0	3·9	4·1 (2)		2·2 (1)	A9Pd1/Pt	–2·6	liq, ol, sp	83·6(5), 16·4(4), 0·1(5)	0·14	
PU899	1160	RC158c	20·0	3·9	n.p.		1·3 (2)	A9Pd1/Pt	–1·7	liq, ol, (cpx)	84·5(9), 15·5(3), tr.	0·08	
PU909	1120	RC158c	41·0	4·0	4·4 (2)		2·9 (1)	A9Pd1/Pt	–8·8	liq, ol, cpx, sp	82·0(6), 16·1(2), 1·1(6), 0·8(4)	0·03	
PU1006	1100	RC158c	6·2	5·1	4·3 (3)		4·1 (4)	A9Pd1	–4·3	liq, ol, cpx, (sp)	64·3(12), 24·4(6), 11·4(15), tr.	0·03	
PU1003	1080	RC158c	10·0	5·2	5·8 (3)		4·4 (3)	A9Pd1	–2·2	liq, ol, cpx, sp	63·4(9), 25·8(4), 10·4(11), 0·3(5)	0·08	
PU1004	1060	RC158c	20·6	6·4	6·0 (4)		5·1 (5)	A9Pd1	2·0	liq, ol, cpx, sp	50·5(15), 25·6(8), 22·6(19), 1·3(7)	0·18	

(continued)

Table 2: Continued

Run no.	*T* (°C)	Starting material	Time (h)	H_2O(n) (wt %)	H_2O(R) (wt %)	Log fO_2 ΔNNO	fO_2 ΔNNO	Capsule(s) (inner/outer)	ΔFe (%)	Run products	Phase proportions (wt %)	$\sum R^2$	*F* rel. (wt %)
PU905	1040	RC158c	65·0	9·5	9·0 (6)		5·3 (2)	A9Pd1/Pt	8·2	liq, ol, cpx, opx, amp, sp	23·5(53), 1·9(30), 14·6(17), 22·1(53), 37·6(64), 0·3(2)	0·02	
PU1005	1000	RC158c	46·3	10·1	8·8 (4)		5·5 (6)	A9Pd1	8·0	liq, ol, cpx, opx, amp, (sp)	20·9(104), 8·4(113), 12·1(22), 11·4(130), 47·2(98), tr.	0·02	
PU906	980	RC158c	67·0	11·5	9·3 (5)			Au/Pt	0·2	liq, cpx, opx, amp, sp	15·2(7), 11·3(10), 21·8 (8), 50·6(22), 1·1(2)	0·06	
Fractional crystallization RC158c graphite–Pt capsules (FC Mb Pt–C)													
rk3	1230	Rc158c	23·0	3·1	3·1 (1)	C–COH		C/Pt	–2·5	liq, ol, sp	82·9(5), 17·1(4), 0·01(1)	0·12	82·9 (5)
rk6	1200	F1	87·0	4·1	2·6 (2)	C–COH		C/Pt	–3·6	liq, ol, cpx	78·6(12), 3·2(5), 18·2(13)	0·11	65·2 (13)
rk11	1170	F2	72·0	4·4	2·6 (2)	C–COH		C/Pt	5·8	liq, cpx	91·5(4), 8·5(4)	0·02	59·6 (12)
rk13	1140	F3	60·0	5·8	n.a.	C–COH		C/Pt	–0·2	liq, cpx, opx, sp, plg	74·9(23), 19·0(17), 0·1(10), 2·2(6), 3·9(23)	0·01	44·7 (23)
rk55	1110	F4	85·0	9·8	2·5 (2)	C–COH		C/Pt	–7·7	liq, cpx, opx, plg, (sp)	52·7(16), 7·3(11), 14·7(11), 25·4(10), tr.	0·04	23·5 (20)
rk64	1080	F5	120·0	17·6	2·0 (3)	C–COH		C/Pt	–3·6	liq, cpx, plg, ilm, gar	60·5(17), 8·1(8), 11·0(17), 1·2(2), 19·2(14)	0·02	14·2 (20)
Equilibrium crystallization RC158c graphite–Pt capsules (EQ Mb Pt–C)													
PU72	1350	RC158c	4·0	2·8	2·9 (1)	C–COH		C/Pt	11·3	liq	100	0·31	
P1330	1330	RC158c	3·5	2·9	3·2 (1)	C–COH		C/Pt	1·4	liq, ol	98·1(4), 1·9(3)	0·08	
P1301	1300	RC158c	4·3	3·0	3·7(1)	C–COH		C/Pt	2·5	liq, ol	92·2(1), 7·8(1)	0·02	
P1302	1300	RC158c	7·5	2·9	3·4(1)	C–COH		C/Pt	3·0	liq, ol	95·5(4), 4·5(3)	0·10	
P1270	1270	RC158c	10·5	3·0	3·6 (1)	C–COH		C/Pt	1·0	liq, ol	92·7(1), 7·3(1)	0·02	
P1240	1240	RC158c	16·0	3·2	n.a.	C–COH		C/Pt	0·4	liq, ol	88·8(2), 11·2(2)	0·03	
P1210	1210	RC158c	21·7	3·4	3·7(1)	C–COH		C/Pt	0·9	liq, ol, (sp)	83·1(2), 16·9(1), tr	0·03	
P1180	1180	RC158c	25·9	3·7	3·7 (1)	C–COH		C/Pt	0·6	liq, ol, cpx, (sp)	75·0(4), 19·9(2), 5·1(4), tr	0·02	
P1151	1150	RC158c	30·0	3·8	4·4 (2)	C–COH		C/Pt	3·1	liq, ol, cpx, sp	73·1(7), 19·0(2), 7·7(7), 0·2(2)	0·03	
P1152	1150	RC158c	28·8	4·4	n.a.	C–COH		C/Pt	9·5	liq, ol, cpx, sp	63·6(9), 20·5(3), 15·7(10), 0·2(2)	0·06	
P1121	1120	RC158c	50·8	4·6	n.a.	C–COH		C/Pt	12·7	liq, ol, cpx, opx, (sp)	60·6(37), 18·6(33), 18·7(24), 2·2(20), tr	0·39	
P1122	1120	RC158c	99·0	4·7	3·6 (1)	C–COH		C/Pt	20·3	liq, ol, cpx, opx, (sp)	59·8(5), 14·0(4), 17·2(3), 9·0(7), tr.	0·01	
P1090	1090	RC158c	75·0	5·7	4·0 (3)	C–COH		C/Pt	–2·0	liq, ol, cpx, opx, sp	49·4(13), 17·8(11), 25·2(6), 5·4(17), 2·2(1)	0·01	
P1060	1060	RC158c	98·0	10·9	6·7 (2)	C–COH		C/Pt	4·1	liq, ol, cpx, opx, amp, sp	24·9(20), 5·6(17), 38·7(12), 23·0(19), 3·1(31), 4·6(2)	0·01	
P1000	1000	RC158c	211·3	13·6	n.a.	C–COH		C/Pt	5·6	liq, cpx, opx, amp, sp	15·9(2), 27·1(3), 29·1(2), 25·5(8), 2·3(1)	0·01	

Starting materials are given in Table 1. H_2O(n) wt %, H_2O contents in the starting material corrected for melt fraction (*f*) and modal amount of amp (2·1 wt %); H_2O(R) wt %, H_2O content of glasses (liquid) determined by Raman spectroscopy; n.a., experiment charge is no longer available (lost); log fO_2 ΔNNO indicates graphite capsules ≈C–COH (see text), for double-capsule experiments = initial fO_2 constrained by Fe^{3+}/Fe_{tot} of the starting material expressed as difference from the Ni–NiO equilibrium at the same pressure and temperature; fO_2 (ol) (ΔNNO) corresponds to the fO_2 calculated from olivine–liquid Fe^{2+}–Mg partitioning (see text). Capsule(s): C/Pt, graphite container sealed in Pt; A9Pd1/Pt or A5Pd5, Fe-pre-saturated inner $Au_{50}Pd_{50}$ or $Au_{90}Pd_{10}$ capsule (not for Au_{100}) in outer capsule (Pt or $Au_{50}Pd_{50}$) containing same starting material. ΔFe % is the difference between the FeO content of the bulk starting composition and the FeO obtained by mass-balance calculations; negative values indicate relative iron gain in wt %. Phase proportions are given in wt % and were calculated by least-squares regressions; numbers in parentheses indicate standard deviations and read as follows: 98·1(4) = 98·1 ± 0·4; $\sum R^2$ is the sum of the squared residuals; *F* rel. (wt %) is the amount of liquid left in the fractional crystallization experiments relative to the initial starting material (RC158c and 85-44 for Mb and ba runs respectively). Phases: liq, liquid (glass); ol, olivine; cpx, high-Ca clinopyroxene; opx, low-Ca orthopyroxene; sp, Cr–Al–Fe-spinel; ilm, ilmenite; amp, amphibole; gar, garnet, plg, plagioclase, mag, (Ti-)magnetite, apa, apatite, qtz, quartz; phases in parentheses indicate that the phase is present only in trace amounts not quantified during least-squares regression (tr.). All runs were performed at a pressure of 1·0 GPa.

at 1·2 GPa under equilibrium crystallization conditions with three H_2O contents of 2·5, 3·8 and 5·0 wt %. We used 5·0 wt % as the starting composition for the fractional crystallization experiments at 1·0 GPa, allowing comparison of the fractional and equilibrium crystallization experiments but keeping in mind that the pressure is not identical (1·0 versus 1·2 GPa) and the fO_2 conditions might be slightly more reducing in the equilibrium crystallization experiments as these were conducted with Fe-pre-saturated $Au_{80}Pd_{20}$ inner capsules surrounded by graphite contained in an outer Pt capsule.

All starting materials except the natural high-Mg basalt (i.e. initial starting composition RC158c with 3 wt % H_2O) and all liquid compositions from the fractional crystallization experiments that were employed as starting material for the next fractionation experiment (Table 1) were mixed from fired (1000°C: SiO_2, TiO_2, Fe_2O_3, MgO, $CaSiO_3$) and dried (220–350°C: γ-Al_2O_3, $CaCO_3$, MnO, Fe_2SiO_4, $NaSi_2O_7$, $KAlSi_3O_8$/$K_2Si_4O_7$) oxides and silicates and dried mixtures of AlOOH (200°C) and $Al(OH)_3$ and $Mg(OH)_2$ (100°C) to adjust the desired H_2O content. Fayalite (Fe_2SiO_4) was synthesized from reagent grade SiO_2 and Fe_2O_3 in an iron pre-saturated Pt crucible for two times 24 h with intermediate grinding at 1120°C at a log fO_2 of –12·50 (1 log unit above the iron–wüstite equilibrium) in a vertical gas-mixing (CO_2–H_2) quench furnace and checked by powder X-ray diffraction analysis. $KAlSi_3O_8$ (potassium-feldspar) was obtained from a natural K-feldspar (Ba-bearing) that was finely ground and mixed with KCl (ratio KCl:$KAlSi_3O_8$ 10:1) heated to 850°C in a Pt crucible for 48 h, quenched and the KCl washed out with deionized H_2O. This produced nearly pure K-feldspar.

Capsule material and treatment

Graphite–Pt double capsules

Two series of experiments, an equilibrium (EQ Mb Pt–C) and a fractional (FC Mb Pt–C) series starting from the high-Mg basalt RC158c (Table 1), were conducted with graphite–Pt (Pt–C) double capsules, resulting in relatively reducing conditions between the C–CO_2 and the H_2O maximum in the graphite buffered C–O–H system; that is, conditions of 2–3 log units below the Ni–NiO equilibrium (ΔNNO; Ulmer & Luth, 1991; Frost & Wood, 1995). Graphite–Pt double capsules have the advantage that Fe loss is minimal and that, theoretically (see below), volatile loss can be avoided. This was achieved for the equilibrium crystallization experiments, but was not the case for the fractional crystallization experiments, which resulted in H_2O-poor compositions for the latter.

AuPd–Pt and Au/AuPd–Au/AuPd double capsules for fractional crystallization experiments

The two fractional crystallization series (high-Mg basalt starting composition FC Mb AuPd and basaltic andesite starting composition FC ba AuPd) and most equilibrium crystallization experiments on the Mg basalt (EQ Mb AuPd) were conducted in a double capsule, AuPd alloy or Au inner–Pt, AuPd alloy or Au outer capsule arrangement employing $Au_{90}Pd_{10}$ inner capsules (2·3 mm o.d., 0·15 mm wall thickness) except for the two highest temperature experiments (1230°C, rk47 and rk48), which used $Au_{50}Pd_{50}$ inner capsules, and experiments below 1000°C, which used pure Au capsules; the outer capsules were always made of $Au_{50}Pd_{50}$ (4·0 mm o.d., 0·2 mm wall thickness), except below 1000°C, where pure Au was employed. Both capsules contained the same starting material. The inner AuPd capsules (but not the pure Au capsules) were additionally pre-saturated in iron to minimize potential Fe loss using an anhydrous basaltic starting material (F3 for the FC series and RC158c for the EQ series; Table 1) tightly packed into annealed, cleaned and one-side welded capsules that were run for 48 h in a gas-mixing furnace at 1180°C and a log fO_2 of –9·65 corresponding to ΔNNO – 1·7. The recovered capsules were immersed in concentrated HF for 48 h to dissolve the silicate glass and cleaned in an ultrasonic bath using distilled water. This results in negligible Fe and H_2 loss, a prerequisite to maintain nearly constant fO_2 conditions in fluid-undersaturated experiments (Hall *et al.*, 2004; Kägi *et al.*, 2005). Below 990°C the capsule arrangement was modified. A triple-capsule setup was employed with two different inner capsules, one containing the derivative composition of the basaltic andesite parental compositions (denoted ba in Tables 1 and 2) and the other containing the derivative composition of the high-Mg basaltic parental composition (Mb), both packed into an outer Au capsule containing the Mb derivative composition (these compositions are very similar except for some minor differences in CaO and K_2O). Experiments PU1061 and PU1062 contained additionally 1 wt % of An_{95} plagioclase seeds (Table 1; Miyake-Jima volcano, Japan; Amma-Miyasaka & Nakagawa, 2002), experiments PU1063-PU1072 contained 1 wt % each of An_{95} plagioclase and almandine-rich garnet (Table 1; Níjar, southern Spain; Munoz-Espadas *et al.*, 2000) seeds to prevent potential nucleation problems of these two phases and to allow measurement of overgrowth rims on seeds in the case of plagioclase, which otherwise forms very fine platelets that are very difficult to analyze reliably. Runs below 1000°C of this series contained 2 wt % of an additional trace element doped diopside glass providing 40 ppm of 32 trace elements. The addition of the diopside glass was considered calculating the final composition of the respective starting materials. However, no correction was made for the additional seed crystals (plag and garnet) as they were consistently present in the final run products armored by overgrowth rims (see Fig. 2c–f) and, thus, did not significantly contribute to the liquid composition in these experiments.

The situation for the equilibrium crystallization experiments on the high-Mg basalt composition in AuPd alloys (EQ Mb AuPd) was different. Initially, a similar setup to that for the respective fractionation experiments was utilized; that is, iron pre-saturated inner

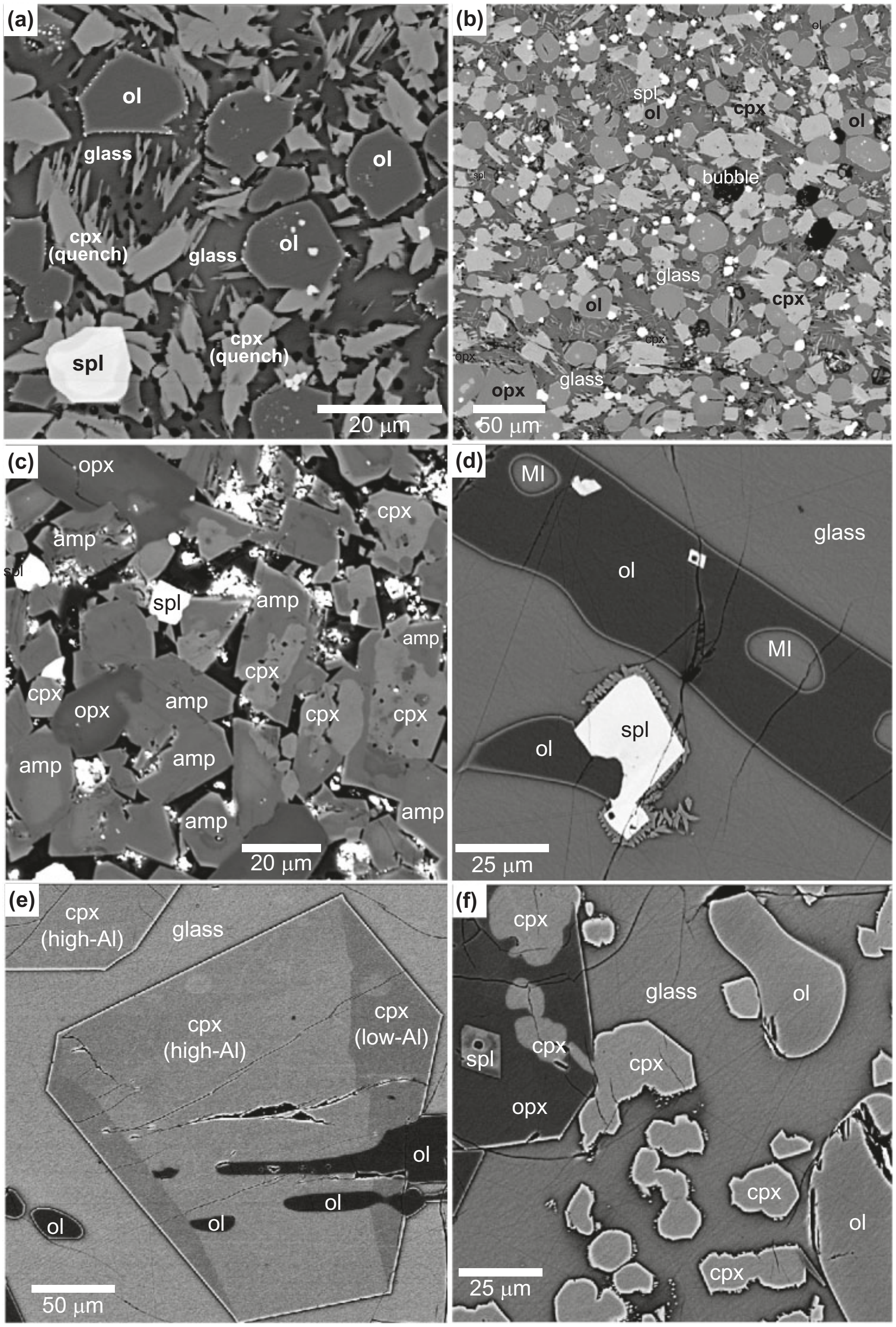

Fig. 1. Back-scattered electron (BSE) images of run charges from equilibrium crystallization experiments on composition RC158c (Mb): (a) run PU926 (1160°C, AuPd capsules) composed of olivine (ol) and zoned Cr-rich spinel (spl) and quench high-Ca clinopyroxene (cpx); (b) run PU905 (1040°C, AuPd capsule) composed of ol, cpx, low-Ca orthopyroxene (opx) and Cr–Al–Fe-rich spinel; (c) run PU906 (980°C, AuPd capsule) showing cpx overgrown by amphibole (amp) coexisting with opx and spl (magnetite); (d) run ZP1210 (1210°C, Pt–C capsules) depicting Cr-rich spinel coexisting with ol that contains melt inclusions (MI); (e) run ZP1180 (1180°C, Pt–C capsules) showing sector-zoned cpx enclosing partly corroded ol; (f) run ZP1090 (1090°C, Pt–C capsules) composed of ol, cpx, opx and Al-rich (hercynitic) spinel; cpx enclosed in opx is resorbed.

capsules and Pt outer capsules. This turned out to be problematic because the natural starting material is rather oxidized, corresponding to an $f\mathrm{O}_2$ at its liquidus (*c.* 1300°C) of NNO + 2. The pre-saturation at NNO – 1·7 resulted in unconstrained conditions owing to the uptake of Fe from the $\mathrm{Au}_{90}\mathrm{Pd}_{10}$ capsule; repeat experiments provided inconsistent phase equilibria and phase proportions. Therefore, we abandoned Fe

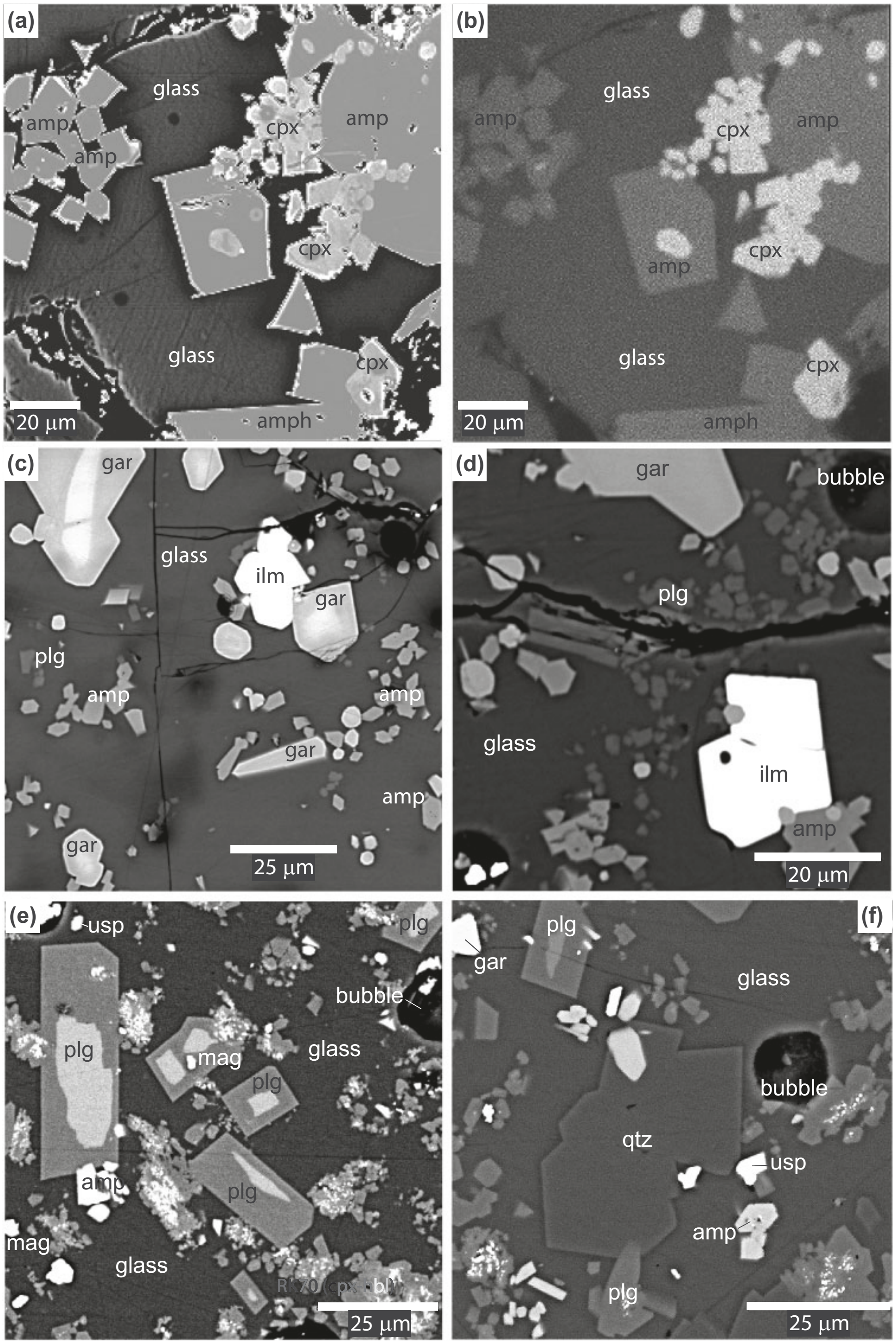

Fig. 2. Back-scattered electron (BSE) images of run charges from fractional crystallization experiments. (a, b) BSE image and Ca–Kα distribution map of run RK70 (1020°C, ba) with high-Ca clinopyroxene (cpx) and amphibole (amp); where cpx is enclosed in amp it shows resorption; (c) BSE image of run PU1063 (950°C, Mb) exhibits garnet (gar) with seed cores (almandine) coexisting with amp, plagioclase (plg) and ilmenite (ilm); (d) BSE image of run PU1064 (900°C, ba) depicting gar, amp, ilm and plag; (e) BSE image of run PU1072 (750°C, ba) showing plg with seed cores (anorthite) coexisting with amp and magnetite (mag); (f) BSE image of the outer capsule of run PU1072o (720°C, ba) containing quartz (qtz) coexisting with plg, amp, ulvöspinel (usp) and unreacted garnet seeds (lacking idiomorphic overgrowth rims).

pre-saturation in this case and changed to untreated inner $Au_{90}Pd_{10}$ capsules, initially in a double-capsule arrangement with Pt outer capsules. This resulted in consistent, reproducible phase equilibria with minimal Fe loss or gain because Fe alloying with Au-dominated AuPd alloy is not a critical issue at oxidizing conditions, unlike under more reducing conditions where even pure Au shows considerable alloying with Fe from basaltic melts (e.g. Ratajeski & Sisson, 1999). A final modification for lower temperature runs was made by employing single $Au_{90}Pd_{10}$ capsules because the employment of double capsules (and MgO ceramic spacers around them) resulted in extensive quench crystallization in the inner capsule owing to decreased quenching rates that basically inhibited successful analysis of the melt phase; using single capsules at low temperature eliminated quench crystallization; the phase relations, however, were identical for double and single capsules at comparable conditions.

For fractional crystallization experiments in AuPd capsules, oxygen fugacity was constrained by adjusting the proportions of ferrous and ferric iron in the starting material to a value close to NNO (NNO – 0·2 to NNO + 0·45) at the conditions of the experiment. The appropriate Fe^{2+}/Fe^{3+} ratio was calculated with the algorithm of Kress & Carmichael (1991). This approach is strictly valid only for charges composed entirely of liquid; therefore, in the present work this is an approximation as the melt fraction (f) varied between unity and 0·75. In the absence of Fe–Ti-oxides, the fO_2 most probably increases in the charges owing to the more incompatible behavior of ferric relative to ferrous iron in the presence of olivine and clinopyroxene, the main liquidus phases at high temperature. At lower temperatures, prediction is more difficult as amphibole can accommodate significant amounts of ferric relative to ferrous iron. However, in these experiments the melt fraction always exceeded 75%; therefore, we do not expect significant deviation from the target fO_2 owing to crystallization of the solid phases. A prerequisite for successful application of this technique is the absence of significant hydrogen and/or iron loss during the experiment (i.e. closed-system behavior). Hydrogen diffusion was minimized by employing the double-capsule technique, packing the same material in the inner and outer capsule and thereby limiting the fH_2 gradient across the inner–outer capsule interface. Fe loss was minimized by using Fe pre-saturated AuPd inner capsules (Kägi *et al.*, 2005) and by minimizing the run duration to the minimum required for close approach to equilibrium (24–188 h).

The situation is different for the 'closed-system' equilibrium crystallization experiments in AuPd capsules: the initial high-Mg basaltic starting material has an Fe^{3+}/Fe_{tot} of 0·31 (molar) that corresponds to a log fO_2 of NNO + 2·0 at its liquidus temperature of *c.* 1300°C. During crystallization down to 1040°C olivine and cpx are the dominant ferro-magnesian phases and only minor Cr-rich spinel crystallized at the highest temperatures. Thus, it is expected that ferrous iron is preferentially extracted by the solid assemblage, resulting in increased Fe^{3+}/Fe_{tot} ratios in the residual liquid and thus resulting in an 'auto-oxidation' of the system with decreasing melt fraction; a result that is clearly supported by the apparent Fe–Mg partitioning between olivine and liquid that decreases with decreasing temperature (see results and discussion sections). Differences of up to 1 log unit in fO_2 were observed at high temperature as a function of the assembly employed: two experiments at 1200 and 1160°C (PU908 and 899) were performed with talc–Pyrex–graphite–Pyrex–BN assemblies that revealed an fO_2 of about 1 log unit more reducing than the experiments conducted at the same conditions with talc–Pyrex–graphite–MgO assemblies that were used for the remainder of this experimental series.

Experimental set-up

Graphite–Pt capsules

The starting materials were dried at 110°C before being loaded into the graphite containers. The graphite capsules were closed with a tight-fitting lid and packed into Pt capsules that additionally contained fine-grained graphite at the bottom and top to prevent cracking of the inner capsule during initial compression in the piston cylinder. The AuPd and Au inner capsules were tightly filled with *c.* 15 mg of starting material, weighed, crimped, cut and welded shut using an arc welder. Sealing of the capsules was checked by weighing before and after welding by submersion in acetone. The same procedure was repeated for the outer capsule containing the inner capsule plus an additional 50 mg of the starting material around the inner capsule. The capsules of all experiments except the graphite–Pt equilibrium experiments on the high-Mg basalt (EQ Mb Pt–C; see below) and runs PU899 and 908 were embedded vertically in MgO-ceramic and contained in a NaCl–Pyrex–graphite–MgO piston cylinder assembly. The capsule was placed in the hotspot of the assembly, which was computed using the numerical model of Hernlund *et al.* (2006). All experiments were performed in 14 mm bore end-loaded piston-cylinder apparatus. A friction correction of –3% was applied to the nominal pressure, based on calibrations employing the fayalite + qtz = orthoferrosilite univariant reaction at 1000°C and 1·41 GPa (Bohlen *et al.*, 1980) and the qtz = coesite transition at 1000°C and 3·07 GPa (Bose & Ganguly, 1995). The temperature was measured with a B-type $Pt_{94}Rh_6$–$Pt_{70}Rh_{30}$ thermocouple, with an estimated accuracy of ±10°C. No corrections for the pressure effect on the electromotive force (e.m.f.) were performed. The experiments were terminated by switching off the power supply, resulting in quenching rates in excess of 100°C s^{-1}. The EQ Mb Pt–C experiments (denoted P1xxx runs in Table 2) and runs PU899 and PU908 were conducted in the same apparatus, but employing BN–crushable alumina–Pyrex inner assembly parts and talc–Pyrex outer parts. The friction correction for this assembly amounts to –10% based on the same calibration reactions. Temperatures in these experiments were measured with S-type Pt–$Pt_{90}Rh_{10}$ thermocouples.

Analytical methods

Recovered charges were embedded in epoxy resin, ground to expose a longitudinal section of the capsule(s) and polished with diamond paste down to 1 μm. For EPMA and scanning electron microscope (SEM) analyses samples were coated with 20 nm of carbon.

Electron probe microanalysis and scanning electron microscopy

Experimental run products were analyzed with three electron microprobes at ETH Zurich using wavelength- (and energy-) dispersive spectrometers (WDS and EDS) on a ARL SEMQ, a CAMECA SX50 and a JEOL JXA-8200. An acceleration voltage of 15 kV and a variable beam current and beam size (7 nA and 10–20 μm for glasses; 20 nA and 1 μm for minerals) were used to minimize alkali-migration during analyses of hydrous glasses. Peak and background counting times were 20–30 s. All data were corrected with either the ZAF (ARL SEMQ) or the PRZ model (Goldstein *et al.*, 2003; Korolyuk *et al.*, 2009). For glasses, H_2O was used as additional element for ZAF or PRZ corrections, and was calculated as difference from 100 wt %. Data are consistent among the three electron microprobes because the same set of standards was employed for all analyses, and several charges have been reanalyzed in later sessions resulting in identical data within statistical error. Additionally, back-scattered electron (BSE) images and characteristic element X-ray maps were acquired with an JEOL JSM-6390LA SEM equipped with a Thermo-Scientific Noran system 7 EDS detector allowing standardized (quantitative) analyses that were particularly useful for checking the Na_2O (and K_2O) contents of hydrous glass with a beam current of 2·4 nA. Modal proportions were calculated using non-weighted, least-squares regression (LSR) analyses implemented in Microsoft EXCEL® 2010 and/or Origin 9.1® balancing the nominal composition of the starting material against the averages of all analyzed phases in the experimental charges (Tables 1–3).

Micro-Raman spectroscopy

The H_2O contents of most recovered experimental glasses were quantified by micro-Raman spectroscopy. Raman scattering was excited using a 514·5 nm diode laser and measured with a Dilor Labram II confocal micro-Raman spectrometer. The laser beam was focused 5 μm below the sample surface with a spot size of 1–2 μm in confocal mode. Spectra were obtained in the 180–1500 and 2800–3900 cm^{-1} ranges to cover low- and high-frequency T–O stretching and vibration modes and the OH/H_2O stretching regions. Two to three spectra were acquired for each measuring point and 3–5 spots were analyzed on each sample. The acquisition time was 120 s. The spectra were processed using Origin 9.1® software employing a cubic baseline correction scheme similar to that of Di Muro *et al.* (2006) and Mercier *et al.* (2009). Quantification was obtained by acquiring Raman spectra of a total of 20 synthetic glasses with known H_2O concentrations (Karl-Fisher titration; KFT) ranging in composition from olivine-tholeiite to rhyolite and H_2O contents from nominally anhydrous to 10 wt %. The relative peak ratios of the OH/H_2O peak(s) to either the low-frequency (LF, 470–510 cm^{-1}) or the high-frequency (HF, 960–1120 cm^{-1}) silicate vibration modes was calibrated as a function of H_2O content and the LF/HF ratio (as a proxy for composition or polymerization of the silicate glass). Two calibration curves were defined, one for the range olivine-tholeiite to andesite and a second for andesite to rhyolite, as no single, straightforward algorithm allowed fitting over the entire compositional range. Accuracy of the method is estimated at ±0·5 wt % H_2O, and results are reported in Table 2.

RESULTS

Experimental conditions, phase assemblages, modes, relative Fe loss, estimated fO_2 conditions and H_2O contents of recovered glasses are presented in Table 2. Average phase compositions with standard deviations are reported in Tables 3 and 4.

General remarks

The experiments reported in this study are equilibrium and fractional crystallization experiments performed over restricted temperature steps of mostly 30°C and 50°C below 1000°C; the equilibrium crystallization experiments under oxidized conditions (EQ Mb AuPd) used step sizes of 40°C with some additional steps between them (20°C) to explore phase relations, modes and compositions within steps that crystallized significant amounts of solids over a small temperature interval. Whereas fractional crystallization experiments under oxidizing conditions produced large amounts of liquids (>76%) facilitating analysis of the liquid using large electron beam sizes (10–20 μm) and reduced currents (7 nA) to minimize alkali migration in H_2O-rich glasses, fractional crystallization experiments under reduced conditions (FC Mb Pt–C) resulted in lower melt fractions down to 52·7%. Equilibrium crystallization produces decreasing melts fractions with decreasing temperature resulting in very low melt fractions (<20%) at the lowest temperatures (980–1000°C), additionally complicated by quench crystallization (amphibole and cpx) that rendered analysis of the melt phase rather difficult.

A prerequisite to successfully employing the capsule-in-capsule technique to constrain the fO_2 conditions via the ferric–ferrous iron ratio in the starting material in the H_2O-undersaturated, oxidized fractionation experiments is the preservation of a near closed system, in particular regarding potential iron and hydrogen loss or gain. Iron loss was evaluated via LSR analysis of the experimental charges. The resulting iron loss or gain (from the pre-saturated capsules) was less than 12·5% relative for all fractional crystallization experiments. Fe loss or gain of generally less than 8% is

Table 3: Electron microprobe analyses of experimental phases of equilibrium crystallization experiments on composition RC158c

Run #	T (°C)	Phase	#	SiO_2	TiO_2	Cr_2O_3	Al_2O_3	FeO	MnO	NiO	MgO	CaO	Na_2O	K_2O	Total	x_{Mg}
EQ Mb AuPd																
PU910	1200	glass	8	44·41 (25)	0·77 (4)	0·08 (4)	12·11 (10)	9·08 (12)	0·19 (5)	n.d.	13·11 (44)	10·65 (24)	1·17 (11)	0·41 (2)	92·00	0·720
		ol	8	40·70 (05)	0·02 (1)	0·05 (3)	0·05 (3)	7·89 (15)	0·14 (2)	n.d.	50·78 (39)	0·24 (11)	0·01 (1)	0·00 (00)	99·88	0·920
		sp	4	0·74 (93)	0·53 (7)	36·88 (483)	14·67 (367)	28·67 (80)	0·00	n.d.	15·46 (80)	0·41 (16)	0·05 (1)	0·01 (1)	97·43	0·490
PU908	1200	glass	6	44·34 (29)	0·76 (4)	0·09 (5)	12·65 (26)	9·34 (17)	0·17 (4)	n.d.	12·49 (16)	10·94 (7)	1·14 (10)	0·45 (1)	92·36	0·704
		ol	8	40·42 (20)	0·02 (1)	0·04 (2)	0·05 (2)	9·24 (7)	0·15 (2)	n.d.	50·08 (21)	0·25 (2)	0·01 (1)	0·00	100·24	0·906
		sp	5	0·86 (35)	0·34 (2)	39·42 (309)	19·35 (157)	24·09 (62)	0·00	n.d.	15·51 (31)	0·4 (8)	0·03 (2)	0·01 (1)	100·01	0·534
PU926	1160	glass	6	44·94 (13)	0·81 (3)	0·06 (3)	14·41 (11)	8·89 (8)	0·18 (2)	0·02 (2)	10·06 (15)	11·60 (10)	1·12 (4)	0·48 (1)	92·57	0·669
		ol	8	40·56 (24)	0·02 (1)	0·03 (3)	0·12 (3)	9·72 (15)	0·19 (3)	0·23 (3)	49·61 (20)	0·25 (1)	0·02 (2)	0·01 (1)	100·74	0·901
		sp	6	0·23 (11)	0·36 (14)	37·24 (646)	15·50 (186)	29·18 (459)	0·31 (3)	0·12 (5)	13·89 (47)	0·26 (2)	0·01 (2)	0·01 (1)	97·12	0·459
PU899	1160	glass	8	45·02 (62)	0·87 (4)	0·06 (2)	14·12 (12)	10·09 (26)	0·20 (6)	n.d.	10·41 (21)	11·50 (22)	1·34 (6)	0·50 (2)	94·11	0·648
		ol	8	39·22 (105)	0·01 (1)	0·03 (1)	0·04 (2)	11·55 (18)	0·16 (4)	n.d.	48·12 (31)	0·21 (2)	0·00	0·01 (1)	99·36	0·881
		cpx	9	51·24 (44)	0·23 (2)	0·77 (10)	4·64 (31)	5·64 (22)	0·08 (2)	n.d.	17·26 (31)	20·20 (27)	0·32 (4)	0·01 (1)	100·39	0·845
PU909	1120	glass	8	45·01 (32)	0·81 (5)	0·05 (4)	13·94 (23)	9·14 (11)	0·19 (3)	n.d.	9·59 (16)	11·10 (10)	1·31 (7)	0·49 (2)	91·56	0·651
		ol	6	39·70 (19)	0·02 (1)	0·02 (1)	0·03 (2)	9·36 (16)	0·21 (1)	n.d.	49·88 (19)	0·20 (1)	0·02 (2)	0·00	99·43	0·905
		cpx	9	50·91 (18)	0·24 (3)	0·78 (13)	4·30 (25)	5·12 (23)	0·09 (3)	n.d.	17·13 (29)	21·27 (38)	0·27 (2)	0·01 (1)	100·13	0·856
		sp	3	0·17 (7)	0·57 (11)	19·96 (490)	16·03 (221)	44·08 (464)	0·00	n.d.	13·22 (63)	0·21 (8)	0·01 (1)	0·01 (1)	94·27	0·348
PU1006	1100	glass	12	46·87 (32)	1·02 (5)	0·02 (2)	17·31 (54)	9·08 (25)	0·17 (2)	n.d.	5·55 (78)	10·63 (51)	1·46 (8)	0·57 (4)	92·70	0·522
		ol	10	40·61 (13)	0·02 (1)	0·03 (2)	0·06 (2)	12·10 (13)	0·18 (2)	0·17 (2)	47·51 (31)	0·27 (2)	0·00	0·01 (1)	100·96	0·875
		cpx	9	50·62 (34)	0·35 (2)	0·57 (14)	5·46 (30)	5·79 (24)	0·14 (2)	0·04 (2)	16·55 (50)	20·41 (58)	0·28 (2)	0·01 (1)	100·22	0·836
		sp	6	0·32 (21)	0·54 (6)	17·75 (42)	33·96 (174)	28·88 (80)	0·21 (1)	0·19 (2)	16·41 (30)	0·30 (11)	0·01 (1)	0·01 (1)	98·57	0·503
PU1003	1080	glass	6	45·29 (44)	0·98 (4)	0·02 (3)	17·10 (25)	8·14 (16)	0·18 (1)	n.d.	4·40 (42)	11·24 (14)	1·36 (5)	0·49 (4)	89·20	0·490
		ol	8	40·30 (22)	0·02 (1)	0·02 (2)	0·03 (2)	12·01 (25)	0·20 (2)	0·17 (2)	47·29 (39)	0·25 (3)	0·01 (1)	0·00	100·30	0·875
		cpx	9	50·38 (70)	0·35 (13)	0·59 (24)	4·88 (95)	5·56 (66)	0·14 (3)	0·02 (2)	16·33 (60)	20·87 (80)	0·24 (3)	0·01 (1)	99·36	0·839
		sp	6	0·14 (10)	0·60 (10)	27·37 (563)	23·79 (333)	30·51 (215)	0·25 (1)	0·16 (5)	14·05 (65)	0·27 (4)	0·01 (2)	0·01 (1)	97·15	0·451
PU1004	1060	glass	13	46·51 (55)	1·02 (8)	0·02 (2)	19·04 (56)	6·54 (59)	0·16 (2)	n.d.	2·82 (52)	10·04 (49)	1·22 (10)	0·33 (5)	87·70	0·435
		ol	8	40·00 (14)	0·02 (1)	0·01 (1)	0·03 (1)	13·90 (8)	0·22 (2)	0·17 (2)	46·08 (24)	0·20 (1)	0·00	0·01 (1)	100·63	0·855
		cpx	10	49·81 (96)	0·48 (14)	0·20 (12)	5·89 (101)	6·64 (35)	0·17 (2)	0·02 (2)	16·06 (91)	19·86 (96)	0·27 (5)	0·01 (1)	99·39	0·812
		sp	6	0·17 (18)	0·49 (5)	7·11 (118)	44·64 (164)	29·93 (83)	0·17 (2)	0·22 (3)	16·19 (67)	0·18 (2)	0·00	0·01 (1)	99·13	0·491
PU905	1040	glass	5	46·82 (25)	0·83 (1)	0·01 (1)	18·94 (28)	5·62 (27)	0·20 (2)	n.d.	2·37 (1)	9·27 (30)	1·08 (12)	0·35 (2)	85·46	0·429
		ol	3	39·04 (30)	0·00	0·02 (1)	0·05 (1)	13·47 (13)	0·26 (3)	n.d.	46·76 (40)	0·16 (2)	0·00	0·01 (1)	99·77	0·861
		cpx	10	48·21 (48)	0·57 (24)	0·23 (10)	6·44 (53)	6·78 (27)	0·18 (2)	n.d.	15·50 (47)	20·48 (47)	0·28 (3)	0·01 (1)	98·67	0·803
		High-Al opx	5	51·02 (37)	0·16 (3)	0·08 (1)	6·37 (27)	10·44 (21)	0·25 (1)	n.d.	29·78 (24)	1·06 (5)	0·03 (1)	0·01 (1)	99·20	0·836
		Low-Al opx	5	53·85 (19)	0·11 (1)	0·04 (3)	2·93 (16)	9·65 (12)	0·27 (3)	n.d.	31·21 (20)	1·25 (7)	0·03 (0)	0·01 (1)	99·33	0·852
		amph	10	40·95 (57)	1·12 (7)	0·17 (8)	14·29 (32)	8·69 (42)	0·13 (4)	n.d.	16·22 (16)	11·62 (32)	2·03 (4)	0·64 (13)	95·85	0·769
		sp	5	0·14 (03)	1·04 (31)	9·88 (722)	22·39 (158)	49·75 (600)	0·07 (8)	n.d.	11·68 (25)	0·21 (7)	0·02 (2)	0·01 (0)	95·17	0·295
PU1005	1000	glass	20	48·51 (98)	0·74 (10)	0·01 (1)	19·68 (48)	5·23 (81)	0·16 (2)	n.d.	1·81 (44)	8·82 (47)	0·90 (12)	0·43 (9)	86·29	0·382
		ol	10	39·90 (22)	0·02 (1)	0·01 (2)	0·03 (2)	15·87 (11)	0·25 (3)	0·15 (2)	44·96 (34)	0·19 (2)	0·00	0·00	101·38	0·835
		cpx	15	49·45 (67)	0·52 (9)	0·28 (9)	6·51 (72)	6·72 (23)	0·17 (2)	0·03 (2)	15·37 (42)	20·57 (53)	0·22 (2)	0·01 (1)	99·86	0·803
		opx	10	51·85 (49)	0·18 (2)	0·22 (2)	6·55 (29)	11·30 (12)	0·24 (2)	0·06 (2)	29·15 (32)	1·18 (6)	0·02 (2)	0·00	100·74	0·821
		amph	15	42·34 (49)	1·13 (18)	0·32 (15)	14·29 (24)	8·63 (74)	0·10 (2)	0·05 (2)	16·33 (54)	11·40 (15)	1·95 (11)	0·60 (15)	97·13	0·771
		sp	6	0·06 (2)	0·49 (3)	5·73 (13)	45·13 (62)	31·56 (54)	0·20 (2)	0·23 (2)	15·61 (7)	0·16 (3)	0·00	0·00	99·16	0·469
PU906	980	glass	10	49·39 (63)	0·53 (8)	0·03 (2)	19·03 (38)	3·82 (51)	0·20 (7)	n.d.	1·66 (58)	8·47 (23)	0·68 (9)	0·52 (5)	84·33	0·437
		cpx	10	48·49 (66)	0·43 (9)	0·18 (9)	5·77 (68)	6·76 (24)	0·20 (3)	n.d.	15·66 (61)	20·87 (45)	0·20 (2)	0·01 (1)	98·57	0·805
		opx	6	50·43 (52)	0·20 (1)	0·18 (6)	6·74 (49)	11·77 (20)	0·26 (2)	n.d.	28·14 (24)	1·25 (15)	0·03 (5)	0·01 (2)	99·01	0·810
		amph	6	41·73 (45)	0·92 (6)	0·26 (13)	13·61 (61)	8·35 (18)	0·13 (2)	n.d.	16·43 (25)	11·77 (15)	1·62 (3)	0·62 (5)	95·43	0·778
		sp	6	0·16 (07)	1·53 (13)	3·34 (246)	15·37 (46)	64·18 (255)	0·18 (11)	n.d.	9·09 (35)	0·26 (4)	0·00	0·01 (1)	94·11	0·201
EQ Mb Pt–C																
PU72	1350	glass	5	46·19 (28)	0·67 (4)	0·15 (1)	12·80 (07)	8·14 (20)	0·15 (4)	n.d.	17·06 (14)	9·93 (8)	1·19 (3)	0·40 (1)	96·68	0·789
ZP1330	1330	glass	10	46·90 (34)	0·74 (6)	0·21 (3)	12·70 (17)	9·04 (20)	0·17 (2)	n.d.	16·05 (21)	10·13 (7)	1·19 (4)	0·42 (2)	97·56	0·760
		ol	11	41·45 (19)	0·01 (1)	0·10 (2)	0·00	9·20 (18)	0·13 (1)	0·07 (4)	49·73 (20)	0·25 (1)	0·01 (1)	0·00	100·95	0·906
ZP1301	1300	glass	10	46·58 (39)	0·74 (6)	0·21 (3)	13·35 (27)	8·76 (21)	0·17 (2)	0·01 (2)	13·93 (28)	10·82 (13)	1·27 (4)	0·43 (1)	96·27	0·739
		ol	10	41·23 (25)	0·01 (2)	0·15 (1)	0·00	10·21 (22)	0·15 (2)	0·14 (3)	49·20 (31)	0·29 (2)	0·01 (1)	0·00	101·39	0·896
ZP1302	1300	glass	10	46·93 (52)	0·74 (6)	0·20 (3)	13·00 (31)	8·84 (35)	0·16 (3)	n.d.	15·12 (10)	10·33 (5)	1·20 (4)	0·44 (1)	96·96	0·753
		ol	10	41·69 (19)	0·01 (1)	0·09 (2)	0·00	9·51 (22)	0·14 (2)	0·06 (5)	49·91 (15)	0·23 (2)	0·02 (1)	0·00	101·65	0·903

(continued)

Table 3: Continued

Run #	T (°C)	Phase	#	SiO_2	TiO_2	Cr_2O_3	Al_2O_3	FeO	MnO	NiO	MgO	CaO	Na_2O	K_2O	Total	x_{Mg}
ZP1270	1270	glass	10	46·52 (27)	0·80 (4)	0·18 (2)	13·40 (38)	8·91 (26)	0·15 (3)	0·00	14·11 (60)	10·72 (24)	1·22 (3)	0·42 (1)	96·44	0·738
		ol	10	41·09 (32)	0·00	0·12 (1)	0·00	10·22 (34)	0·13 (1)	0·04 (4)	49·17 (62)	0·24 (2)	0·01 (1)	0·00	101·02	0·896
ZP1240	1240	glass	9	46·95 (27)	0·78 (8)	0·19 (2)	14·08 (41)	8·84 (28)	0·15 (2)	0·01 (2)	12·81 (15)	11·11 (9)	1·32 (4)	0·47 (1)	96·70	0·721
		ol	11	41·31 (42)	0·00	0·12 (2)	0·00	11·23 (27)	0·15 (2)	0·05 (4)	48·64 (72)	0·24 (2)	0·01 (1)	0·01 (1)	101·75	0·885
ZP1210	1210	glass	12	47·67 (38)	0·85 (5)	0·16 (2)	15·17 (45)	8·49 (23)	0·17 (3)	0·00	10·71 (39)	12·00 (13)	1·37 (6)	0·49 (2)	97·09	0·692
		ol	10	41·18 (38)	0·00	0·13 (3)	0·00	12·37 (37)	0·16 (2)	0·04 (3)	48·16 (20)	0·28 (3)	0·01 (1)	0·00	102·32	0·874
		sp	10	0·19 (29)	0·33 (3)	32·81 (86)	34·89 (61)	14·49 (31)	0·17 (2)	0·04 (2)	16·30 (19)	0·11 (4)	0·00	0·00	99·34	0·667
ZP1180	1180	glass	10	47·44 (71)	0·92 (8)	0·10 (4)	16·31 (56)	8·31 (34)	0·17 (2)	0·01 (2)	9·15 (52)	12·00 (24)	1·48 (6)	0·52 (2)	96·41	0·662
		ol	8	40·61 (26)	0·00	0·05 (4)	0·00	13·44 (22)	0·19 (2)	0·03 (4)	46·45 (10)	0·26 (2)	0·00	0·00	101·03	0·860
		High-Al cpx	9	50·56 (45)	0·40 (4)	1·28 (17)	5·76 (51)	4·20 (31)	0·13 (1)	0·00	16·46 (10)	20·76 (14)	0·25 (3)	0·00	99·81	0·875
		Low-Al cpx	7	52·70 (66)	0·29 (4)	0·83 (6)	2·26 (27)	4·45 (38)	0·16 (1)	0·00	18·22 (24)	20·01 (60)	0·16 (3)	0·00	99·08	0·880
		sp	8	0·00	0·38 (4)	32·60 (273)	33·77 (224)	15·69 (51)	0·18 (3)	0·00	15·45 (36)	0·16 (9)	0·00	0·00	98·24	0·637
ZP1151	1150	glass	10	47·75 (36)	0·94 (6)	0·05 (4)	16·22 (30)	8·19 (26)	0·17 (2)	0·00	9·39 (11)	11·40 (8)	1·43 (8)	0·53 (1)	96·08	0·672
		ol	16	40·76 (73)	0·01 (2)	0·06 (3)	0·02 (02)	13·58 (30)	0·17 (3)	0·02 (2)	46·21 (87)	0·34 (12)	0·01 (1)	0·00	101·17	0·858
		High-Al cpx	8	51·00 (49)	0·48 (10)	1·19 (12)	7·07 (68)	4·43 (49)	0·12 (1)	0·00	16·34 (43)	20·43 (25)	0·29 (2)	0·00	101·35	0·868
		Low-Al cpx	8	53·20 (59)	0·23 (2)	1·06 (17)	4·08 (40)	4·42 (41)	0·12 (3)	0·00	17·97 (57)	19·89 (62)	0·26 (2)	0·00	101·24	0·879
		sp	10	0·26 (33)	0·37 (9)	27·47 (260)	36·27 (298)	15·77 (49)	0·18 (4)	0·00	15·87 (52)	0·28 (15)	0·00	0·00	96·49	0·642
ZP1152	1150	glass	12	46·86 (96)	1·01 (9)	0·08 (3)	17·44 (43)	7·82 (35)	0·24 (4)	0·01 (3)	8·04 (43)	10·75 (51)	2·10 (11)	0·53 (4)	94·88	0·647
		ol	8	40·70 (32)	0·00	0·08 (1)	0·00	13·33 (57)	0·28 (4)	0·11 (3)	46·31 (47)	0·26 (5)	0·00	0·00	101·07	0·861
		cpx	10	50·97 (78)	0·48 (8)	1·06 (8)	6·49 (94)	4·86 (30)	0·20 (4)	0·00	16·30 (48)	19·99 (17)	0·34 (1)	0·01 (1)	100·68	0·857
		sp	11	0·00	0·24 (3)	21·65 (119)	45·64 (118)	14·04 (55)	0·23 (5)	0·10 (6)	17·86 (40)	0·09 (6)	0·00	0·01 (1)	100·18	0·694
ZP1121	1120	glass	12	46·82 (125)	0·84 (6)	0·04 (3)	17·73 (38)	7·38 (49)	0·13 (2)	0·00	8·17 (28)	10·92 (36)	2·79 (12)	0·58 (5)	95·40	0·664
		ol	12	41·40 (53)	0·01 (1)	0·05 (3)	0·00	14·05 (61)	0·17 (3)	0·07 (3)	45·95 (46)	0·24 (3)	0·02 (3)	0·01 (1)	101·97	0·854
		cpx	10	51·76 (71)	0·52 (10)	0·34 (12)	7·81 (81)	5·54 (39)	0·14 (3)	0·02 (2)	16·50 (38)	18·89 (45)	0·43 (8)	0·03 (1)	101·97	0·842
		High-Al opx	4	53·97 (38)	0·15 (4)	0·30 (9)	6·62 (22)	7·89 (32)	0·16 (2)	0·00	29·89 (53)	1·64 (2)	0·13 (1)	0·00	100·75	0·871
		Low-Al opx	7	55·71 (53)	0·12 (3)	0·27 (7)	4·00 (85)	8·26 (29)	0·14 (2)	0·00	30·68 (45)	1·71 (10)	0·13 (3)	0·00	101·02	0·869
		sp	8	0·97 (49)	0·14 (2)	9·73 (119)	56·32 (102)	12·18 (26)	0·12 (2)	0·06 (3)	19·76 (60)	0·16 (6)	0·00	0·00	99·44	0·743
ZP1122	1120	glass	10	46·51 (65)	0·98 (6)	0·00	17·91 (38)	6·86 (20)	0·13 (3)	0·00	8·66 (20)	11·05 (14)	1·94 (4)	0·74 (2)	94·77	0·692
		ol	8	41·63 (47)	0·01 (1)	0·01 (1)	0·00	12·80 (23)	0·14 (4)	0·02 (7)	47·65 (57)	0·28 (4)	0·00	0·00	102·59	0·869
		cpx	12	52·26 (62)	0·40 (8)	0·53 (19)	6·43 (58)	4·65 (38)	0·16 (4)	0·02 (4)	16·99 (47)	20·08 (58)	0·28 (3)	0·00	101·78	0·867
		High-Al opx	9	53·27 (52)	0·21 (5)	0·39 (7)	7·78 (32)	8·69 (73)	0·13 (3)	0·03 (5)	29·50 (67)	1·72 (2)	0·04 (1)	0·00	101·76	0·858
		Low-Al opx	4	56·62 (58)	0·12 (1)	0·29 (4)	3·38 (10)	8·81 (30)	0·15 (2)	0·02 (4)	31·12 (31)	1·86 (6)	0·03 (1)	0·00	102·40	0·863
ZP1090	1090	glass	8	49·12 (24)	1·09 (9)	0·01 (1)	18·33 (89)	8·63 (48)	0·17 (2)	0·01 (2)	7·01 (52)	10·29 (67)	2·31 (12)	0·86 (9)	97·83	0·592
		ol	7	42·41 (28)	0·00	0·03 (2)	0·00	17·48 (45)	0·27 (2)	0·15 (2)	44·77 (48)	0·26 (1)	0·00	0·01 (1)	105·38	0·820
		cpx	9	50·87 (38)	0·51 (4)	0·41 (8)	6·95 (43)	5·52 (17)	0·15 (3)	0·00	16·29 (13)	20·05 (23)	0·33 (2)	0·01 (1)	101·10	0·840
		High-Al opx	5	52·27 (33)	0·30 (3)	0·03 (3)	8·23 (48)	11·01 (13)	0·25 (2)	0·00	27·92 (10)	1·72 (18)	0·05 (1)	0·01 (1)	101·79	0·819
		Low-Al opx	5	55·25 (7)	0·14 (2)	0·03 (3)	3·70 (12)	10·99 (24)	0·25 (4)	0·00	29·68 (19)	1·67 (1)	0·05 (2)	0·01 (1)	101·76	0·828
		sp	8	0·00	0·18 (4)	4·43 (291)	65·62 (298)	13·90 (54)	0·13 (4)	0·09 (3)	19·74 (50)	0·17 (6)	0·01 (2)	0·02 (1)	104·30	0·717
ZP1060	1060	glass	13	46·87 (148)	1·07 (18)	0·02 (3)	19·33 (52)	7·51 (40)	0·11 (3)	0·00	4·85 (64)	7·38 (37)	3·63 (30)	1·55 (9)	92·29	0·535
		ol	4	39·12 (21)	0·05 (1)	0·02 (2)	0·00	20·11 (50)	0·23 (2)	0·11 (3)	39·55 (40)	0·28 (3)	0·00	0·00	99·48	0·778
		cpx	10	51·16 (72)	0·81 (6)	0·15 (7)	7·39 (20)	5·82 (26)	0·14 (2)	0·02 (2)	15·79 (64)	20·21 (32)	0·41 (4)	0·02 (1)	101·93	0·829
		opx	9	53·57 (74)	0·28 (4)	0·11 (4)	6·46 (64)	11·91 (57)	0·20 (3)	0·01 (2)	27·78 (50)	1·54 (22)	0·05 (4)	0·01 (2)	101·93	0·806
		amp	5	42·28 (74)	1·94 (15)	0·15 (1)	15·32 (40)	7·51 (33)	0·11 (1)	0·03 (2)	15·61 (34)	11·15 (72)	2·40 (17)	0·71 (4)	97·20	0·787
		sp	8	0·00	0·20 (4)	1·64 (134)	60·86 (168)	15·25 (33)	0·11 (2)	0·14 (3)	17·60 (42)	0·20 (2)	0·00	0·00	96·00	0·673
ZP1000	1000	glass	8	44·67 (55)	0·92 (7)	0·00	20·72 (13)	6·50 (09)	0·06 (2)	0·00	3·98 (41)	9·01 (15)	3·12 (20)	1·24 (6)	90·20	0·521
		cpx	9	50·81 (82)	0·70 (20)	0·16 (4)	7·26 (84)	6·22 (39)	0·17 (2)	0·02 (3)	15·21 (43)	20·91 (31)	0·31 (7)	0·01 (1)	101·80	0·813
		opx	9	52·97 (54)	0·17 (4)	0·13 (6)	6·12 (72)	13·06 (29)	0·24 (2)	0·01 (2)	27·32 (49)	1·22 (4)	0·02 (1)	0·00	101·28	0·788
		amp	9	43·27 (69)	1·09 (20)	0·21 (8)	15·67 (93)	7·74 (48)	0·11 (2)	0·05 (2)	15·94 (49)	11·12 (57)	2·23 (14)	0·69 (9)	98·12	0·786
		sp	8	0·00	0·14 (2)	1·68 (19)	65·05 (57)	15·12 (25)	0·15 (1)	0·13 (3)	18·61 (28)	0·24 (2)	0·00	0·00	101·12	0·687

All Fe as FeO. Units in parentheses indicate standard deviations (2σ) from averaged analysis [i.e. 44·41(25) should be read as 44·41 ± 0·25 wt %]; #, number of individual spots averaged for each phase composition reported. Abbreviations are as for Table 2; x_{Mg} = molar [MgO/(MgO + FeO_{tot})].

Table 4: Electron microprobe analyses of experimental phases of fractional crystallization experiments

Run #	*T* (°C)	phase	#	SiO_2	TiO_2	Cr_2O_3	Al_2O_3	FeO	MnO	NiO	MgO	CaO	Na_2O	K_2O	P_2O_5	Total	x_{Mg}	x_{An}
FC ba AuPd																		
rk48	1230	glass	9	48·95 (33)	0·60 (4)	n.d.	14·71 (35)	7·84 (23)	0·18 (7)	n.d.	9·59 (16)	9·25 (8)	2·04 (14)	0·36 (3)	n.d.	93·52	0·686	
rk50	1200	glass	10	48·00 (48)	0·60 (5)	n.d.	14·44 (31)	8·15 (13)	0·14 (5)	n.d.	8·85 (11)	9·36 (14)	2·14 (16)	0·38 (2)	n.d.	92·06	0·659	
		opx	10	55·15 (40)	0·08 (1)	n.d.	3·11 (28)	7·74 (16)	0·18 (3)	n.d.	32·37 (26)	1·48 (13)	0·03 (2)	0·00	n.d.	100·14	0·882	
rk56	1170	glass	9	48·71 (27)	0·65 (3)	n.d.	15·47 (18)	7·73 (29)	0·18 (4)	n.d.	7·45 (19)	9·41 (21)	2·25 (14)	0·43 (3)	n.d.	92·29	0·632	
		cpx	9	52·60 (38)	0·20 (2)	n.d.	3·45 (50)	5·40 (18)	0·20 (3)	n.d.	18·04 (49)	19·32 (49)	0·29 (12)	0·01 (1)	n.d.	99·51	0·856	
		opx	10	55·39 (31)	0·11 (2)	n.d.	2·81 (48)	9·17 (17)	0·25 (5)	n.d.	30·94 (27)	1·78 (8)	0·05 (2)	0·01 (1)	n.d.	100·50	0·857	
rk60	1140	glass	10	50·09 (72)	0·69 (5)	n.d.	15·71 (22)	7·22 (21)	0·18 (4)	n.d.	6·64 (9)	9·23 (13)	2·11 (41)	0·47 (2)	n.d.	92·34	0·621	
		cpx	10	52·73 (25)	0·21 (4)	n.d.	3·00 (38)	5·30 (31)	0·21 (4)	n.d.	17·99 (16)	20·00 (28)	0·34 (4)	0·01 (1)	n.d.	99·80	0·857	
		opx	10	55·25 (63)	0·13 (3)	n.d.	2·59 (29)	9·37 (31)	0·30 (3)	n.d.	30·94 (37)	1·71 (17)	0·05 (2)	0·01 (1)	n.d.	100·33	0·855	
rk63	1110	glass	9	48·76 (28)	0·76 (5)	n.d.	16·38 (27)	6·06 (19)	0·17 (5)	n.d.	6·05 (11)	8·77 (10)	2·48 (12)	0·58 (3)	n.d.	90·00	0·640	
		cpx	10	52·81 (44)	0·26 (4)	n.d.	3·20 (47)	4·92 (35)	0·26 (5)	n.d.	17·64 (46)	20·58 (65)	0·32 (3)	0·01 (1)	n.d.	100·00	0·865	
		opx	10	54·79 (17)	0·15 (2)	n.d.	3·09 (24)	9·18 (21)	0·32 (4)	n.d.	30·59 (33)	1·56 (20)	0·04 (2)	0·01 (1)	n.d.	99·73	0·856	
rk66	1080	glass	10	49·38 (26)	0·83 (4)	n.d.	17·68 (19)	6·14 (20)	0·17 (4)	n.d.	4·47 (9)	7·78 (8)	2·80 (11)	0·66 (3)	n.d.	89·89	0·565	
		cpx	8	49·12 (50)	0·60 (4)	n.d.	6·99 (31)	6·26 (15)	0·22 (3)	n.d.	14·78 (39)	20·44 (28)	0·48 (4)	0·02 (2)	n.d.	98·90	0·808	
		opx	9	52·99 (37)	0·20 (3)	n.d.	5·25 (73)	11·33 (22)	0·35 (3)	n.d.	28·77 (34)	1·25 (9)	0·04 (2)	0·00	n.d.	100·19	0·819	
rk69	1050	glass	10	49·66 (31)	0·81 (5)	n.d.	17·91 (27)	6·20 (11)	0·20 (6)	n.d.	3·78 (10)	7·85 (9)	2·48 (12)	0·68 (3)	n.d.	89·57	0·521	
		cpx	6	48·88 (86)	0·69 (4)	n.d.	6·86 (33)	6·86 (31)	0·26 (3)	n.d.	14·44 (35)	21·22 (32)	0·46 (4)	0·01 (1)	n.d.	99·68	0·789	
		amp	10	42·13 (65)	1·66 (5)	n.d.	14·40 (40)	9·52 (42)	0·18 (3)	n.d.	15·32 (38)	11·26 (19)	2·47 (5)	0·43 (2)	n.d.	97·36	0·742	
rk70	1020	glass	10	50·16 (65)	0·81 (3)	n.d.	18·22 (34)	6·04 (16)	0·21 (5)	n.d.	3·01 (9)	7·61 (17)	2·57 (13)	0·72 (2)	n.d.	89·34	0·470	
		cpx	7	47·37 (38)	0·84 (4)	n.d.	8·20 (46)	7·78 (12)	0·31 (2)	n.d.	12·91 (31)	21·23 (16)	0·51 (5)	0·01 (1)	n.d.	99·17	0·747	
		amp	8	41·59 (31)	1·86 (4)	n.d.	15·72 (19)	10·32 (14)	0·24 (3)	n.d.	14·02 (4)	11·13 (9)	2·47 (5)	0·42 (2)	n.d.	97·76	0·708	
rk71	990	glass	10	52·58 (58)	0·73 (5)	n.d.	18·04 (7)	5·29 (26)	0·21 (4)	n.d.	2·09 (11)	7·38 (12)	2·79 (19)	0·74 (5)	n.d.	89·86	0·413	
		cpx	9	46·30 (61)	0·96 (9)	n.d.	9·26 (67)	9·17 (14)	0·33 (5)	n.d.	11·22 (34)	21·74 (13)	0·57 (3)	0·01 (1)	n.d.	99·56	0·686	
		amp	10	40·79 (41)	2·02 (11)	n.d.	15·72 (24)	12·50 (23)	0·26 (4)	n.d.	12·05 (23)	11·51 (7)	2·49 (8)	0·39 (2)	n.d.	97·72	0·632	
PU1049	990	glass	11	49·67 (19)	0·76 (4)	n.d.	18·46 (19)	5·46 (9)	0·20 (4)	n.d.	3·23 (9)	7·43 (20)	2·85 (11)	0·72 (4)	0·16 (6)	88·94	0·513	
		amp	12	40·96 (39)	2·00 (18)	n.d.	15·89 (39)	10·87 (42)	0·23 (3)	n.d.	14·21 (36)	10·96 (37)	2·28 (4)	0·39 (4)	0·01 (1)	97·81	0·700	
		mag	8	0·13 (1)	3·11 (8)	n.d.	15·83 (48)	69·13 (76)	0·45 (2)	n.d.	6·16 (13)	0·16 (2)	0·01 (1)	0·01 (1)	0·01 (1)	94·98	0·137	
PU1070	980	glass	22	48·58 (18)	0·84 (9)	n.d.	18·20 (20)	5·20 (20)	0·23 (7)	n.d.	2·79 (24)	7·58 (10)	2·74 (6)	0·74 (6)	0·24 (4)	87·14	0·488	
		amp	30	40·98 (69)	2·14 (9)	n.d.	15·46 (32)	8·26 (25)	0·23 (5)	n.d.	13·91 (35)	11·02 (28)	2·34 (15)	0·43 (6)	n.d.	94·76	0·750	
PU1062	950	glass	41	52·17 (60)	0·76 (7)	n.d.	19·60 (39)	4·97 (19)	0·19 (2)	n.d.	2·24 (21)	7·43 (10)	3·10 (22)	0·81 (5)	0·18 (3)	91·24	0·446	
		amp	34	40·15 (33)	1·96 (9)	n.d.	16·72 (44)	9·64 (20)	0·23 (1)	n.d.	13·52 (26)	10·90 (14)	2·36 (4)	0·46 (2)	0·04 (2)	95·90	0·714	
		gar	15	37·96 (32)	0·61 (12)	n.d.	22·61 (20)	17·13 (23)	1·33 (11)	n.d.	10·54 (44)	8·48 (49)	0·03 (2)	0·01 (1)	0·05 (1)	98·73	0·523	
PU1064	900	glass	25	55·65 (30)	0·51 (6)	n.d.	17·86 (25)	3·93 (7)	0·10 (3)	n.d.	1·13 (3)	6·05 (8)	3·15 (15)	1·05 (5)	0·24 (4)	89·67	0·339	
		amp	26	41·87 (68)	2·00 (20)	n.d.	17·07 (52)	15·04 (26)	0·25 (2)	n.d.	10·21 (7)	10·47 (18)	2·29 (5)	0·49 (3)	0·02 (1)	99·71	0·548	
		gar	20	39·75 (36)	1·20 (7)	n.d.	22·07 (22)	21·65 (35)	1·60 (5)	n.d.	6·77 (25)	9·65 (42)	0·02 (1)	0·01 (1)	0·02 (1)	102·75	0·358	
		plg	32	48·83 (83)	0·03 (2)	n.d.	34·61 (52)	0·38 (2)	0·01 (1)	n.d.	0·02 (1)	17·44 (46)	1·86 (15)	0·03 (1)	0·02 (2)	103·30		0·838
		ilm	17	0·04 (1)	41·44 (104)	n.d.	0·78 (5)	55·33 (171)	0·35 (3)	n.d.	2·23 (15)	0·14 (3)	0·01 (1)	0·01 (1)	0	100·19	0·055	
PU1066	850	glass	24	58·06 (38)	0·38 (2)	n.d.	16·41 (28)	2·83 (9)	0·08 (3)	n.d.	0·74 (4)	4·88 (9)	3·22 (12)	1·24 (4)	0·21 (4)	88·05	0·317	
		gar	19	38·73 (55)	1·06 (12)	n.d.	21·40 (30)	23·62 (27)	1·34 (12)	n.d.	5·40 (24)	9·19 (23)	n.d.	n.d.	n.d.	100·73	0·289	
		plg	23	49·25 (78)	n.d.	n.d.	33·32 (48)	0·39 (15)	n.d.	n.d.	16·05 (40)	2·45 (16)	0·03 (2)	n.d.	n.d.	101·49		0·784
		ilm	6	0·33 (4)	56·45 (54)	n.d.	0·35 (4)	42·84 (48)	0·48 (6)	n.d.	2·53 (6)	0·25 (4)	n.d.	n.d.	n.d.	103·24	0·095	
PU1068	800	glass	27	62·93 (32)	0·21 (4)	n.d.	15·06 (16)	1·76 (9)	0·05 (2)	n.d.	0·38 (2)	3·28 (6)	3·73 (10)	1·55 (5)	0·12 (3)	89·07	0·276	
		amp	16	43·99 (87)	1·67 (7)	n.d.	13·97 (62)	18·77 (89)	0·45 (7)	n.d.	8·03 (30)	9·75 (26)	2·03 (9)	0·38 (6)	n.d.	99·05	0·433	
		gar	24	37·96 (51)	1·05 (18)	n.d.	20·94 (22)	25·05 (67)	1·99 (16)	n.d.	3·47 (26)	9·47 (66)	n.d.	n.d.	n.d.	99·92	0·198	
		plg	21	57·12 (69)	n.d.	n.d.	28·67 (66)	0·27 (8)	n.d.	n.d.	n.d.	10·25 (35)	5·97 (16)	0·03 (2)	n.d.	102·32		0·487
		ilm	10	0·31 (15)	49·53 (70)	n.d.	0·41 (2)	47·98 (69)	0·41 (7)	n.d.	1·41 (4)	0·15 (5)	n.d.	n.d.	n.d.	100·19	0·050	
PU1072	750	glass	10	61·92 (39)	0·04 (2)	n.d.	13·22 (15)	0·87 (6)	0·10 (3)	n.d.	0·40 (3)	2·44 (7)	3·21 (7)	1·81 (5)	0·11 (2)	84·09	0·449	
		plg	14	55·26 (66)	n.d.	n.d.	26·02 (32)	0·24 (6)	n.d.	n.d.	n.d.	8·81 (25)	6·05 (11)	0·03 (3)	n.d.	96·41		0·446
		mag	7	0·65 (23)	15·90 (242)	n.d.	1·28 (26)	68·57 (130)	0·20 (6)	n.d.	0·40 (8)	0·16 (4)	n.d.	n.d.	n.d.	87·15	0·010	
		gar	10	35·45 (61)	0·05 (5)	n.d.	20·45 (31)	30·29 (166)	3·48 (10)	n.d.	2·37 (33)	2·92 (40)	n.d.	n.d.	n.d.	95·01	0·122	
PU1072-o 750	720	glass	15	64·34 (41)	0·07 (3)	n.d.	13·42 (14)	0·78 (10)	0·10 (2)	n.d.	0·36 (3)	2·05 (6)	3·28 (10)	1·92 (6)	0·11 (3)	86·43	0·453	
		plg	21	59·04 (59)	n.d.	n.d.	25·50 (35)	0·24 (7)	n.d.	n.d.	n.d.	7·46 (25)	7·05 (21)	0·05 (3)	n.d.	99·33		0·369
		amp	22	44·27 (96)	1·33 (18)	n.d.	11·83 (70)	19·02 (43)	0·96 (14)	n.d.	8·1 (29)	8·83 (23)	2·08 (13)	0·31 (10)	n.d.	96·72	0·432	
		mag	6	1·43 (24)	18·81 (357)	n.d.	1·48 (49)	66·64 (238)	0·27 (5)	n.d.	0·46 (9)	0·15 (2)	n.d.	m.d.	n.d.	89·25	0·012	
		qtz	4	99·18 (67)												99·18		

(continued)

Table 4: Continued

Run #	T (°C)	phase	#	SiO_2	TiO_2	Cr_2O_3	Al_2O_3	FeO	MnO	NiO	MgO	CaO	Na_2O	K_2O	P_2O_5	Total	x_{Mg}	x_{An}
FC Mb AuPd																		
rk47	1230	glass	16	43·86 (43)	0·79 (3)	0·08 (3)	12·11 (44)	9·32 (18)	0·16 (5)	0·02(2)	12·24 (70)	10·92 (33)	1·27 (9)	0·44 (3)	n.d.	91·37	0·701	
		ol	10	40·72 (31)	0·01 (1)	0·05 (3)	0·04 (1)	8·82 (16)	0·17 (3)	0·21 (2)	50·53 (19)	0·21 (2)	0·01 (1)	0·00	n.d.	100·77	0·911	
		sp	8	0·00	0·30 (6)	42·13 (585)	13·85 (275)	24·83 (164)	0·00	0·13 (3)	14·08 (39)	0·21 (9)	0·03 (3)	0·00	n.d.	95·56	0·501	
rk51	1200	glass	10	43·66 (41)	0·89 (4)	n.d.	14·02 (28)	9·00 (22)	0·20 (6)	n.d.	10·36 (12)	12·35 (13)	1·27 (10)	0·53 (2)	n.d.	92·27	0·672	
		ol	10	40·84 (15)	0·01 (1)	n.d.	0·03 (1)	10·33 (19)	0·19 (3)	n.d.	48·74 (26)	0·24 (2)	0·01 (1)	0·00	n.d.	100·39	0·894	
		cpx	9	52·08 (55)	0·23 (3)	n.d.	3·78 (52)	4·30 (14)	0·11 (3)	n.d.	17·39 (45)	21·68 (42)	0·21 (2)	0·00	n.d.	99·79	0·878	
rk52	1170	glass	10	44·61 (56)	0·71 (2)	n.d.	16·53 (32)	9·07 (24)	0·21 (4)	n.d.	8·92 (27)	11·33 (24)	1·53 (14)	0·74 (4)	n.d.	93·65	0·637	
		ol	10	40·66 (19)	0·01 (1)	n.d.	0·05 (1)	12·23 (27)	0·25 (4)	n.d.	46·77 (40)	0·24 (2)	0·00	0·00	n.d.	100·21	0·872	
		cpx	10	49·35 (80)	0·34 (6)	n.d.	7·49 (76)	5·68 (69)	0·16 (2)	n.d.	15·57 (47)	21·24 (59)	0·32 (3)	0·01 (1)	n.d.	100·17	0·830	
		sp	2	0·11 (1)	0·12 (1)	n.d.	59·39 (5)	18·96 (23)	0·18 (6)	n.d.	19·93 (20)	0·06 (1)	0·01 (1)	0·00	n.d.	98·74	0·652	
rk54	1140	glass	9	44·67 (34)	0·80 (6)	n.d.	17·21 (27)	9·53 (22)	0·23 (6)	n.d.	7·50 (14)	10·38 (12)	1·73 (12)	0·91 (3)	n.d.	92·97	0·584	
		cpx	10	48·73 (51)	0·42 (4)	n.d.	7·89 (48)	6·39 (29)	0·20 (2)	n.d.	14·85 (24)	21·49 (16)	0·32 (4)	0·01 (1)	n.d.	100·31	0·805	
		sp	9	0·10 (3)	0·18 (3)	n.d.	57·74 (100)	21·73 (49)	0·16 (3)	n.d.	18·47 (32)	0·14 (4)	0·01 (1)	0·00	n.d.	98·53	0·602	
rk57	1110	glass	9	47·00 (35)	0·86 (5)	n.d.	18·07 (25)	8·47 (26)	0·22 (5)	n.d.	5·66 (31)	8·74 (20)	2·16 (12)	1·07 (7)	n.d.	92·26	0·544	
		cpx	10	48·87 (43)	0·60 (5)	n.d.	7·95 (51)	7·03 (31)	0·26 (3)	n.d.	14·63 (24)	20·15 (36)	0·41 (4)	0·01 (1)	n.d.	99·90	0·788	
		opx	10	51·69 (38)	0·18 (3)	n.d.	6·86 (65)	12·28 (19)	0·35 (3)	n.d.	27·30 (49)	1·48 (22)	0·05 (3)	0·02 (3)	n.d.	100·21	0·798	
		sp	10	0·10 (7)	0·17 (6)	n.d.	60·28 (58)	20·73 (51)	0·20 (2)	n.d.	17·10 (19)	0·12 (3)	0·01 (2)	0·00	n.d.	98·71	0·595	
rk58	1080	glass	10	48·43 (44)	0·91 (4)	n.d.	17·18 (29)	8·40 (28)	0·30 (6)	n.d.	4·35 (27)	7·80 (34)	2·42 (9)	1·34 (4)	n.d.	91·13	0·480	
		cpx	8	45·65 (60)	0·96 (13)	n.d.	10·28 (72)	9·00 (32)	0·36 (5)	n.d.	12·22 (31)	20·06 (25)	0·55 (3)	0·01 (1)	n.d.	99·09	0·708	
		opx	7	48·63 (44)	0·25 (3)	n.d.	8·61 (47)	13·72 (47)	0·48 (2)	n.d.	25·34 (32)	1·11 (13)	0·05 (2)	0·00	n.d.	98·20	0·767	
		mag	5	0·13 (2)	3·10 (6)	n.d.	12·23 (8)	73·29 (53)	0·36 (6)	n.d.	4·97 (9)	0·04 (5)	0·00	0·00	n.d.	94·11	0·108	
rk73	1050	glass	10	49·86 (51)	0·86 (4)	n.d.	17·85 (17)	8·70 (17)	0·30 (6)	n.d.	3·78 (9)	7·90 (15)	2·29 (9)	1·18 (4)	n.d.	92·71	0·437	
		cpx	1	47·41	0·84	n.d.	8·07	8·34	0·34	n.d.	13·73	20·74	0·44	0·08	n.d.	99·99	0·746	
		amp	9	41·26 (49)	1·92 (10)	n.d.	15·73 (36)	10·45 (111)	0·28 (4)	n.d.	14·27 (56)	11·34 (18)	2·20 (8)	0·84 (4)	n.d.	98·29	0·709	
rk65	1020	glass	10	52·17 (27)	0·87 (4)	n.d.	17·18 (39)	7·07 (18)	0·28 (7)	n.d.	2·70 (5)	6·78 (9)	2·41 (11)	1·35 (3)	n.d.	90·81	0·405	
		cpx	10	47·50 (99)	0·75 (13)	n.d.	6·94 (84)	10·88 (60)	0·49 (4)	n.d.	12·31 (56)	20·04 (40)	0·51 (3)	0·01 (1)	n.d.	99·42	0·669	
		amp	4	41·01 (44)	2·17 (10)	n.d.	14·36 (26)	14·08 (20)	0·38 (2)	n.d.	12·05 (12)	10·91 (26)	2·19 (7)	0·70 (5)	n.d.	97·84	0·604	
		mag	5	0·12 (2)	5·96 (11)	n.d.	7·98 (14)	76·44 (101)	0·54 (4)	n.d.	3·03 (4)	0·04 (4)	0·00	0·00	n.d.	94·11	0·066	
rk67	990	glass	10	54·74 (111)	0·59 (8)	n.d.	15·94 (18)	5·59 (38)	0·31 (5)	n.d.	1·48 (12)	5·68 (7)	2·71 (16)	1·33 (7)	n.d.	88·36	0·321	
		cpx	4	46·31 (103)	0·77 (5)	n.d.	7·25 (51)	13·02 (7)	0·65 (4)	n.d.	10·30 (42)	19·48 (97)	0·75 (14)	0·02 (2)	n.d.	98·54	0·585	
		amp	12	40·46 (59)	1·96 (21)	n.d.	13·41 (31)	16·90 (60)	0·48 (3)	n.d.	10·28 (34)	10·75 (23)	2·19 (9)	0·67 (4)	n.d.	97·09	0·520	
		mag	4	0·15 (1)	6·10 (28)	n.d.	5·66 (4)	79·74 (110)	0·70 (6)	n.d.	1·49 (5)	0·17 (6)	0·01 (1)	0·01 (1)	n.d.	94·02	0·032	
PU1048	990	glass	13	52·64 (30)	0·86 (4)	n.d.	16·47 (10)	5·58 (8)	0·29 (3)	n.d.	2·69 (9)	6·60 (11)	2·61 (9)	1·32 (4)	0·22 (7)	89·28	0·462	
		cpx	4	50·08 (84)	0·83 (16)	n.d.	5·05 (75)	8·18 (22)	0·59 (3)	n.d.	14·63 (31)	19·48 (44)	0·32 (3)	0·01 (1)	0·01 (1)	99·17	0·761	
PU1069	980	glass	13	50·97 (33)	0·92 (3)	n.d.	16·65 (11)	6·17 (8)	0·31 (7)	n.d.	2·35 (3)	6·82 (8)	2·66 (5)	1·54 (3)	0·23 (5)	88·62	0·405	
		cpx	19	48·70 (79)	0·77 (20)	n.d.	5·11 (119)	8·65 (33)	0·71 (9)	n.d.	13·23 (57)	19·35 (50)	0·46 (7)	n.d.	n.d.	97·00	0·732	
PU1061	950	glass	29	53·24 (34)	0·90 (8)	n.d.	17·69 (20)	6·10 (14)	0·27 (3)	n.d.	2·21 (7)	6·83 (8)	2·91 (10)	1·52 (5)	0·21 (2)	91·87	0·393	
		amp	25	41·57 (16)	2·26 (18)	n.d.	14·79 (30)	11·45 (42)	0·33 (4)	n.d.	13·13 (20)	10·48 (20)	2·17 (6)	0·85 (4)	0·04 (2)	97·09	0·671	
		gar	10	38·75 (21)	0·55 (17)	n.d.	22·38 (21)	19·13 (33)	2·09 (21)	n.d.	9·23 (43)	7·58 (38)	0·03 (2)	0·01 (1)	0·05 (1)	99·79	0·462	
		cpx	7	51·60 (103)	0·65 (8)	n.d.	5·50 (99)	10·62 (93)	0·84 (19)	n.d.	12·99 (52)	18·89 (34)	0·53 (8)	0·04 (1)	0·01 (1)	101·66	0·685	
PU1063	900	glass	12	54·23 (43)	0·48 (3)	n.d.	16·86 (14)	3·74 (12)	0·09 (2)	n.d.	0·97 (5)	5·28 (8)	2·92 (5)	1·70 (5)	0·28 (3)	86·56	0·317	
		amp	5	40·62 (44)	2·14 (18)	n.d.	15·94 (21)	15·18 (21)	0·26 (4)	n.d.	9·93 (17)	10·41 (28)	2·14 (8)	0·92 (5)	0·03 (1)	97·57	0·538	
		gar	8	36·83 (29)	1·37 (11)	n.d.	21·06 (18)	22·12 (41)	1·69 (9)	n.d.	6·06 (50)	9·29 (22)	0·04 (1)	0·01 (1)	0·06 (3)	98·83	0·328	
		plg	31	48·84 (102)	0·02 (1)	n.d.	34·09 (104)	0·48 (8)	0·01 (1)	n.d.	0·02 (1)	16·97 (58)	2·07 (16)	0·07 (1)	0·01 (1)	102·70		0·819
		ilm	13	0·04 (1)	43·46 (124)	n.d.	0·65 (5)	51·50 (115)	0·40 (3)	n.d.	2·34 (10)	0·17 (2)	0·01 (1)	0·02 (1)	0	98·37	0·063	
PU1065	850	glass	29	58·74 (30)	0·38 (3)	n.d.	16·32 (27)	2·65 (12)	0·06 (3)	n.d.	0·68 (3)	4·68 (6)	2·92 (5)	2·13 (4)	0·19 (4)	88·75	0·314	
		gar	35	38·50 (55)	1·21 (16)	n.d.	21·43 (26)	23·42 (41)	1·46 (12)	n.d.	5·42 (27)	8·92 (43)	0·04 (1)	0·01 (1)	0·07 (2)	100·48	0·290	
		plg	22	49·20 (40)	0·03 (1)	n.d.	33·29 (57)	0·23 (3)	0·01 (1)	n.d.	0·01 (1)	16·10 (52)	2·39 (13)	0·08 (1)	0·03 (1)	101·37		0·788
		ilm	8	0·13 (3)	51·90 (15)	n.d.	0·28 (2)	43·09 (8)	0·41 (2)	n.d.	2·65 (5)	0·17 (2)	0·02 (2)	0·02 (1)	0·02 (2)	98·68	0·099	
		apa	6	0·31 (14)	n.d.	n.d.	0·06 (5)	0·73 (7)	n.d.	n.d.	0·20 (3)	53·80 (33)	n.d.	n.d.	45·07 (34)	99·92		
PU1067	800	glass	12	59·77 (65)	0·18 (4)	n.d.	14·49 (13)	1·65 (5)	0·03 (2)	n.d.	0·34 (2)	3·10 (2)	3·46 (5)	2·62 (5)	0·11 (2)	85·75	0·268	
		amp	17	43·21 (125)	1·68 (19)	n.d.	15·05 (90)	18·77 (66)	0·37 (8)	n.d.	7·63 (36)	9·92 (28)	1·90 (7)	0·81 (12)	n.d.	99·35	0·420	
		gar	19	38·26 (84)	1·03 (14)	n.d.	21·13 (28)	25·46 (57)	1·64 (17)	n.d.	3·54 (27)	9·26 (62)	n.d.	n.d.	n.d.	100·32	0·198	
		plg	18	56·22 (65)	n.d.	n.d.	29·95 (56)	0·24 (7)	n.d.	n.d.	n.d.	11·54 (41)	5·41 (26)	0·04 (3)	n.d.	103·41		0·541

(continued)

Table 4: Continued

Run #	T (°C)	phase	#	SiO_2	TiO_2	Cr_2O_3	Al_2O_3	FeO	MnO	NiO	MgO	CaO	Na_2O	K_2O	P_2O_5	Total	x_{Mg}	x_{An}
		ilm	10	0·38 (6)	49·45 (67)	n.d.	0·41 (4)	48·45 (80)	0·30 (9)	n.d.	0·30 (9)	1·37 (5)	0·16 (4)	n.d.	n.d.	100·51	0·048	
PU1071	750	glass	18	61·50 (24)	0·06 (2)	n.d.	13·64 (8)	0·86 (9)	0·08 (2)	n.d.	0·37 (2)	2·56 (7)	2·96 (10)	2·94 (7)	0·10 (3)	85·01	0·434	
		gar	16	35·99 (83)	0·03 (3)	n.d.	20·49 (36)	34·64 (50)	1·84 (14)	n.d.	2·74 (9)	0·80 (5)	n.d.	n.d.	n.d.	96·52	0·124	
		plg	18	54·61 (83)	n.d.	n.d.	27·25 (25)	0·22 (8)	n.d.	n.d.	n.d.	10·05 (20)	5·43 (9)	0·03 (2)	n.d.	97·58		0·506
		mag	14	0·32 (9)	18·37 (179)	n.d.	0·99 (17)	67·75 (115)	0·25 (10)	n.d.	0·13 (4)	0·49 (7)	n.d.	n.d.	n.d.	88·30	0·003	
FC Mb C-Pt																		
rk3	1230	glass	8	46·75 (29)	0·88 (2)	0·15 (2)	15·00 (10)	8·70 (16)	0·14 (2)	n.d.	10·59 (11)	12·20 (8)	1·47 (3)	0·49 (2)	n.d.	96·37	0·712	
		ol	10	40·47 (20)	0·02 (2)	0·11 (2)	0·06 (1)	12·50 (17)	0·19 (3)	n.d.	47·05 (26)	0·33 (2)	0·03 (4)	0·01 (1)	n.d.	100·76	0·870	
		sp	4	0·33 (25)	0·39 (5)	38·19 (676)	31·29 (619)	14·43 (77)	0·00	n.d.	15·68 (140)	0·15 (9)	0·02 (1)	0·01 (1)	n.d.	100·48	0·659	
rk6	1200	glass	10	47·79 (13)	1·13 (4)	n.d.	17·60 (15)	9·76 (16)	0·18 (2)	n.d.	8·05 (24)	11·22 (6)	2·02 (6)	0·73 (1)	n.d.	98·49	0·595	
		ol	11	39·97 (19)	0·02 (1)	n.d.	0·07 (2)	16·96 (13)	0·23 (2)	n.d.	44·24 (24)	0·34 (3)	0·01 (1)	0·01 (1)	n.d.	101·85	0·823	
		cpx	12	51·00 (34)	0·51 (3)	n.d.	7·21 (37)	5·65 (20)	0·17 (2)	n.d.	17·11 (23)	19·81 (56)	0·31 (3)	0·01 (1)	n.d.	101·79	0·844	
rk11	1170	glass	10	46·41 (64)	1·19 (3)	n.d.	17·99 (30)	9·17 (13)	0·22 (3)	n.d.	7·27 (8)	10·10 (13)	2·09 (15)	0·74 (2)	n.d.	95·17	0·586	
		cpx	10	49·39 (92)	0·60 (5)	n.d.	7·97 (60)	5·70 (24)	0·20 (2)	n.d.	15·70 (43)	19·49 (43)	0·38 (2)	0·01 (1)	n.d.	99·42	0·831	
rk13	1140	glass	7	48·07 (37)	1·39 (4)	n.d.	18·43 (37)	10·58 (15)	0·21 (2)	n.d.	5·56 (10)	8·69 (10)	2·65 (27)	1·08 (4)	n.d.	96·65	0·484	
		cpx	7	48·64 (41)	0·92 (15)	n.d.	8·41 (74)	8·67 (32)	0·27 (3)	n.d.	15·15 (40)	17·17 (48)	0·50 (6)	0·02 (1)	n.d.	99·75	0·757	
		opx	10	50·20 (66)	0·41 (3)	n.d.	7·71 (41)	14·37 (20)	0·30 (2)	n.d.	25·31 (36)	1·95 (28)	0·07 (2)	0·01 (1)	n.d.	100·32	0·758	
		plg	5	44·12 (127)	0·09 (5)	n.d.	34·08 (99)	0·59 (6)	0·02 (2)	n.d.	0·16 (4)	18·46 (66)	0·95 (30)	0·07 (3)	n.d.	98·55		0·911
		sp	10	0·38 (27)	0·31 (2)	n.d.	62·52 (74)	17·31 (15)	0·14 (2)	n.d.	16·44 (22)	0·20 (6)	0·04 (3)	0·01 (1)	n.d.	97·34	0·629	
rk55	1110	glass	5	48·16 (15)	2·10 (5)	n.d.	17·15 (35)	13·80 (67)	0·32 (6)	n.d.	3·35 (11)	6·65 (16)	3·17 (4)	1·73 (9)	n.d.	96·43	0·302	
		cpx	9	47·88 (37)	1·34 (11)	n.d.	7·79 (48)	13·83 (65)	0·51 (6)	n.d.	12·49 (31)	14·86 (43)	0·57 (5)	0·05 (4)	n.d.	99·32	0·617	
		opx	9	49·33 (75)	0·62 (7)	n.d.	6·29 (83)	20·93 (49)	0·56 (4)	n.d.	19·59 (48)	2·29 (32)	0·10 (3)	0·01 (1)	n.d.	99·72	0·625	
		plg (high An)	5	43·97 (125)	0·27 (13)	n.d.	35·35 (142)	0·53 (5)	0·05 (2)	n.d.	0·10 (8)	18·57 (120)	0·69 (46)	0·09 (8)	n.d.	99·60		0·931
		plg (low An)	4	52·93 (56)	0·08 (2)	n.d.	29·68 (25)	0·55 (4)	0·01 (1)	n.d.	0·06 (1)	11·99 (49)	4·48 (23)	0·42 (4)	n.d.	100·19		0·582
rk64	1080	glass	10	51·19 (38)	1·90 (8)	n.d.	16·27 (19)	12·22 (30)	0·20 (4)	n.d.	1·89 (6)	5·27 (11)	3·92 (13)	2·67 (5)	n.d.	95·51	0·216	
		cpx	9	47·32 (60)	1·17 (14)	n.d.	6·07 (80)	19·60 (69)	0·51 (5)	n.d.	10·88 (44)	12·87 (62)	0·60 (3)	0·03 (1)	n.d.	99·05	0·497	
		plg	9	56·48 (78)	0·08 (1)	n.d.	26·83 (38)	0·60 (9)	0·01 (1)	n.d.	0·05 (2)	9·46 (61)	5·92 (29)	0·80 (8)	n.d.	100·22		0·448
		ilm	4	0·06 (1)	50·25 (56)	n.d.	0·49 (2)	42·05 (35)	0·49 (4)	n.d.	2·90 (5)	0·19 (2)	0·03 (2)	0·05 (1)	n.d.	96·50	0·109	
		gar	6	37·63 (22)	1·22 (37)	n.d.	20·42 (41)	25·05 (43)	1·09 (8)	n.d.	6·49 (37)	7·55 (32)	0·03 (2)	0·00	n.d.	99·48	0·316	

All Fe as FeO. Units in parentheses indicate standard deviations (2σ) from averaged analysis [i.e. 46·75(29) should be read as 46·75 ± 0·29 wt %]; #, number of individual spots averaged for each phase composition reported. Abbreviations are as for Table 2; x_{Mg} = molar [MgO/(MgO + FeO_{tot})]; x_{An}, anorthite content of plagioclase = molar [Ca/(Ca + Na + K)].

considered acceptable, thus, we consider the experiment as (nearly) closed system regarding iron. This also applies to the Pt–graphite double-capsule experiments, where all but three experiments lost less than 10% Fe relative, the three exceptions being the highest temperature run (PU72, 1350°C) and two replicates at 1120°C (equilibrium, P1121 and 1122), which lost 12 and 20% Fe relative. Hydrogen loss (or gain) by diffusion through the noble metal capsule will significantly influence the ambient fO_2 conditions in the noble metal capsule experiments, either reducing it through hydrogen gain or increasing it by loss to the outer capsule or assembly (Luth, 1989). In the Pt–C experiments, hydrogen loss results in increased CO_2 contents through the reaction $H_2O + C = H_2$ (lost) $+ CO_2$. A general feature of the experiments conducted under oxidizing conditions at temperatures of less than 1090°C is the presence of bubbles (Figs 1 and 2), which become more frequent and generally larger with decreasing temperature and increasing nominal H_2O contents in the liquid phase (up to 11·6 wt %, PU1072). The solubility of pure H_2O exceeds the amounts of H_2O added to the starting material as well as the amounts calculated and determined for the residual liquids in the respective charges. The solubility of H_2O in basalts exceeds 8 wt % already at 0·5 GPa and is estimated to be ~18 wt % for basalts at 1 GPa (Newman & Lowenstern, 2002; Botcharnikov *et al.*, 2005; Iacono-Marziano *et al.*, 2012); for rhyolite the pure H_2O solubility exceeds 15 wt % at 1 GPa, extrapolating the equation of Zhang (1999) beyond 0·8 GPa. The nominally added H_2O contents amount to 3·0 ± 0·3 wt % for the initial high-Mg basalt and reach 11·6 wt % for the final rhyolite (PU1072, 750°C), taking into account the liquid and hydrous phase proportions (amphibole) in lower temperature runs. These values are considerably lower than the inferred solubility limits of pure H_2O. The presence of bubbles is most probably caused by the presence of additional fluid components with much lower solubility than H_2O, resulting in the exsolution of a mixed volatile phase at pressure–temperature conditions far below the H_2O-saturation of the respective liquid phase. The most likely candidate is CO_2, although this is not verified to date. We attempted to avoid any potential CO_2 contamination of the starting material during preparation and welding by employing $NaSi_2O_7$ and $KAlSi_3O_8$ as sources for Na_2O and K_2O instead of commonly used carbonates, and used only $CaCO_3$ as a calcium source initially. Using wollastonite ($CaSiO_3$) did not change the results. The problem, however, might be related either to carbon introduced from the tip of the carbon electrode of the welder used in most of this study, the diffusion of carbon from the graphite furnace through the noble metal container (e.g. Brooker *et al.*, 1998; Jakobsson, 2012), or absorbance of CO_2 by the very-fine grained, and thus very reactive, starting material leading to the formation of hydromagnesite despite the fact that the starting material was stored in a desiccator and heated to 110°C before loading. CO_2 contents required to saturate the liquids at 1·0 GPa with a mixed H_2O–CO_2 fluid range between 5200 ppm at 5·8 wt % H_2O in a basalt and 7000 ppm at 11·6 wt % in a rhyolite based on calculations using VolatileCalc (Newman & Lowenstern, 2002), extrapolating beyond its nominal application range of 0·5 GPa. The natural high-Mg basalt RC158c contained 500 ppm CO_2 (measured by coulometric titration); thus, even in this case additional CO_2 had to be present during the experiments (EQ Mb AuPd series). The companion study at 0·7 GPa (Nandedkar *et al.*, 2014) revealed bubbles in nominally H_2O-undersaturated experiments, with the significant difference that in the latter study any carbonates were avoided in the starting materials for the fractional crystallization experiments and a W-based electrode has been used for welding the AuPd capsules, eliminating two of the four above-mentioned potential carbon sources. Alonso-Perez *et al.* (2009) determined the CO_2 contents of their vitrified starting oxide mixes prepared exactly in the same way as the present synthetic starting material (they used composition F8a of this study) and obtained 9100 ± 200 ppm CO_2 in their nominally CO_2-free starting materials ranging in H_2O content from 6·2 to 9·4 wt %.

The case for the equilibrium crystallization experiments employing graphite capsules is different. The natural starting material contained only 500 ppm of CO_2, but the starting material is rather oxidized and assuming that all ferric iron (3·25 wt % Fe_2O_3) is converted to ferrous iron via the reaction $2Fe_2O_3 + C = 4FeO + CO_2$ produces an additional 4500 ppm of CO_2, resulting in 5000 ppm CO_2 that will drive volatile saturation at 1·0 GPa to about 7·0 wt % H_2O, consistent with the observation that run P1060 with 6·7 wt % H_2O determined by Raman spectroscopy is just about fluid-saturated. The H_2O contents calculated from the amount of H_2O in the starting material with the H_2O content obtained by the by-difference method using an internal mineral standard (clinopyroxene) for correction of the melt analysis totals is shown in Fig. 3. The diagram reveals a consistent variation along a 1:1 correlation up to 6 wt % corresponding to 1090°C. The highest values clearly deviate; the nominal values are higher than the calculated values. The upper limit of H_2O contents around 10–11 wt % in the liquid is most probably the result of CO_2 contamination limiting the amount of dissolved H_2O in the silicate liquid.

In summary, we observe small amounts of vapor or fluid bubbles in experiments conducted at temperatures <1080°C that we attribute to CO_2 absorption by the very fine-grained oxide–silicate starting materials and/or the reaction of oxidized starting materials with graphite. However, the amount of calculated CO_2 in our experiments is small compared with the amount of H_2O (always <5 mol % of the total volatile concentration). With the exception of the fractional crystallization experiments in Pt–C double capsules, all experiments were successful in maintaining the attempted H_2O contents in our charges and neither gained nor lost significant amounts of hydrogen through diffusion through the

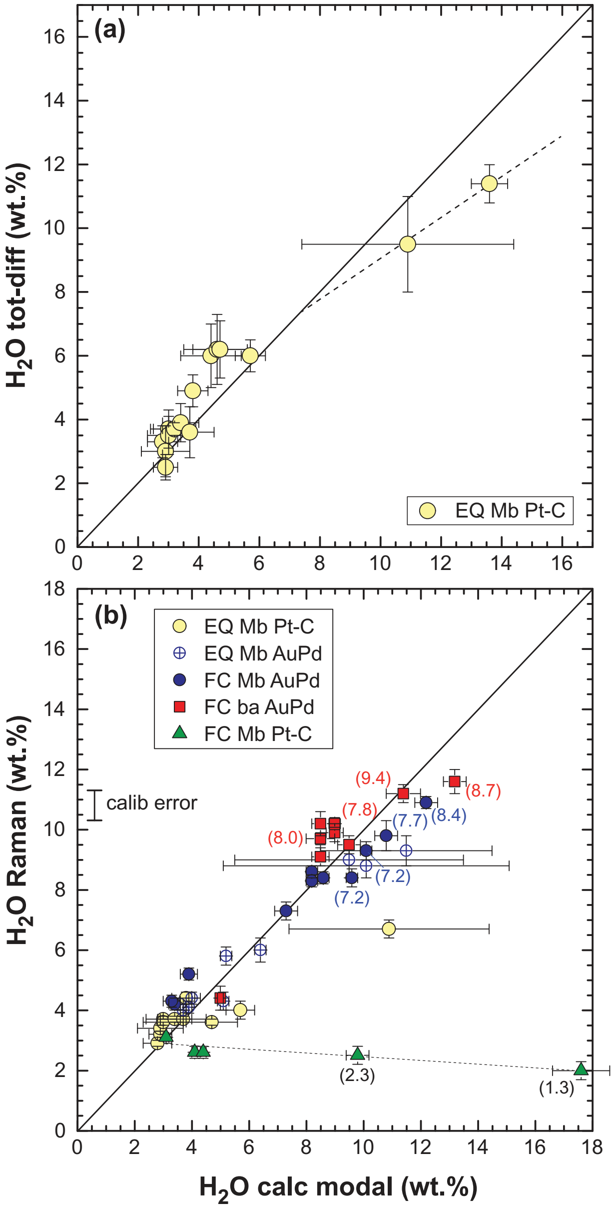

Fig. 3. Comparison of H_2O contents (wt %) determined by (a) the difference method and (b) Raman spectroscopy with nominal H_2O contents calculated from the amount contained in the starting material, the melt fraction of the respective experiment corrected for amphibole modal amounts (assuming 2·1 wt % H_2O in amphibole, H_2O calc modal). In (a), microprobe totals of the glass phase were corrected to cpx totals using an external standard and assuming cpx totals are 99·6–99·9 wt %. In (b), numbers in parenthesis indicate H_2O contents calculated for the same experiments with the Waters & Lange (2015) plagioclase–melt hygrometer. Raman result for experiment P1060 (10·9 wt % modal, 6·7 wt % Raman) is unreliable because of interference with additional (solid) phases. The fractional crystallization experiments under reducing conditions (FC Mb Pt–C) experienced significant H_2O loss (for details see text). 'Calib error' denotes approximate accuracy of Raman H_2O determination based on calibration with 20 in-house standards.

noble metal containers. This is demonstrated in Fig. 3b, which shows a comparison of the nominal H_2O content calculated from the initially loaded amount of H_2O (as hydroxide, rarely as additional H_2O added by micro-syringe when the amount of hydroxide was insufficient) and the modal proportions of the liquid phase (and amphibole if present) with the H_2O content determined by micro-Raman spectroscopy (Table 2). Maximum H_2O contents of 11·6 wt % in the presence of a fluid phase for the final rhyolite at 750°C (PU1072) are consistent with a CO_2 content of *c.* 7000 ppm. Overall estimated minimum CO_2 contents for experiments that are fluid saturated (i.e. all experiments below 1080°C under oxidized conditions) are in the range of 4500–7000 ppm, increasing with decreasing temperature. As an additional test, we calculated the amount of H_2O in the liquids coexisting with plagioclase utilizing the hygrometer of Waters & Lange (2015) for all runs that contained plagioclase. All fractional crystallization experiments that contained plagioclase consistently provided H_2O contents about 10–20% lower than the values obtained by Raman spectroscopy and the nominal values (Fig. 3b), but confirmed that high H_2O contents close to the nominal values were present in these experiments. However, fractional crystallization experiments in Pt–C capsules have lost most H_2O and will be discussed below.

The attainment of equilibrium in the fractional crystallization experiments is facilitated by large liquid proportions always exceeding 75% in the oxidized experiments, very fine-grained starting materials (<10 μm grain size) and run durations optimized for equilibration versus iron and hydrogen loss that varied from 3·5 h at the highest to 212 h (9 days) at lowest temperatures. Elevated H_2O concentrations further enhanced diffusional equilibration. Overheating of the starting materials to generate homogeneous liquids was avoided to circumvent the formation of metastable phases that are reluctant to dissolve and/or re-equilibrate at lower temperatures. Runs were first pressurized to 0·4 GPa and then heated at a rate of 30–50°C min^{-1} with concomitant increase of pressure and directly brought to run temperature. Attainment of equilibrium can further be evaluated through the following considerations.

1. Solid and liquid phases show homogeneity. For the liquid (glass) phase 5–40 individual analyses were obtained from all experiments. Liquids were analyzed throughout the entire capsule and we did not find any statistically significant variation in any of the runs. Solid phases are generally homogeneous with the exception of some sector zoned high-Ca clinopyroxene (cpx) and low-Ca orthopyroxene (opx) with low-Al and high-Al sectors, a feature that is often observed both in experimental studies (e.g. Sisson & Grove, 1993; Nandedkar *et al.*, 2014) and in field occurrences (e.g. Dessimoz *et al.*, 2012; Hürlimann *et al.*, 2016) in basaltic to andesitic systems and is not necessarily an expression of disequilibrium but might be related to relatively rapid growth of pyroxenes (e.g. Schwandt & McKay, 2006) in a specific temperature window, in the present

case between 1150 and 1180°C for cpx and 1090 and 1120°C for opx.

2. Textures in experimental charges indicate well-crystallized, unzoned, idiomorphic solid phases in most but the lowest temperature experiments where amphibole occasionally shows some limited core–rim zoning (Figs 1 and 2).
3. Major element partitioning, in particular Fe–Mg (Table 2), is very consistent, with values of 0·30 ± 0·02 to 0·35 ± 0·03 for olivine in graphite–Pt experiments and 0·23–0·26 in fractional experiments in AuPd capsules; likewise, Fe–Mg K_d values vary very little for cpx and opx within a given series, always with the exception of the equilibrium crystallization experiments in AuPd capsules.
4. Quench crystallization is limited in the fractional crystallization experiments, with rare feathery overgrowth of olivine, cpx and amphibole on stable crystals that are easily identified in BSE images, but becomes much more abundant in the equilibrium crystallization experiments, in particular at higher temperatures (see Fig. 1a and b), to the extent that only composition can clearly distinguish between stable and quench cpx (very high Al, and variable Ca and Fe/Mg contents).

The attainment of near constant $f\text{O}_2$ in the fractional and the equilibrium crystallization experiments in graphite–Pt capsules (which are truly buffered) at the intended values corresponding to NNO and close to the H_2O maximum in the C–COH system cannot be strictly validated. However, in all experiments that contained olivine the apparent Fe^{2+}–Mg partitioning assuming that olivine accommodates only ferrous iron provides a constraint on the relative $f\text{O}_2$ (Fig. 4). The equilibrium and fractional crystallization experiments in Pt–C capsules result in K_d(ol–liq) values that are independent of temperature and vary within error around the preferred value of 0·324 at 1·0 GPa (Ulmer, 1989). The more oxidized experiments in AuPd alloys show significantly lower apparent K_d; the fractional ones where only a few experiments contained olivine scatter around 0·24, whereas the equilibrium crystallization experiments show a systematic decrease of the K_d with decreasing temperature.

Phase relations and phase proportions

The discussion of the phase relations and compositions is strictly limited to the results from the inner capsules in the case of a noble metal double-capsule setup, as the outer capsule was generally made of AuPd alloys with higher proportions of Pd or even of Pt and not Fe-pre-saturated, resulting in much increased Fe loss exceeding 50% in some high-temperature runs. In addition, the outer capsule was much larger and, thus, was subjected to a larger thermal gradient that in some cases resulted in the crystallization of additional (lower temperature) phases at the extremities of the capsule. Nevertheless, the phase equilibria observed in the outer capsules were consistent with and in most cases were identical to the data obtained from the inner capsules and served as control, in particular to detect potential volatile loss from the inner capsules. We first present the results of the oxidized (AuPd) experiments followed by the more reduced experiments that have less significance for the differentiation of arc-type primary magmas. The reduced fractional crystallization experiments contained low H_2O and represent a case of 'damp' (about 2–3 wt % H_2O) differentiation at $f\text{O}_2$ conditions more probably representing arc-tholeiitic differentiation. However, near anhydrous tholeiitic differentiation trends related to H_2O-poor melts generated by decompression in the sub-arc mantle have been described from several subduction-related systems (e.g. Sisson & Bronto, 1998; Grove *et al.*, 2002, 2005; Le Voyer *et al.*, 2010) and therefore the 'damp' experiments provide crucial information on the lower crustal differentiation of such magmas in subduction-zone settings. Summaries of the instantaneous solid compositions (ISC) of the fractional crystallization experiments depicting the mineral phases and their modal proportions crystallizing in every fractionation step as well as the total solid composition (TSC) are given in Figs 5–7.

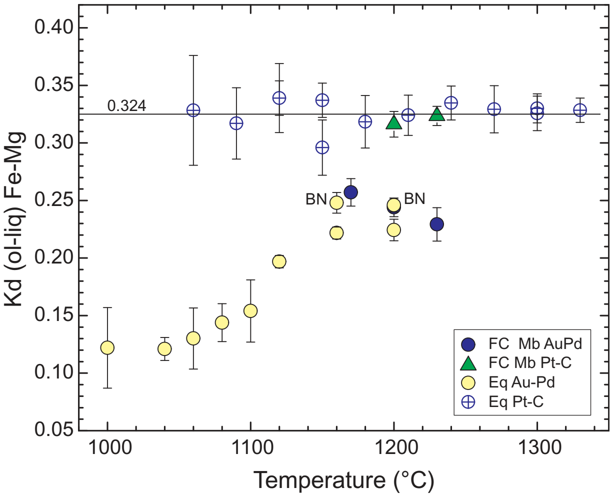

Fig. 4. Fe–Mg partitioning between olivine and coexisting liquid. The distribution coefficient [$K_\text{d} = (\text{FeO}/\text{MgO})_\text{liquid}/(\text{FeO}/\text{MgO})_\text{olivine}$] was calculated for FeO = Fe_total. The value of 0·324 corresponds to the value of Ulmer (1989) for 1 GPa assuming all Fe = Fe^{2+}. Experiments labelled BN were conducted with BN spacers surrounding the AuPd–Pt capsule. Error bars are propagated from averages of individual olivine and liquid analyses (Tables 3 and 4).

Basaltic andesite (85-44, ba) experiments

The liquidus temperature of the initial starting composition (85-44, 5 wt % H_2O) was bracketed at 1215 ± 15°C with orthopyroxene (opx) as the liquidus phase. This is consistent with the data of Baker *et al.* (1994) and Müntener *et al.* (2001), who conducted equilibrium crystallization experiments at 1 and 1·2 GPa under more reducing (closer to C–COH) conditions and located the liquidus at 1·0 GPa between 1260°C for 3 wt % H_2O and

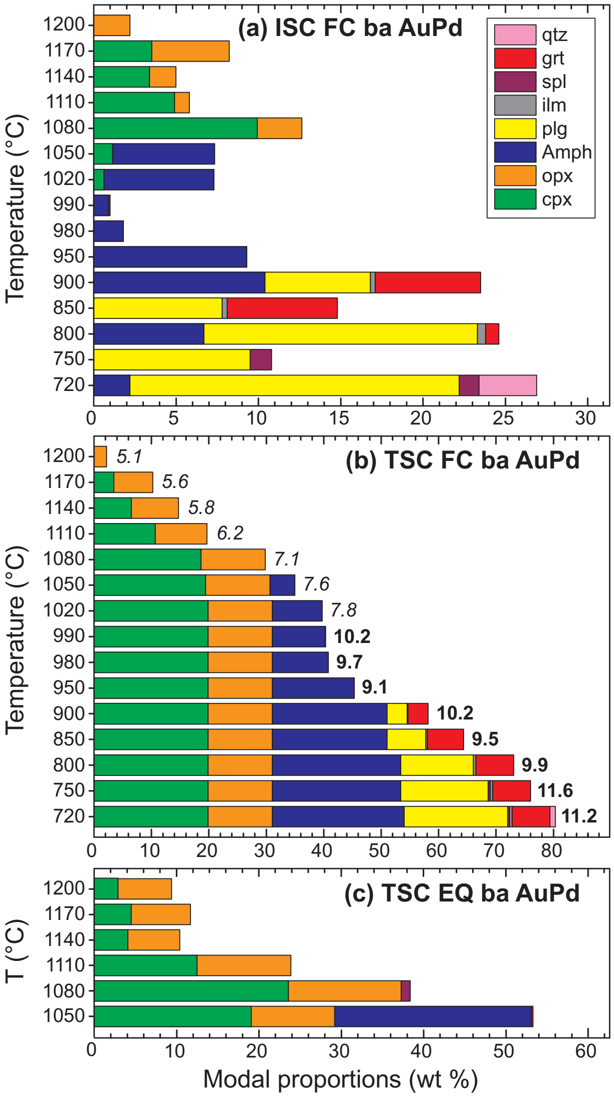

Fig. 5. Modal proportions of solid phases in experiments on the high-Mg, basaltic andesite (85-44) initial composition. (a) ISC (instant solid composition) of the single temperature steps of the fractionation experiments (FC ba AuPd) at 1 GPa under oxidizing conditions. (b) TSC (total solid composition; summarized modal fractions of all previous steps normalized to mass of initial basaltic andesite) $TSC_n{}^m = TSC_{n-1}{}^m + ISC_n{}^m \times AMF_{n-1}$ with $AMF_n = IMF_n \times AMF_{n-1}$, where $TSC_n{}^m$ is total of mineral m for experiment n, $ISC_n{}^m$ is instantaneous fraction of mineral m for experiment n, IMF_n is instantaneous melt fraction of experiment n, and AMF is accumulated melt fraction of experiment n. The difference from 100 corresponds to amount of liquid left relative to start. Numbers on bars indicate H_2O content of liquids determined by Raman spectroscopy (bold) or nominal H_2O contents calculated from starting materials (italic) (see Table 2 for details). (c) TSC of equilibrium crystallization experiments at 1·2 GPa and 5 wt % H_2O taken from Müntener *et al.* (2001).

opx as the liquidus phase, 1190°C for 6 wt % H_2O and olivine (ol) as the liquidus phase, and above 1230°C at 1·2 GPa with opx and cpx. More reducing conditions increase the liquidus temperature for constant H_2O contents (Kägi *et al.*, 2005). The second phase to crystallize together with opx is high-Ca clinopyroxene (cpx) at 1170°C; this assemblage dominated by cpx with minor

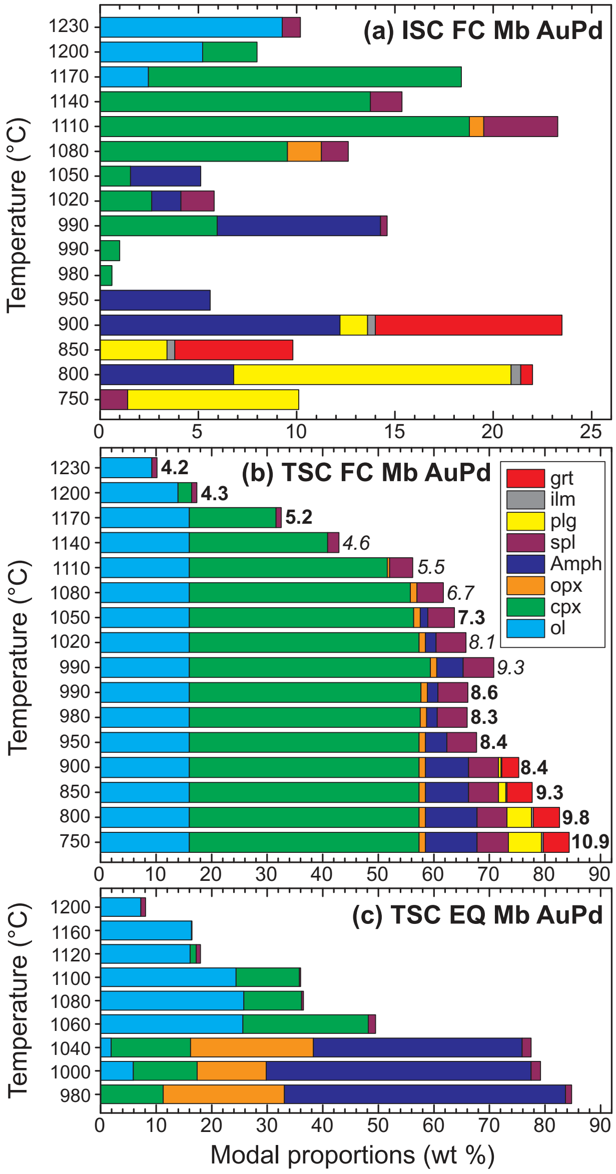

Fig. 6. Modal proportions of solid phases in experiments on the high-Mg basalt (RC158c) initial composition under oxidizing conditions. (a) ISC of the single temperature steps of the fractionation experiments (FC Mb AuPd) at 1 GPa; (b) corresponding TSC (for explanation see Fig. 5); (c) TSC of equilibrium crystallization experiments at 1·0 GPa under oxidizing conditions (EQ Mb AuPd).

opx persists until 1050°C, where opx disappears and amphibole begins to crystallize; both phases form the liquidus assemblage down to 990°C, where it coexists with an andesitic liquid. Neither Fe–Ti-oxides nor plagioclase or garnet were observed in the crystallization interval from high-Mg basaltic andesite to andesite or dacite. The disappearance of opx at the onset of amphibole crystallization indicates an amphibole reaction boundary opx (± cpx) + liq = amph. Between 980 and 1000°C amphibole and minor Ti-bearing magnetite are the liquidus phases. At 950°C, garnet joins the assemblage, forming euhedral overgrowth rims on the almandine seeds, whereas plagioclase seeds nearly

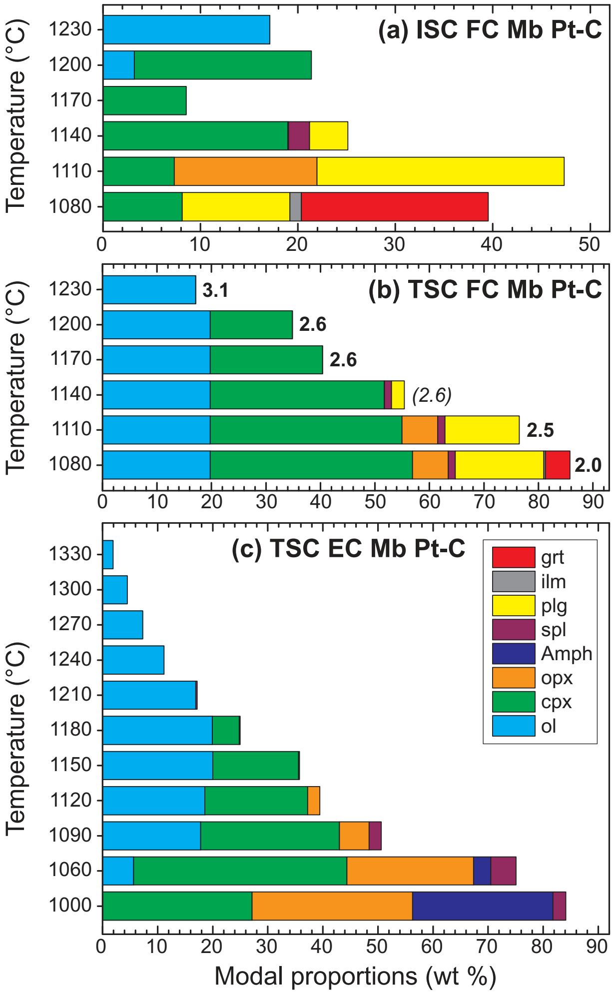

Fig. 7. Modal proportions of solid phases in experiments on the high-Mg basalt (RC158c) initial composition under reducing conditions. (a) ISC of the single temperature steps of the fractionation experiments (FC Mb Pt–C) at 1 GPa; (b) corresponding TSC; numbers indicate H_2O contents of liquids determined by Raman spectroscopy, except for the run at 1140°C, where the value was estimated by the difference method; (c) TSC of equilibrium crystallization experiments at 1·0 GPa under reducing conditions (EQ Mb Pt–C).

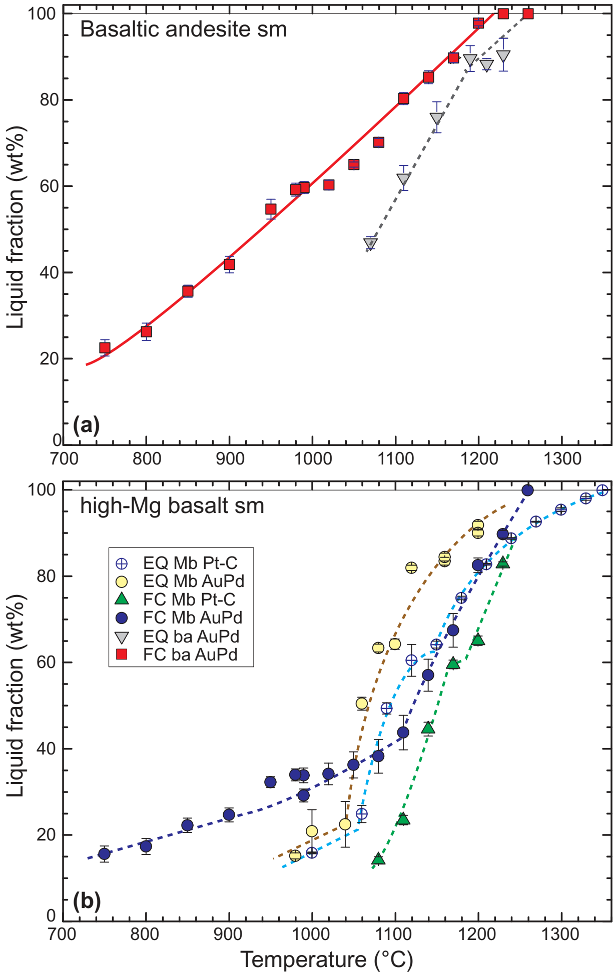

Fig. 8. Liquid fraction as a function of run temperature. (a) High-Mg basaltic andesite (ba) series; fractional crystallization experiments show near-linear variation of melt fraction with temperature. For comparison the equilibrium crystallization experiments at 1·2 GPa for the same initial composition (85-44) with 5 wt % H_2O are taken from Müntener *et al.* (2001). (b) High-Mg basalt (Mb) series depicting distinctly non-linear trends with characteristic shifts linked to fO_2 conditions and H_2O content. (For explanation see text.) EQ and FC denote equilibrium and fractional crystallization experiments. Mb and ba represent (initial) starting compositions (Mb is high-Mg basalt, RC158c, 3 ± 0·3 wt % H_2O; ba is high-Mg basaltic andesite, 85-44, 5 wt % H_2O; Table 1). Pt–C and AuPd denote capsule material (and fO_2 conditions): Pt–C, graphite capsules in outer Pt capsules (reducing); AuPd, Au–Pd single- or double-capsule arrangement (oxidizing). Error bars correspond to standard deviations from mass-balance calculations of modal proportions (Table 2).

completely dissolved, implying that this composition (990 ba) is very close to plag saturation and saturated in garnet. At 900°C, amph–garnet–plag and ilmenite form the stable assemblage coexisting with an andesite or dacite liquid. This assemblage persists to 750°C, with apatite joining at 850°C. At 850°C no amphibole was observed, but at 800°C amphibole was stable again. This situation is not uncommon in stepwise fractional crystallization experiments where the (re-mixed) derivative composition for the next, lower temperature run can slightly deviate from the multiply saturated LLD, resulting in appearance and disappearance of phases. This is graphically illustrated in the discussion, where pseudoternary phase diagrams are presented. Finally, at 720°C corresponding to the outer capsule of run PU1072 in the cold end of the large capsule, quartz and ulvöspinel join the assemblage (the latter at the expense of ilmenite). At the lowest temperatures, 720–750°C, garnet seeds reveal very subtle overgrowth rims that were difficult to impossible to analyze. Amphibole was found only at 720°C but not at 750°C.

The melt fractions (Fig. 8a) decrease near linearly from the liquidus to 720°C despite the fact that the crystallizing assemblages change significantly between 1080 and 1050°C where amphibole (amph) replaces opx and cpx (Fig. 5a) and below 950°C where garnet and plagioclase join the fractionating assemblage. Fractional crystallization produces a variety of different ultramafic cumulates, orthopyroxenites, followed by websterites and opx-bearing clinopyroxenites, and (cpx-bearing) hornblendites that are replaced by garnet–hornblende-gabbros below 950°C. A total of 45 wt % ultramafic cumulates (Fig. 5b) need to be extracted to produce an andesitic liquid from a primary high-Mg basaltic andesite. An additional 20% of garnet–hornblende-gabbro generates a rhyodacitic liquid at 850–800°C, and finally at 720–750°C and 80% fractionation a high-silica rhyolite is produced. For comparison, modal proportions and melt fractions of the equilibrium crystallization experiments by Müntener *et al.* (2001) at 1·2 GPa under more reducing conditions but identical H_2O content are provided (Fig. 5c). The inferred liquidus temperature is considerably higher (estimated 70°C), and both opx and cpx form the near-liquidus assemblage, which persists to 1110°C, where it is joined by hercynitic spinel; at 1070°C amphibole (accompanied by a minute amount of garnet) crystallizes at the expense of spinel, cpx and opx, which all decrease in modal amounts implying a peritectic reaction that forms amphibole. The melt fraction versus temperature relationship displays a strong decrease below 1150°C and, with the onset of amphibole crystallization, less than 50% liquid is left (Fig. 8a). This is ~20% less than in the fractional case at the same temperature.

High-Mg basalt (RC158c, Mb) experiments under oxidizing conditions

The liquidus temperature of the fractional crystallization experiments on the high-Mg basalt initial starting composition is located around 1280–1300°C with olivine (Fo 91·1) and minor Cr-rich spinel as the liquidus phase. As Cr was effectively depleted in the coexisting liquid by 1% spinel (sp) crystallization, Cr_2O_3 was not added to subsequent fractionation steps. Cpx joins olivine at 1200°C and hercynitic spinel appears at 1170°C. Olivine disappears at 1140°C whereas opx saturates at 1110°C. The cubic oxide phase changes from abundant hercynitic spinel between 1170 and 1110°C to Ti-bearing, aluminous magnetite (mag) at 1080°C. At 1050°C opx disappears and amphibole starts crystallizing; at 1020 and 990°C amphibole–cpx–Ti-magnetite form the solid assemblage coexisting with a dacitic liquid representing 30–35% of the initial high-Mg basalt (Fig. 8b). The disappearance of opx at the onset of amphibole crystallization points towards a similar amphibole reaction boundary to that in the case of the basaltic andesite series. Several experiments have been repeated in the range 980–1000°C (rk67, PU1048, PU1069) as some inconsistencies in the amount of liquid present were observed. Unfortunately, run rk67 is no longer available, and thus the true H_2O content of this experiment could not be verified, but we assume that this run contained less than the target value of 8·14 wt % in the starting material that should result in 9·3 wt % in the liquid (considering 85·4 wt % melt and 8·3 wt % amphibole with 2·1 wt % H_2O). We therefore repeated the experiments with a newly prepared starting material (990 pb), which gave 8·6 and 8·2 wt % H_2O determined by Raman spectroscopy. Therefore, these two runs were utilized to continue the series of fractional crystallization experiments that resulted in cpx only as liquidus phases. At 950°C amphibole is the dominant mineral, crystallizing together with small amounts of garnet that formed around the almandine seeds. At 900°C plagioclase and ilmenite join the crystallizing assemblage, which persists until 800°C with the exception, as for the basaltic andesite (ba) series, that no amphibole was found at 850°C. At 750°C plagioclase and Ti-magnetite are present with unreacted garnet seeds (no rim, no resorption discernible) coexisting with a rhyolitic liquid.

The following ultramafic cumulates have formed along the LLD from the liquidus to 950°C (Fig. 6a): spinel-bearing dunites, wehrlites, (ol–spl–opx-bearing) clinopyroxenites and finally hornblende-pyroxenites and cpx-hornblendites. The difference in total amount of extracted ultramafic cumulates between the basaltic andesite (45%) and the high-Mg basalt (70%) largely reflects the amount of dunite (17%) extracted from the latter. Below 950°C ilmenite-bearing garnet–hornblende-gabbros form the main cumulates with coexisting liquids evolving from dacite to rhyolite. The evolution of the melt fraction as a function of temperature is no longer near linear as for the basaltic andesite case, but shows a pronounced curvilinear decrease from the liquidus to 1100°C, with a much flatter slope towards lower temperatures when amphibole and later plagioclase and garnet dominate the solid assemblage (Fig. 8b).

Phase assemblages of equilibrium crystallization experiments under oxidizing conditions are displayed in Fig. 6c. These experiments are not directly comparable with the respective fractionation experiments because fO_2 was unconstrained and allowed to vary in a closed system. As mentioned above and presented below, the fO_2 started at a value of *c.* NNO + 2 given by the Fe_2O_3/FeO of the starting material (except for two runs with BN spacers that resulted in about 1 log unit lower fO_2) but increased to NNO + 5·5 with decreasing temperature and melt fraction; that is, it is between +1 to 2 and +3·5 to 4·5 log units higher than in the fractional crystallization experiments. The liquidus is inferred at about 1280°C and the liquidus phases are olivine (Fo 92·0) and Cr-rich spinel; this assemblage persists to 1160°C and at 1120°C cpx joins the liquidus. At 1040°C both amphibole and opx appear and the amount of cpx and olivine sharply decreases. Olivine is lost from the assemblage at 980°C, the lowest temperature at which it coexists with an andesitic liquid at a melt fraction of 15%. Phase relations and modal proportions indicate a peritectic relationship involving both the well-known ol + liq = opx reaction as well as an amphibole-forming reaction (pyx + liq = amph). The evolution of the melt fraction as a function of temperature is different, with higher initial (higher temperature) melt fractions for equilibrium than for fractional crystallization. The relationship is nonlinear and similar to equilibrium crystallization experiments on a near-primary basalt from St Vincent (Lesser Antilles) with 2·3 wt % H_2O (Melekhova *et al.*, 2013). The steepest decrease in melt fraction between 1080 and 1040°C is related to the intersection of the liquidus with the peritectic amphibole reaction boundary leaving only <23% liquid. This shift towards higher melt fractions at elevated temperatures compared with the fractional crystallization experiments is related to the effect of increased fO_2 shifting the onset of cpx crystallization to just above 1120°C compared with 1200°C in the fractional case at NNO. The combination of high H_2O contents and high fO_2 effectively depresses the cpx stability field relative to olivine, keeping the system in the olivine-only field where crystallization is not efficient. With the onset of cpx the melt fraction decreases, additionally enhanced by peritectic reactions that are suppressed by fractional crystallization, resulting in a very different T–f relationship. Cumulates produced by equilibrium crystallization under oxidizing conditions are comparable with the fractional case down to 980°C, but more abundant opx formed as a result of peritectic formation from olivine that has been extracted in the fractional case.

High-Mg basalt (RC158c) experiments under reducing conditions

The fractional crystallization experiments conducted in graphite–Pt capsules (FC Mb Pt–C) are distinct as they lost most of their H_2O in all but the first experiment conducted with the natural high-Mg basalt RC158c. This was already suspected based on the phase equilibria and total solid compositions and the rather high totals of the quenched glass analyses (>95 wt %). The first experiment, rk3, contained the nominal value of 3·1 wt % (Table 2) whereas all other experiments were conducted with derivative starting materials (Table 1) containing H_2O in the form of Al- and Mg-hydroxides. This systematically resulted in glass H_2O contents of 2·0–2·6 wt % (Raman) and 1·3–2·4 wt % (plag-melt, Fig. 3b), despite the fact that with decreasing temperature the amount of H_2O added in the charge increased from 3·2 to 10·7 wt %. Considering the amount of crystallized solids, the liquid should contain H_2O contents ranging from 4·1 to 17·6 wt % (Fig. 3b). Numerous experiments run at identical conditions with the same starting material are very consistent regarding melt composition, melt fractions, modal mineralogy and mineral compositions. A similar behavior was observed in the equilibrium and fractional crystallization experiments of Caricchi *et al.* (2006) employing exactly the same technique, but the problem remained unresolved. The fact that only experiments conducted with starting materials containing H_2O either in the form of $Mg(OH)_2$ (brucite) and $Al(OH)_3$ (gibbsite) or as free H_2O added by micro-syringe showed this behavior, but none of the experiments conducted with the natural high-Mg basalt RC158c that contains H_2O nearly exclusively in amphibole with some minor contribution from chlorite, points towards the availability of free H_2O at low temperature when no melt phase is present. Amphibole most probably decomposes only at the onset of melting in the basaltic starting material and the water is directly incorporated into the melt phase. In the case of Al-hydroxide and possibly also brucite, they decompose partly or completely at less than 400–500°C. The most likely explanation for this unusual behavior is that free H_2O at 400–500°C in equilibrium with graphite and the reduced starting material containing all Fe as ferrous iron in fayalite resulted in the production of hydrogen and methane with near instantaneous hydrogen diffusion out of the capsule. Why a near constant amount of H_2O of 2·0–2·6 wt % was present in the liquid phase in these experiments cannot be resolved, but provides the base to utilize these experiments as a series of ‘damp’ fractionation experiments at low H_2O content and relatively reducing conditions. These experiments might be representative for the differentiation of primary, H_2O-poor mantle melts that occur in suprasubduction settings (e.g. Mt Shasta; Grove *et al.*, 2005), but are much more widespread in mature extensional settings. The liquidus for the hydrous (3·0 ± 0·3 wt %) high-Mg basalt at 1·0 GPa is around 1330°C, the anhydrous liquidus is located about 100°C higher (at 0·1 MPa and 3·0 GPa; Ulmer, 1988). The liquidus phase at 1230°C (i.e. at least 100°C below the inferred liquidus) is olivine (Fo87) plus minor Cr-rich spinel; at 1200 and 1170°C cpx is the dominant phase, and olivine disappears at 1170°C. At 1140°C, both plagioclase (An91) and hercynitic spinel appear. At 1110°C, highly variable plag (An93 core–An58 rim and small crystals dispersed in the melt) coexists with cpx, opx and spinel, and finally at 1080°C, the lowest temperature run conducted in this series, cpx–plag–ilmenite (ilm)–Fe-rich garnet (gar) form the stable assemblage with only 14% of basaltic trachy-andesite liquid left relative to the initial high-Mg basalt. These phase relations are distinct from all other experiments by early saturation of plagioclase that has not been encountered in any other series at 1·0 GPa at temperatures in excess of 950°C, and by garnet saturation at 1080°C as opposed to the oxidized experiments with high H_2O contents where both phases start crystallizing only at or below 950°C from dacitic liquids. Run rk55 at 1110°C shows clear signs of progressive H_2O loss, in particular the strongly zoned plagioclase with high-An cores and low-An rims and abundant low-An microlites most probably demonstrating continuous H_2O loss from the experiment at an early stage. The plag–melt hygrometer results in 2·3 and 1·6 wt % H_2O for high- and low-An plagioclase, indicating that most H_2O was actually lost before plagioclase even nucleated. The melt fraction versus temperature relations are consistent with low H_2O contents (Fig. 8b), illustrated by a shift of the curve to higher temperatures at a given melt fraction and a high df/dT resembling the relationships of fractional crystallization of anhydrous MOR-tholeiite at 1·0 GPa (Villiger *et al.*, 2004).

The equilibrium crystallization experiments, on the other hand, were completely successful in keeping the system closed for H_2O (see Fig. 3) owing to the fact that natural starting material with H_2O is bound exclusively in silicates that decompose only at high temperatures under elevated pressures when a melt phase is already forming. The liquidus (Fig. 7c) is located at 1340 ± 10°C with ol (Fo 90·6) as the liquidus phase, and Cr-rich spinel saturates at 1210°C, followed by cpx at 1180°C and opx at 1120°C. Saturation in opx and decrease in olivine confirm the peritectic relationship of olivine–opx. Aluminous (hercynitic) spinel is present at 1090°C and below. At 1060°C amphibole starts crystallizing and at 1000°C olivine disappears and the modal amount of cpx decreases relative to amph + opx, implying a reaction of the type ol + cpx + liq = opx + amph. The succession of cumulates is comparable with the higher fO_2 equilibrium crystallization experiments except for higher amounts of opx originating from the peritectic reaction(s). The *T*–*f* relationship (Fig. 8b) shows a similar behavior to the oxidized equilibrium crystallization experiments but shifted to higher temperatures. The crystallization rate (d*f*/d*T*) is low during olivine-only crystallization but increases when cpx and opx join the liquidus. The highest crystallization rates are related to amphibole saturation through the inferred peritectic reaction, leaving 16 wt % silica-undersaturated liquid at 1000°C.

Melt compositions

All liquid compositions (Tables 3 and 4) were normalized to 100 wt % anhydrous and are presented as a function of SiO_2 (Fig. 9) and temperature (Figs 10 and 11). Experiments under oxidized conditions evolve from basalt to basaltic andesite and andesite [total alkalis–silica (TAS) diagram, Fig. 9a]; the fractional crystallization series (FC Mb AuPd and FC ba AuPd) evolve further to dacite and finally rhyolite, reaching silica contents of nearly 75 wt % at 720–750°C. For comparison, the results of the equilibrium crystallization experiments at 1·2 GPa for 3·8 and 5·0 wt % added H_2O are provided, which extend from the primary basaltic andesite to rather alkali-rich andesites (Müntener *et al.*, 2001). The equilibrium crystallization experiments on the high-Mg basalt under oxidizing conditions (EQ Mb AuPd) show an evolution towards low total alkali contents related to (1) high melt fractions at rather high silica contents, (2) large amounts of amphibole below 1040°C and (3) analytical difficulties in obtaining correct alkali contents of the small melt pools at lowest temperatures (highest silica contents). The fractional crystallization experiments of the basaltic andesite display lower total alkali contents for a given SiO_2 than the equilibrium crystallization experiments.

Experiments under reducing conditions (Pt–C) reveal a different evolution: both fractional and equilibrium crystallization evolve towards high total alkali contents with restricted silica enrichment leading to trachybasalts and basaltic trachyandesite. This trend is controlled by abundant opx crystallization in the equilibrium case and the low H_2O content of the fractional crystallization experiments that saturate in plagioclase and opx at 1110°C, driving the liquid to lower SiO_2 at increasing alkali contents.

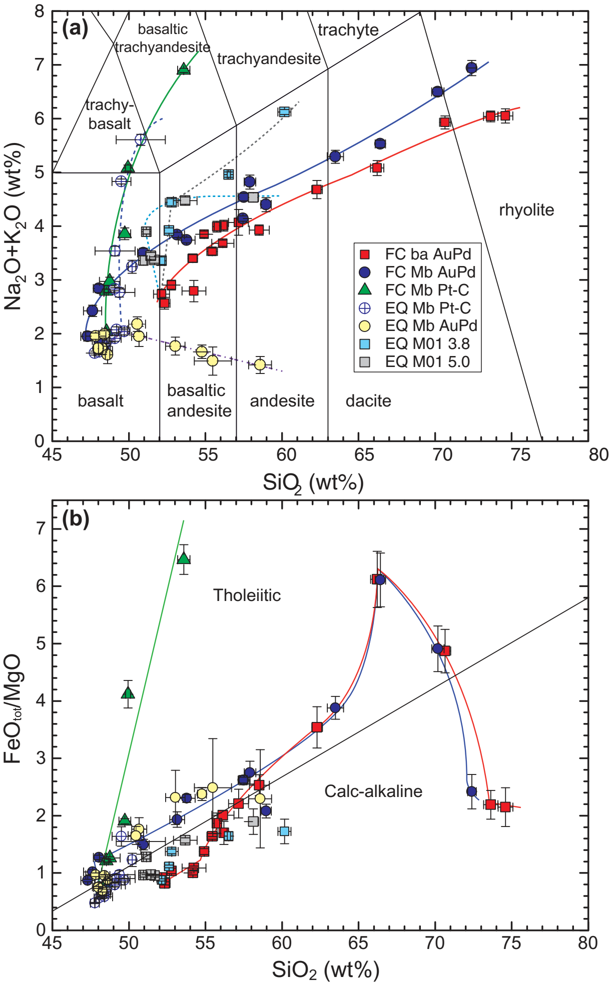

Fig. 9. Liquid compositions plotted in (a) the TAS (total alkali vs silica diagram (Le Maitre *et al.*, 1989) and (b) the FeO/MgO vs SiO_2 (wt %) diagram with the tholeiitic and calc-alkaline fields according to (Miyashiro, 1974). Legend as in Fig. 8; error bars correspond to standard deviations of multiple analyses (Tables 3 and 4).

All but the reduced, low-H_2O fractional crystallization experiments (FC Mb Pt–C) straddle the tholeiitic–calc-alkaline dividing line up to 65 wt % SiO_2, a trend that is rather typical for arc-related hydrous magmas. The lowest temperature fractional crystallization runs (900–720°C) show an evolution first towards higher FeO/MgO ratios, driving them deeply into the tholeiite field down to 850°C, followed by an abrupt inversion to lower ratios back into the calc-alkaline field that is mainly caused by Fe-rich garnet and ilmenite and, in the last step, by Ti-magnetite fractionation. A systematic decrease of the FeO/MgO ratio with increasing SiO_2 as well as with increasing fO_2 was observed at 0·4–0·7 GPa (Pichavant *et al.*, 2002; Sisson *et al.*, 2005) whereas a similar trend with a cross-over from tholeiitic to

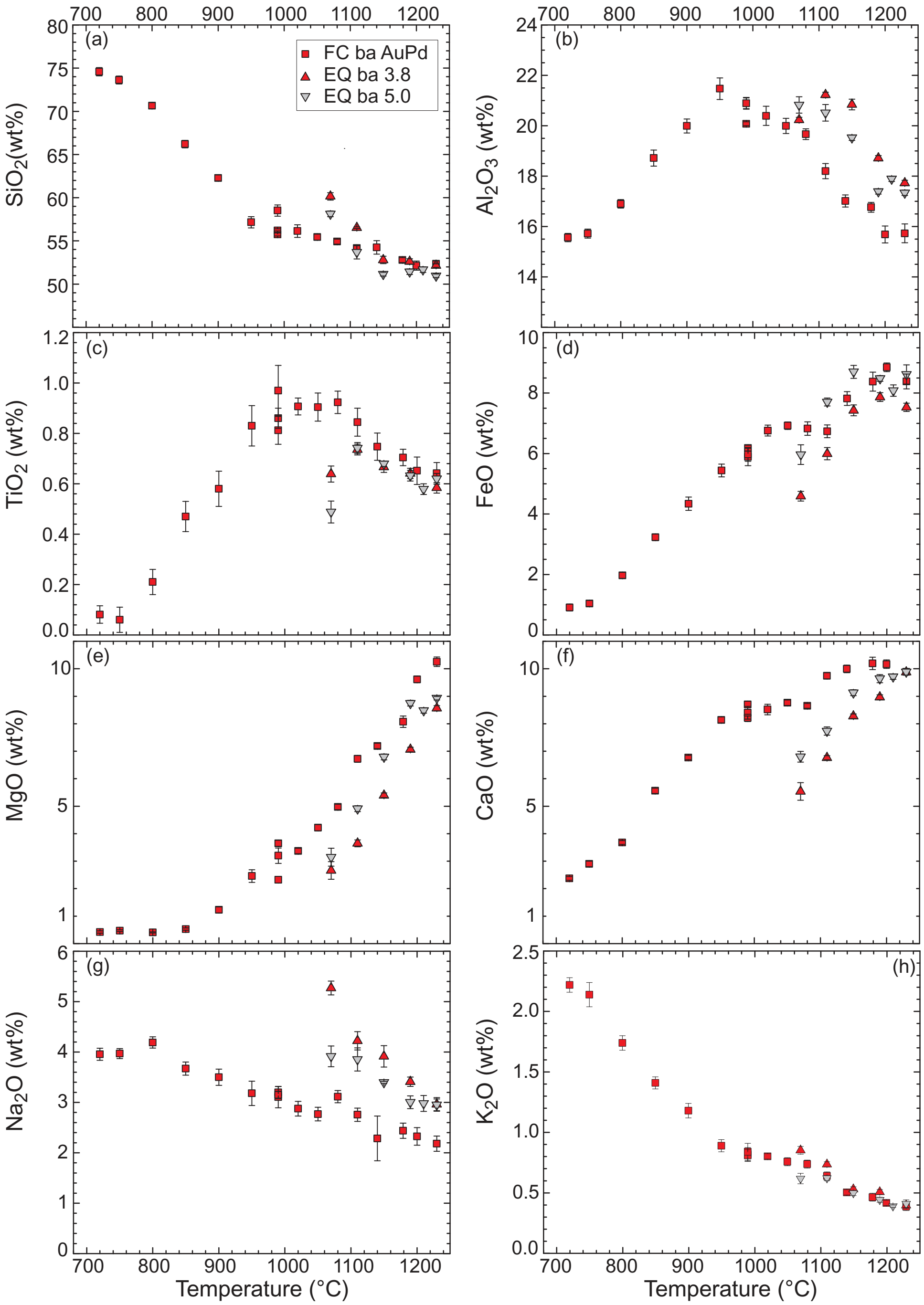

Fig. 10. Oxide variations of experimental liquids (glasses) as a function of temperature (°C) for the high-Mg basaltic andesite fractional series (85-44) under oxidizing conditions: (a) SiO_2; (b) Al_2O_3; (c) TiO_2; (d) FeO_{tot}; (e) MgO; (f) CaO; (g) Na_2O; (h) K_2O; all in wt % normalized to 100 wt % anhydrous. Compositions of equilibrium crystallization experiments at 1·2 GPa for 3·8 and 5·0 wt % H_2O [EQ ba 3.8 and EQ ba 5.0) are given for comparison and are taken from Müntener *et al.* (2001)]. Legend as in Fig. 8; error bars correspond to standard deviations of multiple analyses (Tables 3 and 4).

calc-alkaline around 55 wt % SiO_2 at 0·7 GPa and experiments that cluster around the dividing line at 0·9 GPa at 62 wt % SiO_2 was shown by Blatter *et al.* (2013).

Liquid evolution of basaltic andesite (85-44) experiments

The silica content steadily increases with decreasing temperature for fractional crystallization experiments, becoming steeper below 1000°C (Fig. 10a) where low-silica amphibole and garnet plus relatively anorthitic plagioclase replace opx and cpx at about 56·5 wt % SiO_2. Between 950 and 720°C silica continuously increases to 75 wt %, covering the entire range from andesite through dacite and rhyodacite to rhyolite. The two equilibrium crystallization series at 1·2 GPa (Müntener *et al.*, 2001) evolve in an identical fashion

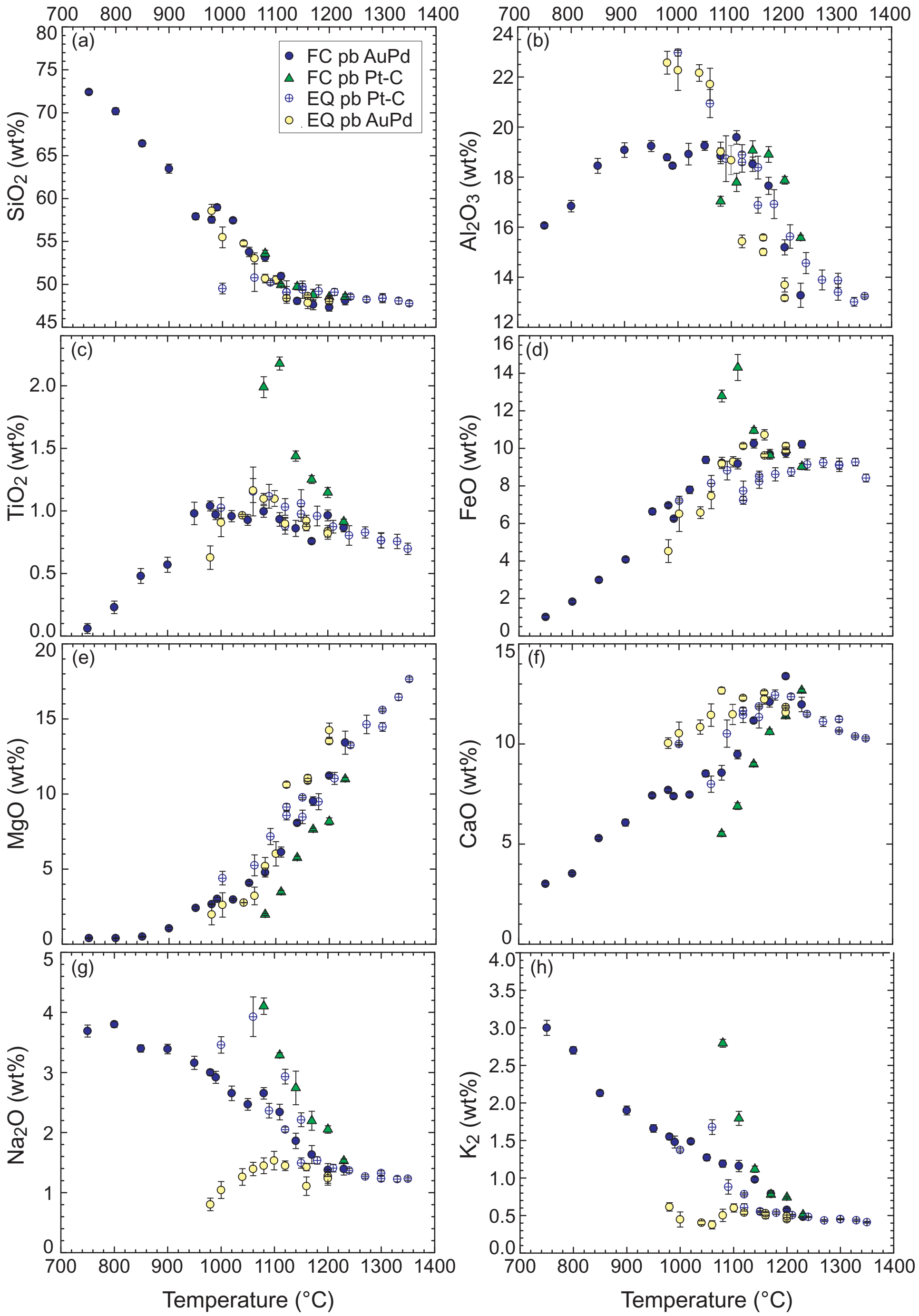

Fig. 11. Oxide variations of experimental liquids (glasses) as a function of temperature (°C) for the high-Mg basalt (RC158c) experiments: (a) SiO_2; (b) Al_2O_3; (c) TiO_2; (d) FeO_{tot}; (e) MgO; (f) CaO; (g) Na_2O; (h) K_2O; all in wt % normalized to 100 wt % anhydrous. Legend as in Fig. 8; error bars correspond to standard deviations of multiple analyses (Tables 3 and 4).

until about 1100°C but then silica strongly increases owing to earlier (1070°C) amphibole saturation and considerably lower amount of liquid left at this stage (Fig. 8a, 48 versus 70 % liquid). Al_2O_3 increases with decreasing temperature with some evident shifts towards higher alumina contents compared with the fractional crystallization experiments (Fig. 10b). The fractional crystallization experiments reveal a sharp bend to lower alumina contents between 900 and 950°C clearly related to plagioclase and garnet saturation effectively depleting the derivative liquids in alumina. TiO_2 initially increases as it behaves incompatibly with decreasing temperature until amphibole saturates (EQ and FC) between 1070 and 1050°C (Fig. 10c). At lower temperatures TiO_2 decreases in the equilibrium crystallization experiments (extensive amphibole crystallization owing to peritectic reaction) but remains constant in the FC series until 950°C followed by a sharp decrease owing to the combined effects of amphibole and ilmenite fractionation. Total FeO (Fig. 10d) for the equilibrium crystallization runs is initially nearly constant and strongly decreases below 1150°C where either hercynitic spinel (up to 5 wt % H_2O) or Fe-rich garnet (3·8 wt %) effectively deplete FeO. In the fractional crystallization experiments, FeO decreases at the beginning owing to the dominance of Fe-rich opx (1200–1110°C), followed by a plateau (1110–1020°C) where cpx is the dominant phase, and then by a continuous decrease to 720°C controlled by amphibole, Fe-rich garnet and ilmenite/Ti-magnetite. MgO shows a continuous decrease with decreasing temperature that is more pronounced for the equilibrium crystallization experiments (Fig. 10e); the final rhyolitic melts for the FC experiments are nearly devoid of MgO ($<0·5$ wt %). A similar evolution is observed for CaO, which decreases for all but the first fractionation step (only opx on the liquidus) owing to persistent cpx and later amphibole and plagioclase crystallization (Fig. 10f). It is interesting to note that the andesite compositions obtained by fractional crystallization around 1000°C are CaO-rich (8 wt %) at low MgO (2·3–3·5 wt %) and moderate Mg# (0·42–0·51; Table 4). The evolution of Na_2O is characterized by continuously increasing contents for the equilibrium crystallization runs and a ‘hump’ in the evolution of the fractional crystallization experiment at the onset of amphibole crystallization (Fig. 10g); a slowing down of Na_2O enrichment is expected at that point (amphibole is pargasitic), but the decrease is most probably an experimental artifact related to Na_2O loss during analyses and incomplete compensation in the next starting material. In any case, the Na_2O enrichment is less pronounced than for the equilibrium runs. The final two experiments of the FC series show a slight decrease of Na_2O from about 4·2 to 3·8 wt % related to the formation of albite-rich plagioclase. K_2O behaves incompatibly over the entire course of differentiation (Fig. 10h); however, in amphibole-dominated experiments the increase is moderate owing to accommodation of some K_2O in the amphibole structure. Unlike Na_2O, K_2O also increases in the last fractionation steps owing to the absence of any K_2O-bearing phase such as biotite or K-feldspar, and reaches 2·22 wt % K_2O at 720°C starting from an initial K_2O content of 0·40 wt % (85-44; Table 1), which corresponds to a near-perfect incompatible behavior at a melt fraction just below 0·2 relative to the initial basaltic-andesite.

Liquid evolution of high-Mg basalt (RC158c) experiments

The SiO_2 content as a function of temperature for this series reveals two contrasting trends (Fig. 11a). The SiO_2 content for the oxidized experiments and to a lesser extent the fractional crystallization experiments under reducing conditions (FC Mb Pt–C) increases with decreasing temperature, although only after a prolonged plateau at around 48–50 wt % extending from the liquidus (>1300°C) down to 1120°C. At this point SiO_2 increases and the liquids differentiate towards andesite, dacites, rhyodacites and finally rhyolites for the fractional crystallization series under oxidized conditions (FC Mb AuPd). The equilibrium crystallization series under oxidized conditions produces andesite with 58·5 wt % SiO_2 at 980°C whereas the experiments under reduced conditions, both FC and EQ, generate liquids that are trachyandesitic with 54 wt % SiO_2 and trachybasaltic with 50 wt % SiO_2, respectively. The differentiation to alkaline liquids is related to both their rather silica-rich fractionating solid assemblages, dominated by opx + cpx in the EQ experiments and opx–cpx–plag in the FC experiments, and very low melt fractions at the lowest temperatures responsible for the high alkali contents of these liquids. The strong and steady increase of SiO_2 in the oxidized FC experiments is related to the onset of spinel crystallization and reinforced by amphibole at and below 1050°C. Below 950°C a silica-poor solid assemblage composed of amph–plag–gar–ilm is responsible for the continuous and rapid increase of SiO_2. The EQ experiments under oxidized conditions show a progressive silica enrichment over the entire crystallization interval investigated owing to the expanded olivine-only stability field followed by cpx + spinel (Cr–Al–Fe^{3+}-spinels with decreasing Cr contents with decreasing temperature).

Al_2O_3 concentrations increase with decreasing temperature over the entire range for all the EQ experiments. Both EQ series (reduced and oxidized) reach elevated Al_2O_3 of nearly 23 wt % in andesitic liquids. The reduced FC experiments show a sharp bend in the Al_2O_3 evolution at 1140°C (19 wt %) where plagioclase plus hercynitic spinel saturate; the final trachyandesite that also experienced garnet extraction has 17 wt % Al_2O_3. The oxidized fractionation experiments show a plateau at the onset of garnet + plag crystallization (950–1000°C) followed by continuous decrease to lower temperatures with final rhyolites containing ~16 wt % Al_2O_3.

The TiO_2 contents initially increase with decreasing temperature for all series, and this increase slows down and/or inverts upon amphibole saturation between 1060 and 1040°C (Fig. 11c). The fractional crystallization experiment under reducing conditions shows a tholeiitic trend with increasing TiO_2 (low melt fraction under H_2O-poor conditions), except for the last run (1070°C) where ilmenite saturated. The oxidized fractionation experiments reveal strongly decreasing TiO_2 concentrations below 950°C, where Ti-bearing amphibole ilmenite and, in the last step, Ti-magnetite effectively deplete TiO_2 in the residual liquid.

The evolutionary trend for FeO_{tot} is initially nearly flat or even slightly increasing followed by a continuous decrease for all but the reduced fractionation experiments (Fig. 11d). The latter reveal a tholeiitic trend with strongly increasing FeO_{tot} until ilmenite and Fe-rich garnet saturate at 1080°C. Decreasing FeO_{tot} for all other series to lower temperatures is related to the extensive crystallization of increasingly more fayalitic olivine, hercynitic to magnetitic spinel, and, for the oxidized FC series, ilmenite and Fe-rich garnet.

MgO exhibits continuous decrease with decreasing temperature that is more accentuated for the fractional crystallization experiments under reducing conditions (Fig. 11e). The melts from the oxidized equilibrium crystallization experiments have initially higher MgO contents owing to their low crystallinity, but extensive olivine (and cpx) crystallization below 1120°C drives them to the same values as the other experiments.

CaO shows initial increase related to olivine (plus small amounts of Cr-rich spinel) crystallization as the liquidus phase, followed by a variable decrease for the different series (Fig. 11f): the oxidized fractional crystallization experiments show a steady decrease from 1200°C down to 750°C; the oxidized equilibrium crystallization experiments show a limited CaO decrease owing to the dominance of opx and amphibole at lower temperature resulting in considerably higher CaO contents in the coexisting solids at a given SiO_2 than in the fractional case. The reduced equilibrium experiments show a decrease similar to the oxidized equilibrium experiments, but that trend inverts in the last step, where CaO increased from about 8 to 10 wt % related to the peritectic reaction that consumes (high-Ca) cpx and generates amph + opx (see Fig. 7c). The resulting liquid is rich in CaO, but of trachybasaltic composition at rather low Mg# (0·52). The reduced fractionation experiments display steeply decreasing CaO contents with decreasing temperature owing to extensive cpx and plag fractionation.

The evolution of Na_2O and K_2O largely mimics the remaining melt fraction as they principally behave incompatibly (Fig. 11g and h), exceptions being the decrease of both Na and K in the last crystallization interval for the reduced equilibrium experiments where abundant amphibole accommodates alkalis, and likewise the behavior of both Na and K for the oxidized equilibrium crystallization experiments that reveal decreasing Na_2O and basically constant K_2O. At higher temperatures this reflects high melt fractions (>63% at 1080°C) but at the lowest melt fraction this is related to abundant crystallization of amphibole. As discussed below, melts are depleted in Na and also the mineral phases (amph and cpx) are unusually low in Na_2O, possibly indicating that abundant amphibole (>37%) in the last three experiments (980–1040°C) accommodates more alkalis than the coexisting liquids in this high-Mg basaltic system. Mass-balance constraints on these three experiments result in a perfect match for Na and K, except for the lowest temperature experiment (PU906, 980°C) where *c.* 0·20 wt % Na_2O is missing in the mass balance, pointing towards difficulties in measuring Na contents accurately in these highly hydrous (10 wt % H_2O) melts.

Mineral compositions

Olivine

Olivine exclusively occurred in the experiments with the high-Mg basalt starting material and the evolution of the forsterite content (fo) as a function of temperature is illustrated in Fig. 12. Olivine crystallized over nearly the entire temperature interval for the equilibrium crystallization experiments (1330–1060°C for reducing and 1200–1000°C for oxidizing conditions), but only formed a near-liquidus phase in the fractional crystallization experiments. Olivine compositions under oxidizing conditions are more forsteritic owing to the higher ferric iron content and, thus, relatively more magnesian character of the liquids (Fig. 4). The second consistent observation is that the fractional crystallization runs show a much steeper decrease of forsterite with temperature, favoring Mg extraction over Fe by olivine (e.g. Bowen & Schairer, 1935). The most magnesian olivine under oxidizing conditions is Fo 92·0, whereas under reducing conditions it is Fo 90·6, bracketing the compositions of the cores of the natural phenocrysts of the high-Mg basalt (Fo 91·1, Ulmer, 1986; Hürlimann *et al*., 2016) that is perfectly matched by the highest Fo content observed for the oxidized (NNO) fractional crystallization experiments (rk47, 1230°C, Fo 91·1). The Ca content of olivine is relatively low and varies between 0·21 and 0·34 wt % CaO with a clear tendency for higher values for the experiments conducted under more reducing conditions.

High-Ca clinopyroxene

Clinopyroxene crystallized over a wider temperature range (1200–950°C) and displays large compositional variation, as illustrated in Fig. 13. Tetrahedrally coordinated Al (Al^{IV}) varies negatively with $Mg + Fe^{2+}$ (Fig. 13a) close to, but with a flatter slope compared to the slope resulting from an ideal Tschermak's substitution [$(Mg, Fe^{2+})Si \Longleftrightarrow Al^{IV}Al^{VI}$], with the exception of three cpx from the most differentiated reduced fractional crystallization experiments. The most likely reason for the deviation from ideal Tschermak's substitution is the more pronounced Ca–Mg exchange (opx component) of these Fe-rich pyroxenes, which results in a horizontal line as depicted in the Ca–temperature diagram (Fig. 13b). Cpx shows restricted Ca variation as a function of temperature. There are notable exceptions such as the behavior of cpx from the basaltic andesite fractional experiments (FC ba AuPd), which show a constant increase of the Ca content. This is controlled by the following factors. (1) Cpx in the range 1170–1080°C is opx-buffered and its Mg# is nearly constant at 0·860 ± 0·005. Therefore, we attribute the increase in Ca content to the widening of the cpx–opx solvus with decreasing temperature at nearly constant Mg# (e.g. Lindsley, 1983). (2) Below 1080°C opx no longer coexists, and coexisting liquids of this series in the range 1080–900°C are rather Ca-rich. The equivalent experiments on the high-Mg basalt starting material (FC Mb AuPd) that are also opx-free below 1080°C do not show this increase of Ca in cpx but instead reveal a subtle decrease, most probably an expression of slightly higher silica activity in the liquid and considerably lower x_{Mg} favoring lower Ca contents at a given

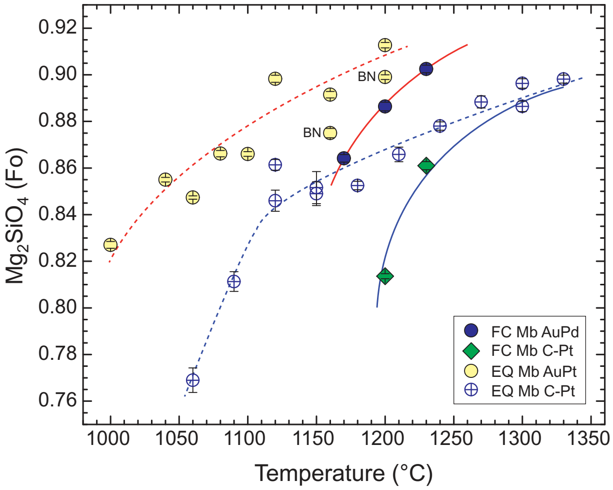

Fig. 12. Forsterite content (molar) of olivine from the high-Mg basalt (RC158c) experiments as a function of temperature (°C). Experiments labelled 'BN' were conducted with BN as spacers surrounding the AuPd–Pt capsules, resulting in slightly more reducing conditions. Legend as in Fig. 8; error bars correspond to standard deviations of multiple analyses (Tables 3 and 4).

temperature. The reduced fractional crystallization experiments (FC Mb Pt–C) reveal strongly decreasing Ca with decreasing x_{Mg} and temperature consistent with coexisting opx except for the lowest temperature experiment. The strong decrease of Ca with decreasing x_{Mg} and temperature buffered by opx (solvus) is well known (Lindsley, 1983). Titanium in cpx is characterized by an initial increase followed by a decrease related to either ilmenite or amphibole saturation that depletes the TiO_2 content in the coexisting liquid phase (Fig. 13c). In contrast, Ti in cpx continuously increases in the basaltic andesite down to the lowest temperatures. The Ti increase in cpx correlates with the highest Al_2O_3 and increasing Ca contents (Fig. 13b), both pointing towards decreased silica activity in hydrous, calc-alkaline magmas as already pointed out by Müntener *et al.* (2001). Sodium shows increasing concentrations with decreasing temperature, except for the equilibrium crystallization series on the high-Mg basalt starting material under oxidized conditions, which reveals continuous decrease (EQ Mb AuPd) over the entire temperature range (Fig. 13d). This is consistent with the low

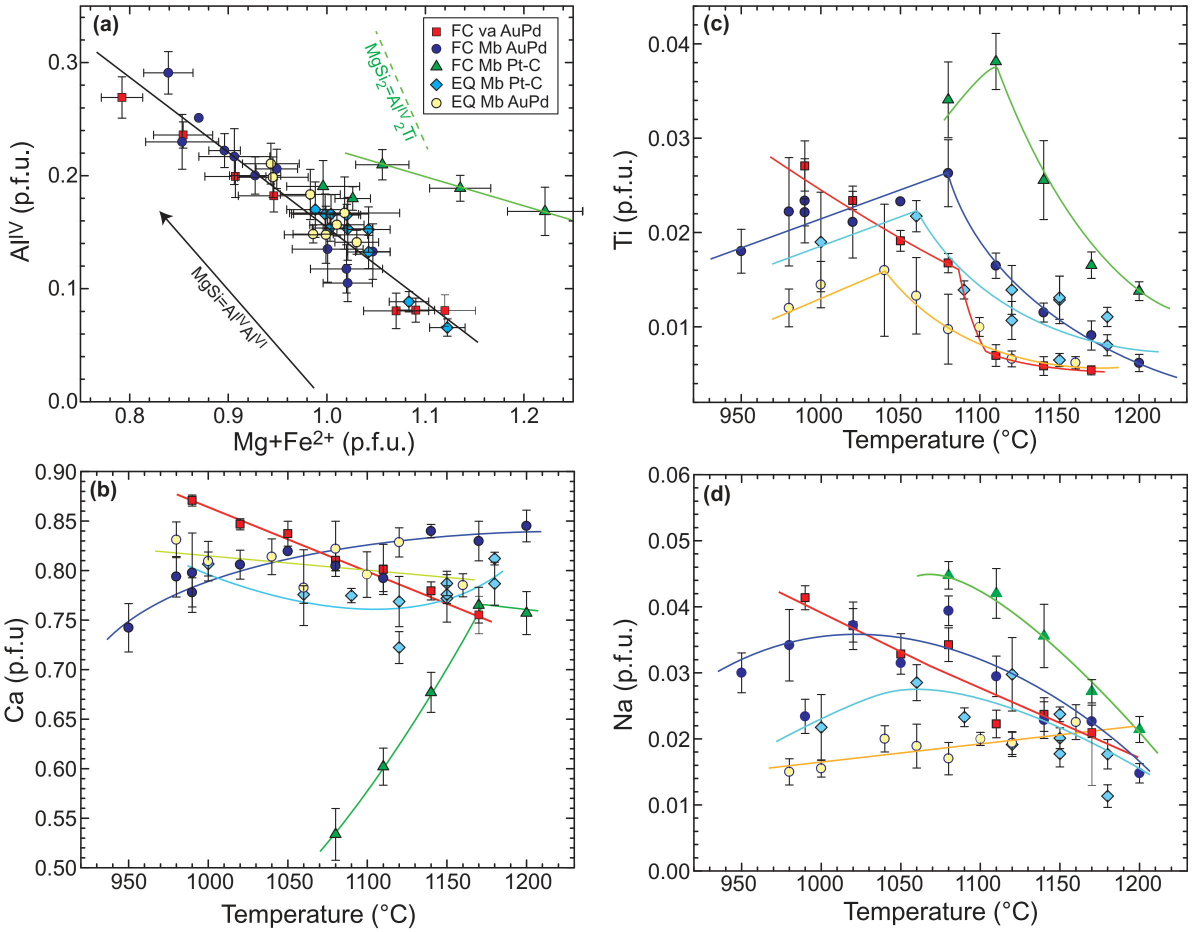

Fig. 13. Cpx compositional variations expressed as cations per formula units (p.f.u.) based on four cations and 12 positive charges. (a) Tetrahedrally coordinated Al (Al^{IV}) as a function of the sum of $Mg+Fe^{2+}$; labelled lines indicate Tschermak's and Ti-Tschermak's substitution respectively; (b) Ca as a function of temperature (°C); (c) Ti as a function of temperature; (d) Na as a function of temperature. Legend as in Fig. 8; error bars correspond to standard deviations of multiple analyses (Tables 3 and 4).

Na contents of these liquids (Fig. 11g). Both the FC and EQ experiments on the high-Mg basalt show decreasing Na contents in cpx with decreasing temperature when coexisting with amph. In contrast, the FC series on the basaltic andesite exhibits a continuous increase of Na with decreasing temperature, again pointing to lower silica activity and incorporation of Ti as NaTiAl^{IV} component.

Orthopyroxene

Orthopyroxene (opx) forms the liquidus phase in the basaltic andesite experiments, where it persists down to 1070°C. In the fractional crystallization experiments opx disappears at 1050°C in a peritectic reaction forming amphibole. In the oxidized equilibrium experiments (EQ Mb AuPd) opx appears only at 1040°C and persists to the lowest temperatures (980°C). Compositional variations of opx are illustrated in Fig. 14. Tetrahedrally coordinated Al reveals correlation along a 1:1 vector with $Mg + Fe^{2+}$ identifying the Tschermak's substitution as the principal mechanism for Al incorporation (Fig. 14a). The variation of Mg# (expressed as x_{Mg}) as a function of temperature shows a more pronounced decrease of the Mg# with decreasing temperature for fractional than for equilibrium crystallization experiments (Fig. 14b). The behavior of Ca as a function of temperature exhibits different behavior in the different experimental series (Fig. 14c), as follows. (1) The Ca content of the fractional experiments on the basaltic andesite shows an initial increase of Ca with decreasing temperature followed by a decrease as soon as cpx joins opx in the fractionating assemblage. (2) The reduced equilibrium crystallization experiments exhibit decreasing Ca with decreasing temperature as expected for opx–cpx equilibrium and evolve along the solvus to lower Ca contents with decreasing temperature. (3) The oxidized equilibrium crystallization experiments show invariant behavior of Ca with decreasing temperature that is consistent with constant to increasing Mg# related to progressive oxidation with decreasing temperature. (4) Opx crystallization in the reduced fractionation experiments results in increasing Ca with decreasing temperature despite the fact that it is cpx-saturated. This is the effect of a strongly increasing ferrosilite ($Fe_2Si_2O_6$) component expanding the pyroxene solvus on the low-Ca side to higher Ca contents (e.g. Davidson & Lindsley, 1985). Titanium incorporation into opx (Fig. 14d) shows a coherent evolution, increasing with decreasing temperature for all series correlating with liquid TiO_2 contents. Excluding sector zoned opx the partitioning of TiO_2 between opx and melt (K_d TiO_2^{opx}/TiO_2^{liq}) is 0·35 ± 0·04.

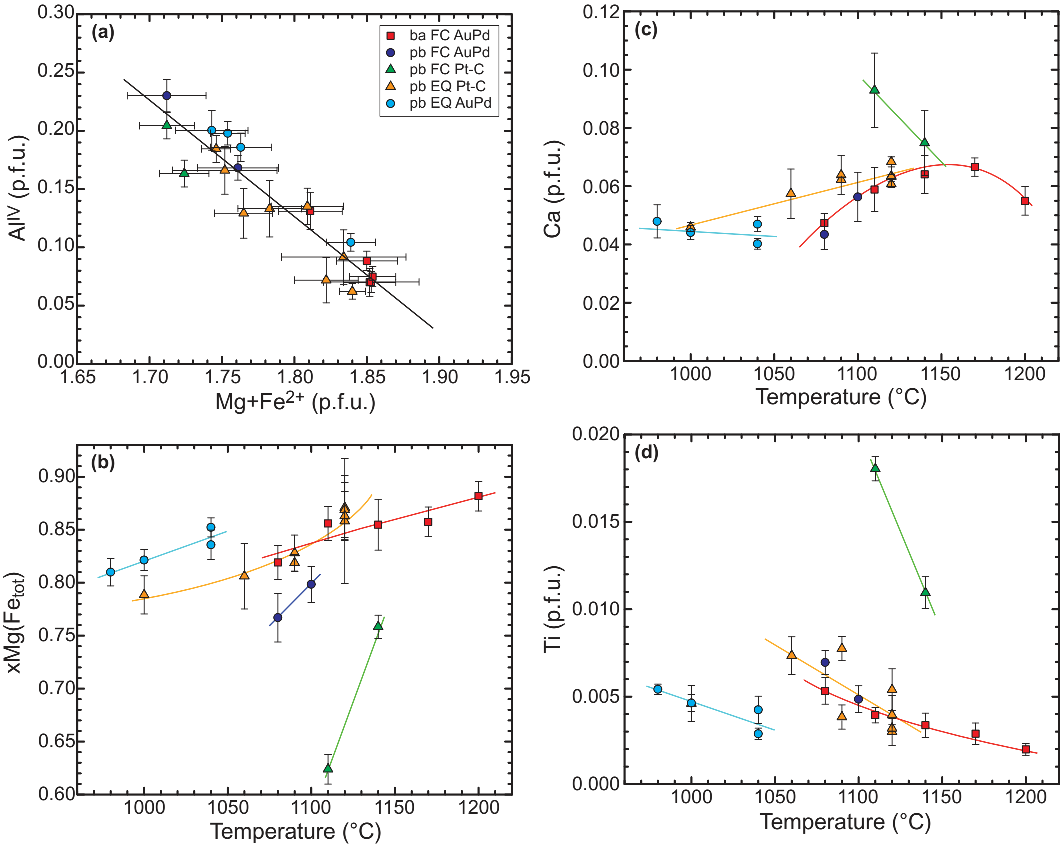

Fig. 14. Opx compositional variations expressed as cations per formula units (p.f.u.) based on four cations and 12 positive charges. (a) Tetrahedrally coordinated Al (Al^{IV}) as a function of the sum of $Mg + Fe^{2+}$; (b) $x_{Mg}(Fe_{tot})$ [$=Mg/(Mg + Fe^{2+} + Fe^{3+})$], (c) Ca and (d) Ti as a function of temperature (°C). Legend as in Fig. 8; error bars correspond to standard deviations of multiple analyses (Tables 3 and 4).

Amphibole

Amphibole crystallized over the temperature range (1060–720°C) delimited by the upper thermal stability of amphibole for basaltic to andesitic liquid compositions at 1·0 GPa (Eggler, 1972; Holloway & Burnham, 1972; Allen & Boettcher, 1978). Equilibrium crystallization experiments were restricted to just under 1000°C and show only limited compositional variations. Amphibole compositions from fractional crystallization experiments reveal systematic changes as a function of temperature, starting composition, mode of differentiation and fO_2 conditions. Amphibole at high temperature (>900°C) is pargasite or ferroan pargasites (Leake *et al.*, 1997) that change to tschermakite (900°C), tschermakitic hornblende (800°C) and finally magnesio-hornblende (720°C). Al^{IV} decreases for the equilibrium crystallization experiments (Fig. 15a), although with an offset between the two series, the oxidized ones plotting at higher Al^{IV} reflecting increased ferri-Tschermak's substitution ($Fe^{3+}Al^{IV} \Longleftrightarrow MgSi$). The fractional crystallization experiments reveal initial invariant (Mb series) or even increasing (ba series) Al^{IV} that inverts to monotonous decrease below 900°C. The latter behavior is expected as Al^{IV} is sensitive to temperature at constant pressure in buffered systems through the edenite exchange ($NaAl^{IV} \Longleftrightarrow \square Si$, Blundy & Holland, 1990; Holland & Blundy, 1994).

The Ti content of amphibole (Fig. 15b) shows very similar behavior to Al^{IV}: decrease at high temperature for the equilibrium series and initial increase followed by monotonous decrease below 950°C for the fractional series, clearly pointing towards Ti-Tschermak's substitution ($TiAl_2^{IV} \Longleftrightarrow MgSi_2$) and most probably decreasing TiO_2 content of the coexisting liquid and increasing D_{Ti}(amph/liq) with decreasing temperature (e.g. Nandedkar *et al.*, 2016).

The decrease of total alkali content on the A-site with decreasing temperature reflects decreasing edenite component with decreasing temperature (Fig. 15c). For experiments with coexisting plagioclase the edenite–richterite temperatures calculated by the equations of Holland & Blundy (1994) result in excellent agreement with the experimental temperatures within 25°C. Na(M4) increases with decreasing temperatures for the fractional crystallization experiments under oxidized conditions (Fig. 15d), whereas the equilibrium crystallization experiments plot at low Na(M4) without significant variation with decreasing temperature. The increase of Na(M4) with deceasing temperature is due to the $CaAl^{VI} \Longleftrightarrow Na(M4)Si$ ('plagioclase') substitution as Ca decreases with decreasing temperature.

The total Na content of amphibole is rather constant and does not show any significant variation for the fractional crystallization experiments (0·65 ± 0·05 a.p.f.u). The oxidized equilibrium crystallization experiments show lower (0·6–0·45 a.p.f.u.) total Na contents that decrease with decreasing temperature, consistent with low Na_2O contents of the coexisting liquids (1·2–1·5 wt %) challenging the commonly accepted view that amphibole saturates in calc-alkaline magmas at liquid Na_2O contents ≥3 wt % (Cawthorn & O'Hara, 1976). Ferric iron probably stabilizes amphibole at low Na content.

Oxide phases

Different spinel group minerals are present throughout most of the experiments, and their compositional variation is illustrated in Fig. 16. Ilmenite was stable in the last fractionation step (1080°C) in the reduced (Pt–C) fractionation series and between 900 and 800°C in the oxidized fractional crystallization experiments. Equilibrium crystallization experiments starting with the natural high-Mg basalt saturated with a Cr-rich to Cr-poor spinel phase over a large temperature interval, 1210–1000°C under reducing conditions and 1200–980°C under oxidizing conditions. The fractional crystallization experiments had no Cr and no spinel phase crystallized at high temperature. In the Mb-series fractional crystallization experiments, the first spinel phase was hercynitic spinel at 1170°C that persisted to 1110°C, followed by Ti-bearing magnetite at 1080°C that became replaced by ilmenite at 900°C that in turn was replaced by Ti-rich magnetite in the lowest temperature experiment at 750°C. In the basaltic andesite series, Ti-bearing magnetite first formed at 990°C and is replaced by ilmenite at 900°C and in turn by Ti-rich magnetite at 720–750°C. Zoning of Cr-rich spinel in the equilibrium crystallization experiments is mostly due to the presence of low-MgO seeds (orange star in Fig. 16) from the natural high-Mg basaltic starting material. Spinel shows rapid re-equilibration of Fe^{2+}–Mg but seems rather reluctant to exchange its Cr versus Al and/or Fe^{3+}, resulting in strongly zoned crystals. The variation of y_{Al} [$= Al/(Al + Cr + Fe^{3+})$] as a function of temperature (Fig. 16a) denotes various spinel phases observed in the experiments. Spinel in the reduced equilibrium crystallization experiments evolves from Cr-rich, Fe^{3+}-poor to Al-rich, Cr-bearing hercynitic spinel and finally to Cr-poor hercynite (Fig. 16c and d). The equilibrium crystallization experiments under oxidized conditions produced a large variety of Cr-rich to Cr-poor, Al-, but also Fe^{3+}-rich spinels with y_{Fe} 0·15–0·66. The oxidized fractional crystallization experiments with the high-Mg basaltic starting composition produced moderate Fe^{3+} (0·07–0·12 y_{Fe}) aluminous spinel at high temperatures (1170–1110°C) and Ti–Al–Mg-bearing magnetite at lower temperatures (1080–990°C), as did the basaltic andesite at 990°C (PU1049, 990°C) and both series at 720–750°C. Cr-rich spinel is a common accessory phase in the equilibrium crystallization experiments, but it does not exert a significant control on the liquid line of descent (LLD) except for Cr. This is different for hercynitic spinel, which is abundant just prior to amphibole saturation (Tables 3 and 4) and is responsible for SiO_2 increase in the coexisting liquids. Similar relationships have been observed at 0·7 and 1·2 GPa (Müntener *et al.*, 2001; Nandedkar *et al.*, 2014), underlining the importance of spinel on the

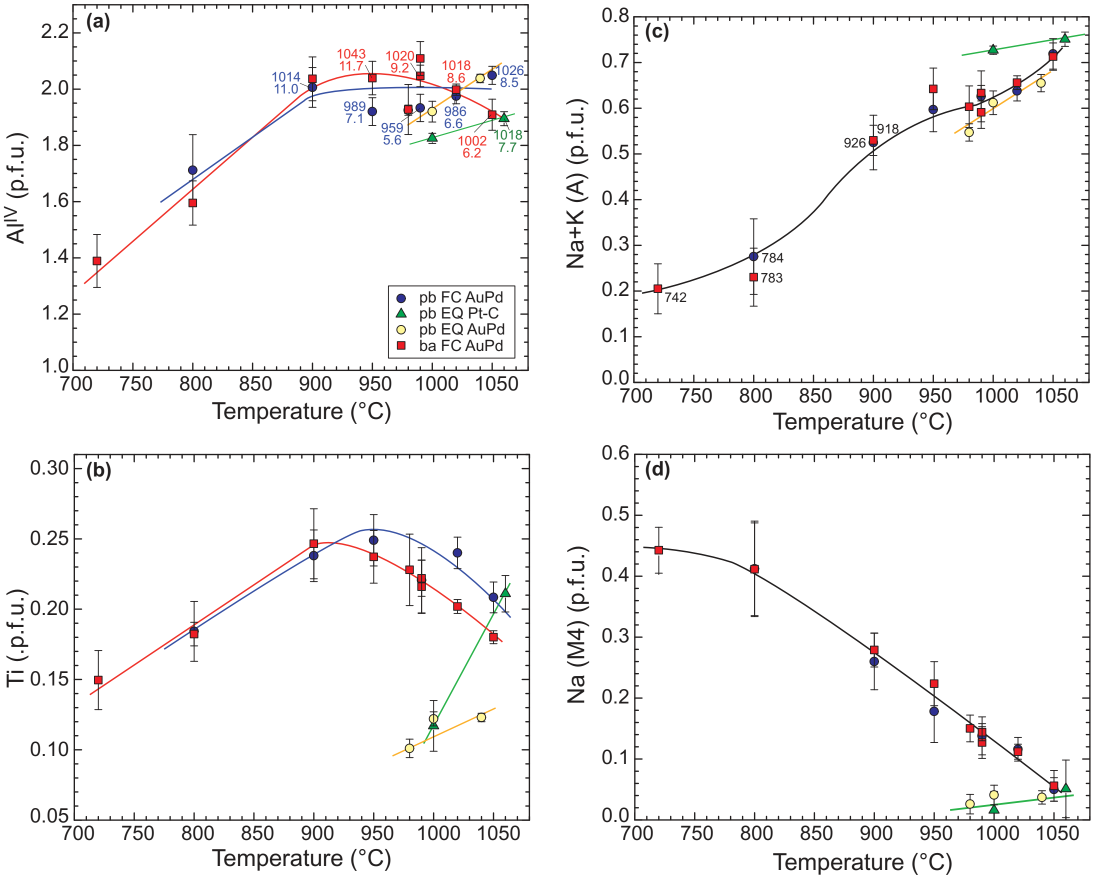

Fig. 15. Amphibole compositional variations expressed as cations per formula units (p.f.u.) based on 46 positive charges excluding OH, F, Cl and fixed Fe^{3+}/Fe_{tot} (see text for details) as a function of temperature. (a) Tetrahedrally coordinated Al (Al^{IV}); labels close to experiment indicate temperatures (°C) and pressures (GPa) calculated with the algorithms proposed by Ridolfi & Renzulli (2012); (b) Ti; (c) Na + K on A-site; labels close to experiments correspond to temperatures calculated with the plag–amph thermometer (edenite–richterite) according to Holland & Blundy (1994); (d) Na on M4-site. Legend as in Fig. 8; error bars correspond to standard deviations of multiple analyses (Tables 3 and 4).

differentiation path from basalt to andesite/dacite. The relative oxidation of the cubic oxide phases is related to fO_2. This is important for calc-alkaline systems where ilmenite is rarely coexisting with the cubic oxide phase, preventing the use of the Fe–Ti-oxide thermo-oxybarometer (Buddington & Lindsley, 1964; Lattard *et al.*, 2005). Ilmenite in the reduced fractional crystallization experiments contains very low recalculated ferric iron (5% hematite component) whereas ilmenite in the oxidized fractional crystallization experiments (800–900°C, ba and Mb series) contains a higher, but variable hematite component of 15–35 mol %.

Feldspar

Plagioclase was observed in the low-H_2O reduced fractional crystallization experiments (FC Mb Pt–C) at temperatures below 1170°C and in the oxidized fractional crystallization experiments below 950°C. Compositions in equilibrium with dacitic liquids are anorthite-rich (An78–84, 900–850°C) and change sharply to lower An contents (An45–55) at 800°C and 750°C coexisting with rhyodacitic to rhyolitic liquids; the plag at 720°C saturated with qtz, mag, amph ± garnet has an An content of 37. The partitioning of Ca/Na between plag and coexisting liquid (see Supplementary Data Electronic Appendix EA1; supplementary data are available for downloading at http://www.petrology.oxfordjournals.org) expressed as distribution coefficient $D(Ca/Na_{plag})/(Ca/Na_{liq})$ decreases from about four to two for the oxidized experiments despite high and increasing H_2O contents towards low temperatures; that is, it is not simply a function of H_2O content or f_{H2O} in the system but is, additionally, strongly composition dependent as discussed by Waters & Lange (2015).

Garnet

Garnet was observed in the lowest temperature reducing experiment in the low-H_2O fractional crystallization experiments (FC Mb Pt–C) coexisting with cpx, plagioclase, ilmenite and liquid (glass) and the oxidized FC experiments at temperatures of 950 down to 750°C. All garnets are relatively almandine-rich with >37% almandine component (for details, see Supplementary Data Electronic Appendix EA2). Garnet from the oxidized FC series shows consistent evolutionary trends with increasing almandine (Fe^{2+}, 37–60) and grossular

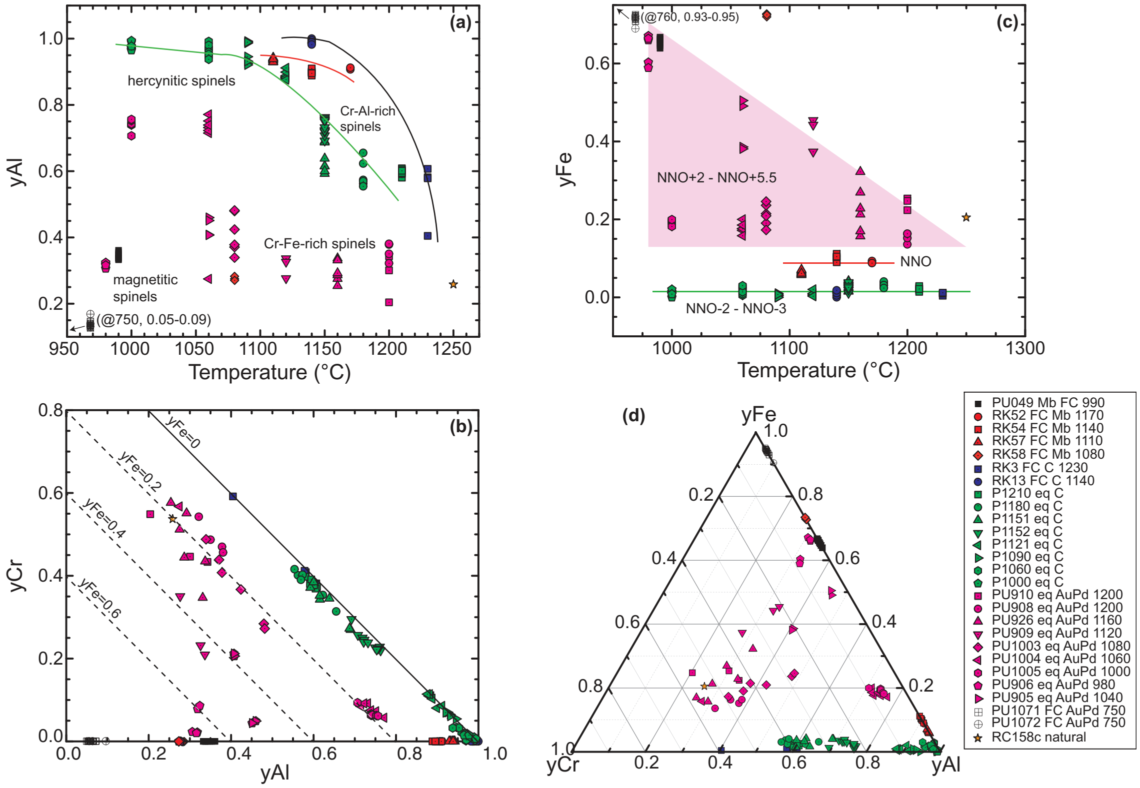

Fig. 16. Spinel phase (cubic oxide) compositional variations expressed as *x*- and *y*-parameters based on cations per formula units (p.f.u., three cations, eight positive charges). Individual spinel analyses are plotted because of large within-sample variations for some spinel phases (see text). (a) y_{Al} [$=Al/(Al+Cr+Fe^{3+})$] as a function of experimental temperature (°C); labels within the diagram identify various types of spinels; low-temperature magnetite spinels plot outside the compositional and temperature space of the diagram and are indicated by an arrow. (b) y_{Cr} [$=Cr/(Al+Cr+Fe^{3+})$] as a function of y_{Al}; dashed lines indicate corresponding y_{Fe3+} values; (c) y_{Fe} [$=Fe^{3+}/(Al+Cr+Fe^{3+})$] as a function of temperature; (d) ternary y_{Al}–y_{Fe}–y_{Cr} diagram summarizing spinel phase compositional variations. Legend identifies spinels from single experiments (Tables 2, 3 and 4).

(Ca, 20–28) components and decreasing pyrope (Mg, 40–13) contents with decreasing temperature, except in the last step where pyrope is constant and almandine increases at the expense of grossular. The spessartine content (Mn) varies between 2·7 and 5·5% without any discernible correlation with temperature. The Ti content initially increases from 950 to 900°C followed by continuous decrease to lower temperature; the bend coincides with ilmenite saturation and, thus, strong and continuous depletion of TiO_2 in the liquid indicating that Ti concentrations in garnet are controlled by partitioning between liquid and garnet. The total amount of garnet extracted between 950 and 720°C amounts to about 6·6 and 4·5 wt % relative to the initial starting material RC158c and 85-44 respectively; when normalized to andesite at 1000°C the amounts become nearly equal around 11% garnet fractionated between andesite and rhyolite. This mass fraction is likely to influence the trace element composition (rare earth elements, Sc, Y) of derivative liquids in the lower crust. The enhanced thermal stability of garnet in the reduced, low-H_2O fractionation experiments is consistent with the results of Alonso-Perez *et al.* (2009) and Müntener *et al.* (2001), which both showed that lower amounts of H_2O in the system increases the stability of garnet in andesitic liquids at pressures around 1·0–1·2 GPa.

DISCUSSION

Auto-oxidation of hydrous magmas during differentiation

In this experimental study, oxygen fugacity conditions of experiments conducted in AuPd capsules were computed from the amount of ferric iron in the liquid phase that was estimated from the difference in the measured Fe_{tot}–Mg olivine–liquid partitioning coefficients and the nominal value of 0·324 at 1·0 GPa assuming all Fe is Fe^{2+} (Ulmer, 1989). The calculations were performed through Monte Carlo type simulations taking into account the analytical uncertainty of the olivine and liquid compositions. The fO_2 values were obtained using the algorithm of Kress & Carmichael (1991) relating ferric iron content of the liquid to liquid composition, temperature and pressure conditions [Table 2; for details of the method see Kägi *et al.* (2005)]. The results illustrating the fO_2 conditions as a function of temperature for the experiments in AuPd capsules that contained olivine are shown in Fig. 17a. The fractional crystallization experiments on the high-Mg basalt indicate fO_2

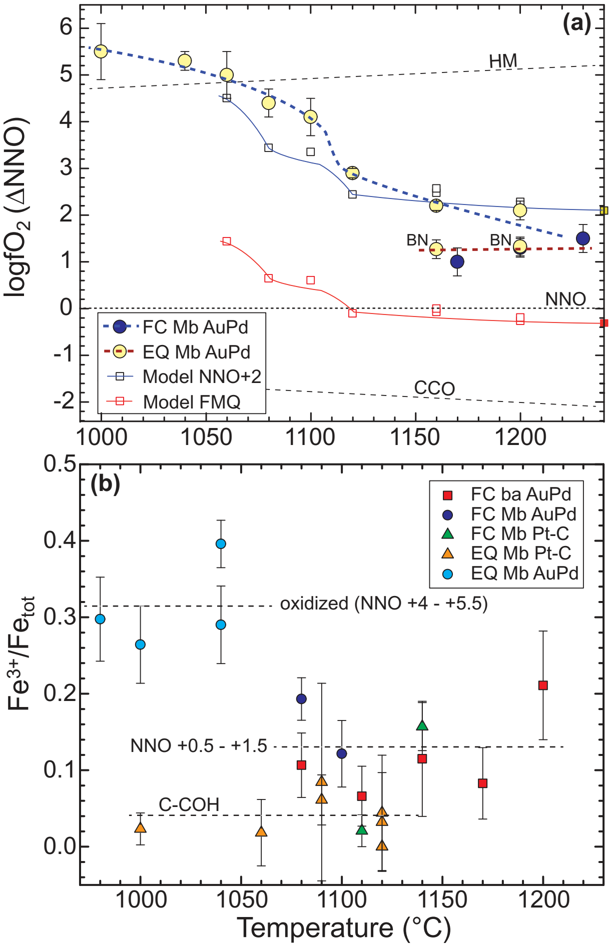

Fig. 17. (a) log fO_2 (ΔNNO) vs temperature diagram illustrating the evolution of fractional and equilibrium crystallization experiments under oxidizing conditions. Oxygen fugacity conditions were calculated based on the apparent olivine–liquid Fe–Mg distribution coefficients (Fig. 4, Table 2) assuming all Fe in olivine is ferrous and using the algorithm of Kress & Carmichael (1991) to relate computed Fe^{3+} contents of the liquid to fO_2. Data points labelled BN were conducted with BN surrounding the noble metal capsules. The data points and curves labelled Model NNO + 2 and Model FMQ are the results of model calculations using modal proportions (Table 2) and compositions of minerals (Tables 3 and 4) to compute Fe_2O_3 and FeO in coexisting liquids that are converted to fO_2 with the algorithm of Kress & Carmichael (1991). (b) Calculated ferric/total iron ratios of experimental opx based on cation normalization (four cations, 12 positive charges) as a function of temperature for various experiments under oxidizing (AuPd) and reducing (Pt–C) conditions.

conditions around NNO + 1, slightly higher than the targeted fO_2 range. The behavior of the closed-system equilibrium experiments is distinctly different. The starting value around NNO + 2 corresponds to the ferric/ferrous iron ratio of the natural starting material (RC158c, Table 1). At temperatures below 1150°C, fO_2 increases up to NNO + 5·5 (i.e. just above the hematite–magnetite equilibrium) at 1000°C where the remaining melt fraction is ~20%. It has been inferred that mantle-derived, primary arc magmas are not necessarily more oxidized than, for example, mid-ocean ridge magmas, but that more evolved andesitic to dacitic liquids acquire their higher fO_2 by differentiation of minerals with low ferric iron content such as olivine and clinopyroxene (e.g. Lee *et al.*, 2005; Dauphas *et al.*, 2009; Jenner *et al.*, 2010). The more oxidized conditions are reflected in the abundant crystallization of magnetite and the increased ferric/ferrous iron ratio (e.g. Carmichael, 1991). Our data support this hypothesis. Using the modal proportions of phases determined by mass balance (Table 2) and solid phase compositions (Table 3) we obtained an excellent match of the Fe_2O_3 and FeO contents (5·95 and 3·00 wt %, respectively) of the liquid compared with the contents estimated by the Monte Carlo simulation, with a calculated difference of 0·09 in Fe_2O_3 and –0·17 for FeO relative to the starting high-Mg basalt [run PU1004 (1060°C, ol, cpx, sp, liq)]. This indicates that auto-oxidation driven by fractionation of low-Fe^{3+} ferromagnesian phases is a viable process to oxidize hydrous arc magmas. The principal reason that this is much more effective for hydrous arc magmas than for nearly dry tholeiitic magmas is probably a consequence of the expanded olivine stability field at a given pressure towards more differentiated compositions (e.g. Kushiro, 1972, 1975). The effect might be further amplified by the observation that amphibole coincides with decreased amounts of magnetite in arc-related ultramafic (hornblendite) to gabbroic (amphibole-gabbro) cumulates, suppressing the potential depletion of ferric iron that would be caused by magnetite crystallization. Two high-temperature (1200 and 1160°C, PU908 and PU899) equilibrium crystallization experiments behave slightly differently, plotting at lower fO_2; these experiments were conducted in BN-bearing piston cylinder assemblies, leading to more reducing conditions (e.g. Kägi *et al.*, 2005). The difference between reducing and oxidizing conditions in equilibrium crystallization experiments is also reflected in the cpx/amphibole ratios. Under reducing conditions (P1060, P1000) the cpx/amphibole ratio is high, whereas under oxidizing conditions (PU905, 906 and 1005) the cpx/amphibole ratio is low. Oxidizing conditions, therefore, favor the formation of hornblende-rich cumulates in the roots of island arc volcanoes. The 'auto-oxidation' is further recorded in the compositions of the coexisting solid phases: spinel from the oxidized equilibrium experiments displays increasingly higher y_{Fe} with decreasing temperature than spinel from the other experiments (Fig. 16c and d). Likewise, the calculated Fe^{3+}/Fe_{tot} ratio of opx exhibits a clear distinction between the reduced experiments (Pt–C), the fractional crystallization experiments around NNO (FC Mb and ba AuPd) and the oxidizing experiments (EQ Mb AuPd) (Fig. 17b). This diagram basically mimics Fig. 4 (olivine–liquid Fe–Mg K_d), further substantiating auto-oxidation as a possible process in fractionating magmatic systems.

To quantify the potential effect of extended olivine extraction from a primary liquid, we modeled the fO_2 evolution of the primary high-Mg basalt (RC158c) for two initial fO_2 conditions: (1) the measured NNO + 2 of the natural RC158c simulating oxidized equilibrium experiments; (2) FMQ approaching inferred 'pristine' MOR-like fO_2 conditions during partial melting (e.g. Ballhaus, 1993). The models considered the modal proportions and compositions of the EQ Mb AuPd series solid phases including the calculated Fe^{3+}/Fe_{tot} ratio for cpx, opx and spinel for the NNO + 2 starting model, and lower Fe^{3+}/Fe_{tot} ratios between the values obtained for the FC Mb AuPd and EQ Mb Pt–C series. The results are illustrated in Fig. 17a. The model can reconcile the observed fO_2–temperature evolution of the oxidized equilibrium crystallization experiments slightly displaced to lower fO_2 values. A similar evolution is shown for the model starting at FMQ (at 1280°C and 1·0 GPa = NNO – 0·31) evolving to NNO + 1·45 at 1060°C just before amphibole saturation. This corresponds to a closed-system oxidation of 1·8 log units, resulting in fO_2 values typical for arc magmas. Saturation in magnetite might buffer the further evolution of andesite to rhyolite to near constant fO_2 or even decrease it (e.g. Jenner *et al.*, 2010). A similar process to account for the elevated fO_2 conditions displayed by most arc magmas has been proposed by Lee *et al.* (2010) based on Zn/Fe systematics and is confirmed by the fO_2–temperature relationship observed in the oxidized equilibrium crystallization experiments when fO_2 was not buffered externally (as typically done in experimental studies), but was exclusively controlled by phase equilibria.

A comparison of the evolution of fO_2 along the LLD between fractional and equilibrium crystallization experiments is not possible; the fractional experiments have been forced to differentiate along the NNO buffer by resetting the ferric/ferrous ratio in every single step to the attempted NNO value, whereas the equilibrium crystallization experiments were allowed to evolve unconstrained (closed system) in T–fO_2 space resulting in strong (+3·5 log units) oxidation from basalt to andesite. Further experimental studies, in particular fractional crystallization studies not resetting the fO_2 in every step, should be conducted together with spectroscopic studies (Mössbauer, X-ray absorption spectroscopy (XAS)) to evaluate a possible oxidation during differentiation. Starting materials less oxidized than in the present case would clarify whether contrasting phase relations between tholeiitic (nearly dry) and calc-alkaline (more hydrous) magmas are responsible for different fO_2 conditions reported for the dominant intermediate magmas rather than different fO_2 conditions in their mantle sources moderated by absence or presence of slab-derived hydrous (oxidizing?) component as alternatively proposed (e.g. Parkinson & Arculus, 1999; Kelley & Cottrell, 2009).

Comparison of liquid compositions with previous experimental studies

The first part of the discussion presents a comparison of the experimentally derived liquid compositions of this study with those from previous studies on hydrous calc-alkaline and anhydrous (tholeiitic) differentiation at a pressure around 1·0 GPa. Experiments conducted with similar starting materials and comparable conditions include the equilibrium and fractional crystallization experiments on an anhydrous tholeiitic starting composition at 1·0 GPa (Villiger *et al.*, 2004), the equilibrium crystallization experiments on hydrous basaltic starting materials at 1·0 GPa (Foden & Green, 1992; Kawamoto, 1996; Pichavant & Macdonald, 2007) and 0·9 GPa (Blatter *et al.*, 2013), as well as the fractional crystallization study of Nandedkar *et al.* (2014) at 0·7 GPa.

To distinguish the tholeiitic from the calc-alkaline differentiation series we plotted FeO/MgO versus SiO_2 (Fig. 18a). Liquid compositions of this and most other studies straddle the calc-alkaline–tholeiitic discrimination line in the range basalt to andesite and, after excursion into the tholeiite field (fractional experiments on oxidized compositions from this study), end in the calc-alkaline field for rhyodacites and rhyolites. The notable exceptions are equilibrium and fractional crystallization experiments under anhydrous (Villiger *et al.*, 2004) and low-H_2O (FC Mb Pt–C series of this study) reducing conditions and some of the data obtained by Foden & Green (1992); only the differentiated liquids obtained by Kawamoto (1996) and Pichavant & Macdonald (2007) plot within the calc-alkaline field at intermediate compositions. The observation that most experimental studies on hydrous differentiation of basaltic magmas at elevated pressures and/or $fO_2 <$ NNO plot close to or even within the tholeiitic field has been discussed in detail by Sisson *et al.* (2005) and Blatter *et al.* (2013). This is also shown by the 0·7 and 1·0 GPa fractional crystallization experiments on the high-Mg basaltic starting material (Nandedkar *et al.*, 2014; this study FC Mb AuPd).

Figure 18b displays the TAS diagram (Le Maitre *et al.*, 1989) showing the respective names associated with the different liquid compositions. Most experimental studies, including 1·0 GPa anhydrous experiments (Villiger *et al.*, 2004), show an evolution from basalt to basaltic andesite and andesite or dacite. However, the equilibrium and fractional crystallization experiments under reducing conditions (EQ and FC Mb C + Pt) evolve to alkaline compositions through trachybasalts to basaltic trachyandesite. Overall, hydrous experiments under lower crustal conditions from this and previous studies reveal the typical calc-alkaline differentiation trends from basalt to dacite to (high-silica) rhyolite. Inspection of the K_2O–SiO_2 diagram (Fig. 18c) reveals the importance of (1) the starting material and (2) the fraction of liquid left for a given SiO_2. The anhydrous crystallization experiments (Villiger *et al.*, 2004) were conducted with a low-K olivine tholeiite and evolve to high K contents at 1060°C with only 3·5 wt % melt left relative to the start, amplifying the initial K_2O content of 0·08 wt % to over 2 wt %. The fractional experiments from this study and the equilibrium crystallization experiments from Müntener *et al.* (2001) employing the basaltic-andesite starting material initially straddle the low- to medium-K dividing line to andesites and then evolve towards medium-K dacites and rhyolites,

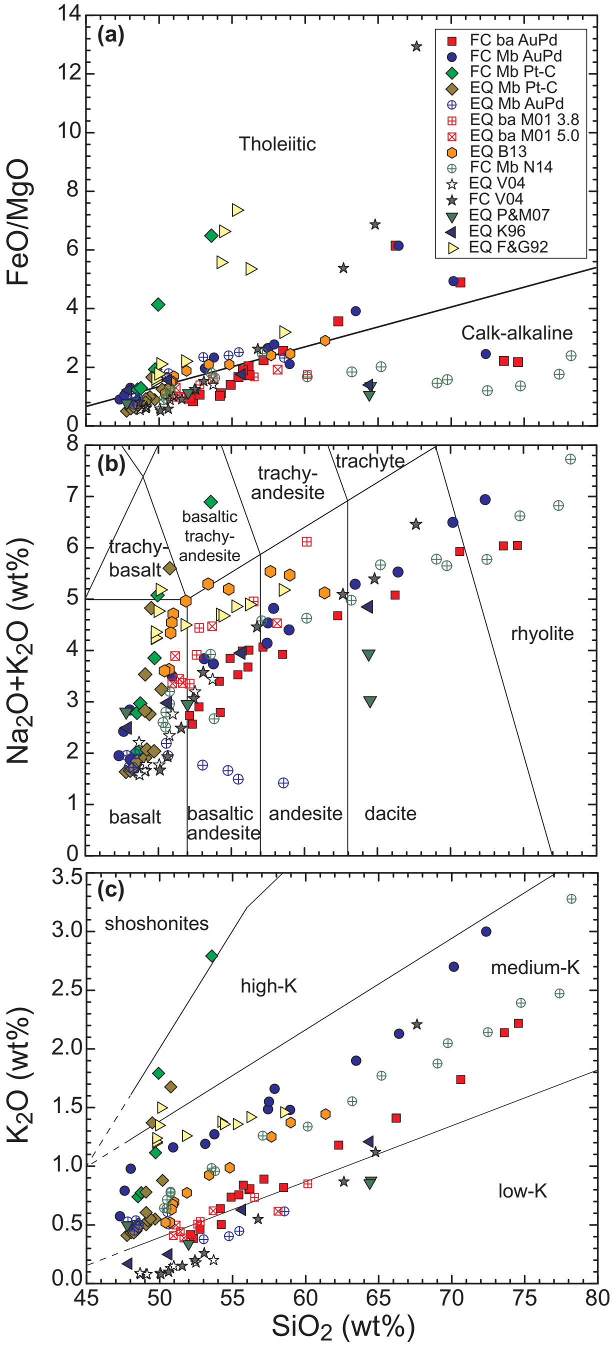

Fig. 18. Liquid compositions of this study compared with other experiments at similar conditions on comparable starting materials. (a) FeO_{tot}/MgO vs SiO_2 (wt %) diagram with the tholeiitic and calc-alkaline fields according to Miyashiro (1974); (b) TAS (total alkali vs silica, Le Maitre *et al.*, 1989) diagram used to denote compositions with volcanic rock names; (c) K_2O (wt %) vs silica diagram discriminating low-, medium-, high-K and shoshonitic rock series. Abbreviations for experiments from this study are as in Fig. 8, EQ ba M01 3.8 and 5.0 denote equilibrium crystallization experiments from Müntener *et al.* (2001) on basaltic andesite 85-44 with 3·8 and 5·0 wt % initial H_2O; EQ B13, Blatter *et al.* (2013); FC Mb N14, Nandedkar *et al.* (2014); EQ V04, Villiger *et al.* (2004) equilibrium crystallization experiments; FC V04, Villiger *et al.* (2004) fractional crystallization experiments; EQ P&M07, Pichavant & Macdonald (2007); EQ K96, Kawamoto (1996); EQ F&G92, Foden & Green (1992).

whereas the higher K oxidized fractional crystallization experiments starting from the high-Mg basalt plot within the medium-K field, approaching the high-K field with increasing differentiation. In contrast, the equilibrium crystallization experiments under oxidized conditions (EQ Mb AuPd) evolve towards low-K compositions owing to extensive amphibole crystallization effectively removing alkalis. The reduced fractional and equilibrium crystallization experiments evolve towards high-K and even shoshonitic compositions owing to extensive pyroxene crystallization and late or absent amphibole crystallization leaving as little as 14 wt % liquid left relative to the start. This observation is consistent with the proposal of Meen (1987), suggesting that (anhydrous) crystallization of ‘normal-K’ calc-alkaline basalts at the base of the crust can lead to high-K or shoshonitic intermediate derivative liquids under reducing conditions. Such an evolution probably requires low initial H_2O contents of 0·5–1·0 wt %.

Liquid compositions obtained by various experimental studies are illustrated in oxide variation diagrams (Fig. 19). It should be noted that most previous studies on hydrous systems were crystallization experiments on fixed bulk compositions (i.e. equilibrium crystallization experiments) and thus are not strictly comparable with the fractional crystallization experimental datasets (Villiger *et al.*, 2004; Nandedkar *et al.*, 2014; this study). This additionally explains that these studies cover a more restricted temperature and/or composition space as the amount of residual liquids becomes very small.

The highest liquidus temperatures (1330°C) observed are those of the high-Mg basalt under reducing conditions followed by the anhydrous tholeiitic system (1300°C) (Villiger *et al.*, 2004), which has lower liquidus temperature because its normative olivine (and MgO) content is lower. Most other compositions have liquidus temperatures around 1200–1250°C; Foden & Green (1992) and Kawamoto (1996) did not delimit the liquidus and did not crystallize olivine in their highest temperature runs, indicating that their starting compositions were either not (near) primary and/or their respective H_2O contents (5 and 1 wt %) were too low.

The Mg# as a function of temperature reveals a systematic decrease from 0·70–0·77 consistent with primary mantle derived magmas to below 0·4 for derivative andesitic or dacitic liquids, and a further decrease to ~0·2 for rhyodacites (Fig. 19a). This systematics inverts for the last steps towards rhyolites, consistently exhibiting Mg# of about 0·4 [the somewhat different behavior of the Nandedkar *et al.* (2014) fractional crystallization experiments is explained in their paper]. Exceptions are anhydrous and low-H_2O fractional crystallization experiments under reducing conditions (Villiger *et al.*, 2004; this study) that evolve to much lower Mg# at temperatures below 1150°C related to extensive pyroxene (and plagioclase) fractionation, and some of the lower temperature experiments of Foden & Green (1992) that crystallized amphibole and pyroxene but lack Fe–Ti-oxides. The latter experiments (containing 5 wt % H_2O) conducted in

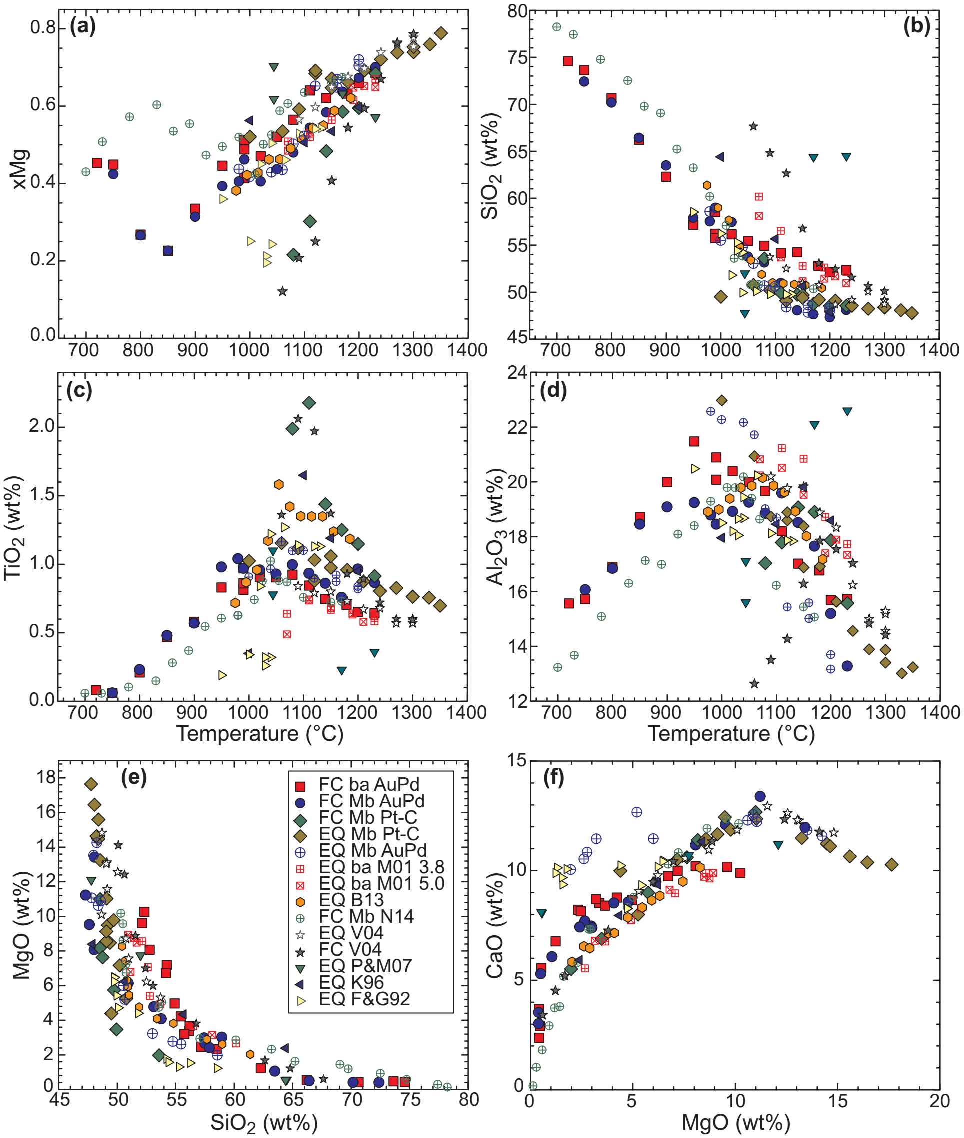

Fig. 19. Liquid compositions of this study compared with other experiments at similar conditions on comparable starting materials. (a) xMg [$=MgO/(FeO_{tot}+MgO)$ molar] versus temperature (°C) diagram; (b) SiO_2 (wt %) versus temperature; (c) TiO_2 (wt %) versus temperature; (d) Al_2O_3 (wt %) versus temperature; (e) MgO (wt %) versus SiO_2 (wt %); and (f) CaO (wt %) versus MgO (wt %). All symbols and abbreviations as in Figure 18.

AgPd sample containers enclosed in BN might have resulted in very low fO_2 conditions [for a discussion see Kägi *et al.* (2005)], thus resembling the experiments conducted under reduced conditions in this work.

The evolution of SiO_2 as a function of temperature displays a fan-shaped pattern between basaltic and andesitic compositions (Fig. 19b). The equilibrium and fractional crystallization experiments under oxidizing conditions start at different levels but converge at lower temperatures together with the equilibrium crystallization experiments at 0·9 GPa of Blatter *et al.* (2013), all leading to andesite or dacite compositions around 1000°C. The fractional series subsequently continue towards rhyolite and are virtually identical, indicating phase equilibria control towards the granite minimum. The fractional experiments at 0·7 GPa (Nandedkar *et al.*, 2014) evolve in parallel but are shifted to higher temperatures by about 50°C; that is, they are more silica-rich for a given temperature below 1000°C consistent with considerably higher An contents of fractionating plagioclase more efficiently enriching the liquid in silica. The compositions of Foden & Green (1992) and Kawamoto (1996) show a similar evolution, but with larger scatter. The equilibrium crystallization experiments of Müntener *et al.* (2001) and Pichavant & Macdonald (2007) at 1·2 and 1·0 GPa with lower H_2O contents evolve towards more silica-rich compositions at higher temperatures.

TiO_2 as a function of temperature displays a bell-shaped evolution for different experimental series dictated by (1) the initial TiO_2 content, (2) fO_2 conditions controlling Fe–Ti-oxide saturation, and (3) H_2O content influencing amphibole saturation. The higher fO_2 experiments on high-Mg basalt and basaltic andesite (this study) display slightly increasing TiO_2 until Fe–Ti-oxide and/or amphibole saturates around 1050°C, and thereafter TiO_2 monotonically decreases (Fig. 19c). The evolution is similar for the equilibrium crystallization experiments of Blatter *et al.* (2013), although shifted to higher TiO_2 values owing to their higher initial TiO_2. Anhydrous and low-H_2O experiments under reducing conditions evolve to higher TiO_2 contents owing the absence of amphibole and delayed Fe–Ti-oxide saturation.

Al_2O_3 reveals very contrasting behavior as a function of temperature dictated by the presence or absence of plagioclase and hercynitic spinel along the liquid line of descent. Fractional crystallization experiments under oxidized conditions at 1·0 GPa are characterized by an increase of Al_2O_3 to about 950°C and a continuous decrease thereafter, with the onset of plagioclase and garnet crystallization effectively depleting Al_2O_3 in the liquid. The 0·7 GPa experiments reach a maximum at 1040°C owing to earlier saturation in plagioclase with decreasing pressure. All equilibrium crystallization experiments (EQ Mb AuPd and Pt–C) do not saturate in plagioclase down to temperatures of 980–1000°C, thus Al_2O_3 increases with increasing differentiation. The Blatter *et al.* (2013) experiments crystallize plagioclase at 0·9 GPa at temperatures below 1095°C, consistent with their relatively low H_2O content (2 wt %) and slightly lower pressure. The evolution of liquid Al_2O_3 underlines the important role of H_2O controlling the relative stabilities of plagioclase and amphibole. At lower temperatures, investigated only in this study, garnet exerts a significant control on Al_2O_3 liquid concentration.

MgO as a function of SiO_2 displays a monotonic decrease principally controlled by the initial MgO and SiO_2 contents; only the low-H_2O experiments on calc-alkaline compositions (FC Mb Pt–C and Foden & Green, 1992) deviate somewhat from the general trend, plotting at lower MgO contents for a given SiO_2 consistent with their extensive and early crystallization of plagioclase limiting silica increase. CaO shows a consistent increase at high MgO controlled by olivine fractionation, followed by a decrease along a single trajectory for most studies controlled by cpx, amphibole and plagioclase crystallization (Fig. 19f). At the lowest temperatures both fractional series converge but show a displacement towards lower MgO for a given CaO content compared with the experiments of Blatter *et al.* (2013) and Nandedkar *et al.* (2014), which is most probably the effect of later plagioclase saturation and overall lower An contents. A significant displacement from the common evolution is shown by equilibrium crystallization of the high-Mg basalt, which is shifted towards higher CaO at lower MgO contents consistent with olivine (+ Cr-spinel) crystallization and delayed cpx saturation. A similar evolution is observed for some of the experiments of Foden & Green (1992) and Pichavant & Macdonald (2007). These experiments are characterized by large amounts of amphibole and very minor cpx. A large amount of dissolved H_2O in the liquid and/or high fO_2 may favor high abundances of amphibole that drive equilibrium crystallization to rather unusual compositions.

In summary, the fractionation experiments on primitive, hydrous magmas show similar evolutions at lower crustal conditions, generally differentiating to intermediate andesitic to dacitic derivative liquids around 1000°C. Major controls are exerted by the absolute (or relative) H_2O contents as well as fO_2, ultimately leading to a variety of LLDs. The most discriminant oxides are TiO_2, Al_2O_3 and CaO, which are mainly controlled by the phases olivine, cpx (opx), amphibole, plagioclase, garnet and Fe–Ti-oxide. Thus, to predict LLDs for a specific plutonic and/or volcanic suite requires information on the H_2O content of parental magmas, fO_2 conditions and pressure. This study and that of Nandedkar *et al.* (2014) provide additional constraints on the evolution from intermediate to SiO_2-rich compositions showing systematic differences as a function of pressure. The LLD at 1·0 GPa shows delayed plagioclase crystallization and occurrence of garnet and ilmenite, the latter being replaced by ulvöspinel–magnetite solid-solution at 0·7 GPa. Importantly, the LLDs for compositions from dacite to rhyolite completely converge for all elements, probably controlled by amphibole, as also shown for Mt St Helens magmas by Blatter *et al.* (2017). Potassium behaves nearly completely incompatibly down to the lowest temperatures investigated and is a key element to identify sources of arc magmas.

The metaluminous to peraluminous evolutionary trend of derivative liquids with increasing differentiation starting from hydrous calc-alkaline to arc-tholeiitic basaltic to basaltic andesite starting material is illustrated in Fig. 20. At 0·9–1·2 GPa, andesite and more evolved compositions (54–62 wt % SiO_2) all become peraluminous, confirming that peraluminous dacitic to rhyolitic liquids are not only the product of anatectic melting of alumina-rich (e.g. metapelitic) sources, but can also be derived from metaluminous basalts by differentiation at elevated pressures dominated by early cpx and amphibole (e.g. Cawthorn & O'Hara, 1976; Cawthorn *et al.*, 1976; Müntener *et al.*, 2001; Blatter *et al.*, 2013, 2017; Nandedkar *et al.*, 2014). Previous experimental studies used for comparison terminate before reaching the peraluminous field, but the trend towards peraluminous compositions is also clearly indicated. Distinctly different are experiments under reducing conditions that remain metaluminous irrespective of their H_2O contents—an expression of their more abundant opx crystallization driving them away from the metaluminous–peraluminous boundary—as well as the experiments by Foden & Green (1992) that exclusively crystallize amphibole and no pyroxenes.

Liquid lines of descent and phase relations in pseudo-ternary projections

Compositions of synthesized liquids for equilibrium and fractional crystallization experiments are plotted in a

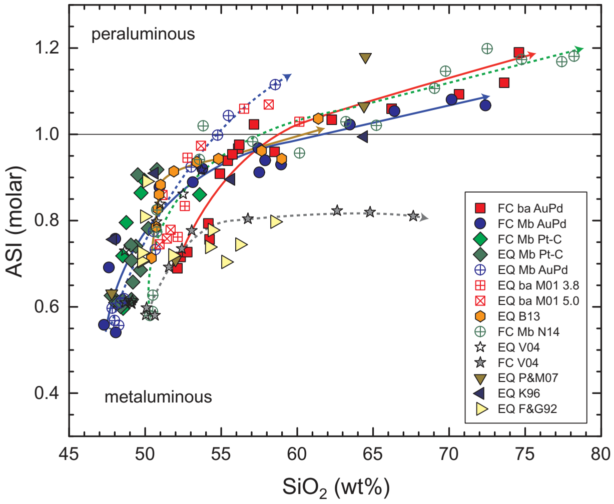

Fig. 20. ASI [alumina saturation index, $Al_2O_3/(CaO+Na_2O+K_2O)$ molar] as a function of SiO_2 (wt %) of experimental liquids from this study and literature data. Symbols and sources of literature data as in Figure 18. Andesitic and more evolved derivative liquids in hydrous systems at 0.7–1.2 GPa are peraluminous.

pseudoternary Ol–Cpx–Qtz diagram (Fig. 21) projected from plagioclase, orthoclase and Fe–Ti–Cr-oxides (Grove *et al.*, 1992; Grove, 1993). Equilibrium and fractional crystallization experiments show significant differences for both starting compositions. The first steps of fractional crystallization of the basaltic andesite experiments are dominated by crystallization of opx and subsequent opx + cpx. The liquid line of descent (LLD) moves towards the Cpx-corner but turns away from the Ol–Cpx side-line when cpx joins the liquidus. Increasing cpx fractionation drives the LLD toward the Ol–Qtz side-line, and concomitant cpx and amph fractionation drives the liquids into the corundum-normative field (negative cpx component). The onset of amphibole crystallization coincides with a branching peritectic relationship of the form opx (+ cpx) + liquid → amphibole marked by the disappearance of opx and reduced cpx crystallization (Fig. 5a). Further evolution is dictated by amphibole and garnet fractionation driving the liquids towards the Qtz apex where a slightly peraluminous rhyolite is obtained. The liquid compositions of the equilibrium crystallization experiments (Müntener *et al.*, 2001) are first driven towards the Ol–Cpx sideline by opx crystallization and then turn towards the Ol–Qtz sideline when cpx becomes the dominant solid phase, crossing the Ol–Qtz tieline around 1110°C. Pyroxene and finally amph crystallization drives the liquids towards intermediate corundum-normative compositions.

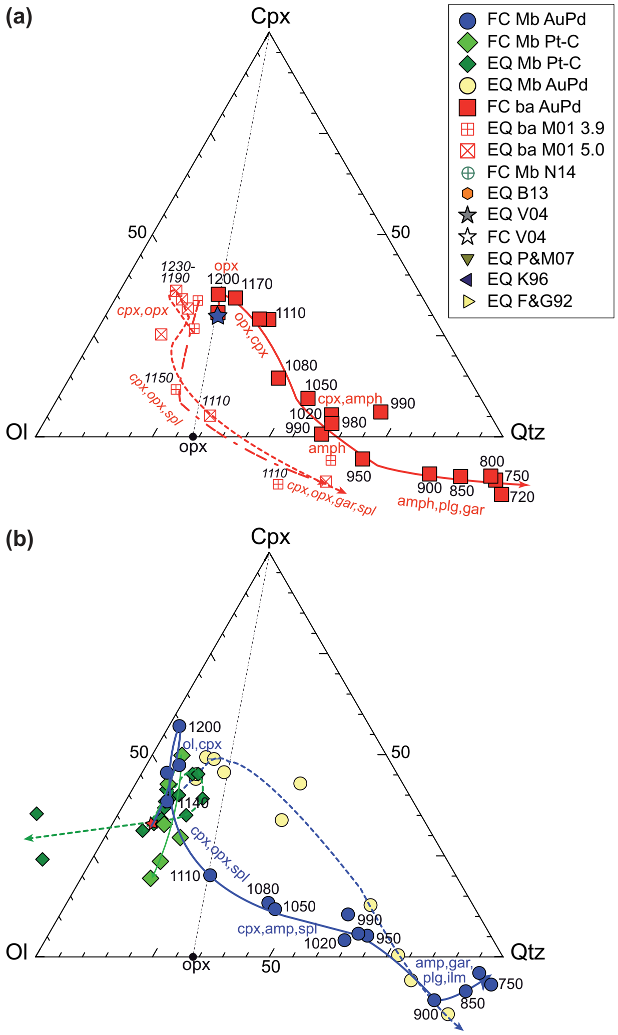

Fig. 21. Normative molecular, pseudoternary olivine (Ol)–clinopyroxene (Cpx)–quartz (Qtz) diagram (Grove *et al.*, 1992; Grove, 1993) projected from plagioclase, orthoclase and Fe–Ti–Cr oxide for experimental liquids (glass). Labels denote run temperatures and coexisting solid assemblages for (a) experiments on high-Mg basaltic andesite (ba series, 85-44) including equilibrium crystallization experiments at 1·2 GPa with 3·8 and 5·0 wt % H_2O after Müntener *et al.* (2001), and (b) high-Mg basalt series (Mb, RC158c). Negative cpx coordinates correspond to corundum-normative (peraluminous) liquids. Symbols and sources of literature data are as in Fig. 18. (For discussion see text.)

The liquid evolution of the high-Mg basaltic starting material is shown in Fig. 20b. Three evolution paths can be identified: (1) fractional and equilibrium crystallization under oxidizing conditions lead to an evolution towards silica-rich intermediate (and SiO_2-rich, fractional) liquids driven by olivine, cpx and later amphibole crystallization/fractionation. The difference between the two LLDs is the persistence of olivine as a liquidus phase in the equilibrium crystallization experiments to 1000°C with cpx (<1160°C) and amphibole (<1060°C), the final liquids being corundum-normative andesite. The fractional crystallization path evolves along lower normative cpx because of early cpx saturation (>1200°C). The peritectic reaction forming amphibole is cpx + liquid → amph not involving any opx. The lack of opx in this series is most probably a combination of high H_2O content (low silica activity; see also Sisson & Grove, 1993) and high fO_2 reducing opx stability relative to olivine and cpx. The crossover to peraluminous compositions plots at ~75% normative qtz relative to ~65% for the basaltic andesite, most probably owing to enhanced amphibole fractionation. Co-precipitation of amphibole and garnet drives liquids to less corundum-normative compositions between 900 and 750°C. The reduced experiments display very different liquid trends. The equilibrium crystallization experiments (EQ Mb Pt–C) first evolve away from olivine and then sharply turn away from cpx when cpx saturation (1180°C) followed by opx occurs. Olivine is replaced by opx, consistent with the reaction olivine + liquid → opx (Fig. 7c). Because the liquid composition is within the Ol–Opx–Cpx triangle while two pyroxenes fractionate, the liquids are driven away from the Cpx–Opx join towards the Ol–Cpx sideline and become silica-undersaturated trachybasalts to trachyandesites between 1090 and 1060°C, despite the fact that the last two crystallization steps involve amphibole that forms through a different reaction where mainly cpx and olivine is consumed and opx + amph form (cpx + ol + liq → amph + opx). This is mainly attributed to the low fO_2 coupled to elevated CO_2 contents from the reaction of the oxidized starting material with graphite. Elevated silica activity in the liquid stabilizes opx relative to olivine and cpx. Such phase relations have been identified in cumulates in the Southern Adamello massif where large amphiboles in hornblendites contain resorbed olivine and cpx primocrysts coexisting with newly formed (intercumulus) opx and strongly zoned amphibole overgrowth rims (Ulmer *et al.*, 1983). Plagioclase is a late phase in these rocks and is mainly attributed to lower pressure intercumulus crystallization when the crystal mush was brought to shallower levels (Ulmer *et al.*, 1983; Blundy & Sparks, 1992; Nimis & Ulmer, 1998). The fractional crystallization experiments under reducing, H_2O-poor (2 wt %) conditions first show an evolution away from the Ol-apex when olivine is the liquidus phase, turn 180° when cpx and minor opx dominate and move towards the Ol–Qtz side-line and sharply turn in the last fractionation step when abundant garnet occurs moving away from Ol.

Phase diagrams for fractionating hydrous magmas at lower crustal conditions

Compositions of synthesized liquids of fractional crystallization experiments along with cpx, opx, hbl and garnet are plotted on the pseudoternary Ol–Cpx–Qtz diagram (Grove *et al.*, 1992; Grove, 1993). Because each experiment uses new starting material, each melt coexisting with crystals is connected with a tieline to its starting composition. Arrows within mineral stability fields indicate compositional variations with decreasing temperature. The two different experimental series show some systematic differences with respect to their evolution along the liquid line of descent. The early evolution of the basaltic andesite (Fig. 22a) is tightly constrained by the two-pyroxene cotectic down to 1080°C. At 1050°C and lower temperatures two pyroxenes cease to coexist and the further crystallization path is determined by a distributary peritectic forming amphibole: cpx + liq → amph or opx + liq → amph. The cpx–amphibole cotectic line was mapped out by slightly varying the starting material and several runs between 990 and 950° formed amphibole only as the liquidus phase. But as the liquids evolve further garnet + amph + plg was stable instead of opx + amphibole at temperatures lower than 900°C, indicating that in the corundum-normative field the lower branch of the amphibole stability field is defined by amphibole + garnet. This means that the field of opx + amph is rather restricted despite the poorly defined grt + amph cotectic. Finally, at the lowest temperature, quartz is stable together with amphibole.

The evolution of the high-Mg basalt is slightly different (Fig. 22b). During the early steps between 1200 and 1140°C the olivine–cpx cotectics is poorly constrained, probably owing to a change of the Mg# from 0·6 to 0·48 during the early stages of fractionation. Decreasing Mg# favors cpx over olivine, thereby expanding the clinopyroxene phase field. Coprecipitation of cpx + spl followed by cpx + opx + spl between 1110 and 1080°C drives the liquids to the right of the cpx–opx tieline, but as liquids further evolve at 1050°C opx disappears and is replaced by hornblende, indicating a similar reaction relationship opx + liq → hbl to that for the basaltic andesite. The further evolution between 1020 and 950°C is characterized by cpx + hbl-saturated liquids. Although there is some variability with respect to starting compositions and measured liquids (because of a combination of some Fe loss and compositional heterogeneity of the starting materials) the cpx–amph boundary is similar to the one from the basaltic andesite. As liquids develop down temperature to dacitic compositions, garnet appears together with amphibole + plagioclase, again suggesting that the amph + opx cotectics is rather restricted. It should be noted that experiments below 950°C saturated in garnet + plagioclase + amphibole are weakly corundum-normative dacitic liquids. The lack of hornblende in some of the experiments below 900°C could be due to small variations in the synthesized material and to different H_2O contents in the liquids.

The results from the two different starting materials show that the formation of hornblende at lower crustal conditions is mainly controlled by the distributary peritectic reaction cpx + opx + liq → hbl. In both cases the cpx + hbl cotectic line is substantially larger than the opx + amph cotectics, which is replaced by amph + garnet at temperatures below ~900°C. This also indicates that garnets are likely to coexist with weakly corundum-normative dacitic liquids at 1·0 GPa conditions corresponding to the lowermost crust. A comparison of garnet compositions indicates that they are compositionally similar for both starting materials, illustrating that fractionation at 1·0 GPa in the lower crust produces dacites that might be garnet saturated. At the onset of garnet saturation, liquids have Mg# between 0·4 and 0·45. A comparison with other experimental studies in the pressure range of 0·9–1·2 GPa indicates that garnet

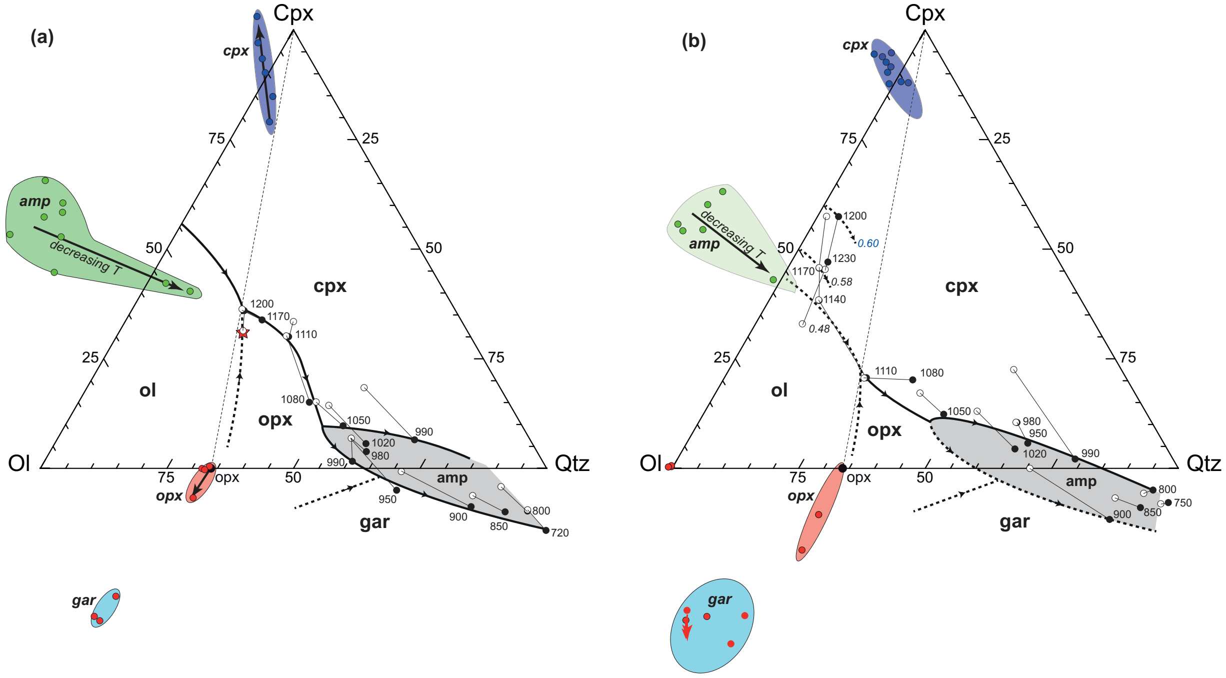

Fig. 22. Pseudo-ternary diagrams illustrating the liquid line of descent of basaltic andesite (a) and high-Mg basalt (b) together with coexisting minerals. Ol, olivine; Cpx, clinopyroxene; Qtz, quartz; Opx, orthopyroxene; gar, garnet; amp, amphibole. Arrows in mineral compositional fields indicate evolution with decreasing temperature. Open circles (starting material) and filled circles (experimental liquids) are connected with a tie-line. Dotted lines indicate approximate phase boundaries. Experiments with Fe loss >20% are not reported.

saturation is common at 1·2 GPa (e.g. Müntener *et al.*, 2001; Alonso-Perez *et al.*, 2009), but rare at pressures of 0·9 and lower. Liquid compositions and/or fO_2 might be critical to stabilize garnet at pressure below 1·0 GPa (e.g. Alonso-Perez *et al.*, 2009; Blatter *et al.*, 2017). Garnet saturation at 1·0 GPa might provide a natural upper limit for the peraluminosity of silicate liquids derived from fractionation in the lower crust.

A comparison of experimentally derived liquids with natural data from the Cascades and Adamello

Most plutonic and volcanic systems that cover a range of compositions from basalt to rhyolite provide evidence for complex histories with multiple generations of normally and reversely zoned crystals and mingling and mixing between diverse magmas (e.g. Eichelberger, 1975; Blundy & Sparks, 1992; Grove *et al.*, 2005). It is therefore instructive to compare natural datasets with experimentally derived liquids. We illustrate the chemical data from the Cascades volcanic rocks (Du Bray *et al.*, 2006) and the Adamello plutonic rocks (Ulmer *et al.*, 1983; Hürlimann *et al.*, 2016) in binary diagrams using MgO and the major oxides SiO_2, CaO, Al_2O_3 and TiO_2 (Fig. 23). The highly systematic variations in melt composition are evidence that the experimentally derived liquids are sufficiently close to natural compositions. There are subtle differences between the natural liquids and the experimentally derived liquids. In MgO vs SiO_2 and CaO diagrams the natural liquids closely follow the fractional crystallization experiments to about 4–5 wt % MgO. Below 4 wt % MgO the fractional crystallization experiments at 1·0 GPa follow different trajectories and the natural data are better represented by lower pressure experiments (e.g. Blatter *et al.*, 2013; Nandedkar *et al.*, 2014). It should be noted that none of the natural datasets follow simple linear trends between 10 and 0 wt % MgO, precluding simple mixing of basalt and rhyolitic liquids to explain intermediate compositions. The similarity between experimental liquids and natural data suggests that most liquids or rock providing unequivocal evidence for mixing are formed from rather similar compositions, so that magma mixing at shallow pressures cannot be resolved by CaO and SiO_2.

A different picture emerges from the evaluation of MgO vs TiO_2 (Fig. 23c). Whereas the Adamello data do not show any values exceeding 1·5 wt % TiO_2, the Cascades data reach values up to 3 wt %. This can be explained by the ubiquitous evidence for (H_2O-poor) arc tholeiites in the Cascades, which follow differentiation trends dominated by early plagioclase saturation, similar to anhydrous experiments (e.g. Grove *et al.*, 1992; Villiger *et al.*, 2004, 2007).

Although experimental liquids synthesized in this study evolve similarly to subduction-zone magmas in many respects, additional processes may be discussed by evaluating MgO vs Al_2O_3 (Fig. 23d). At 5 wt % MgO, the Al_2O_3 values of a part of the Adamello data (Val Fredda series) closely follow the high-pressure experimental trajectories, whereas all other Adamello data

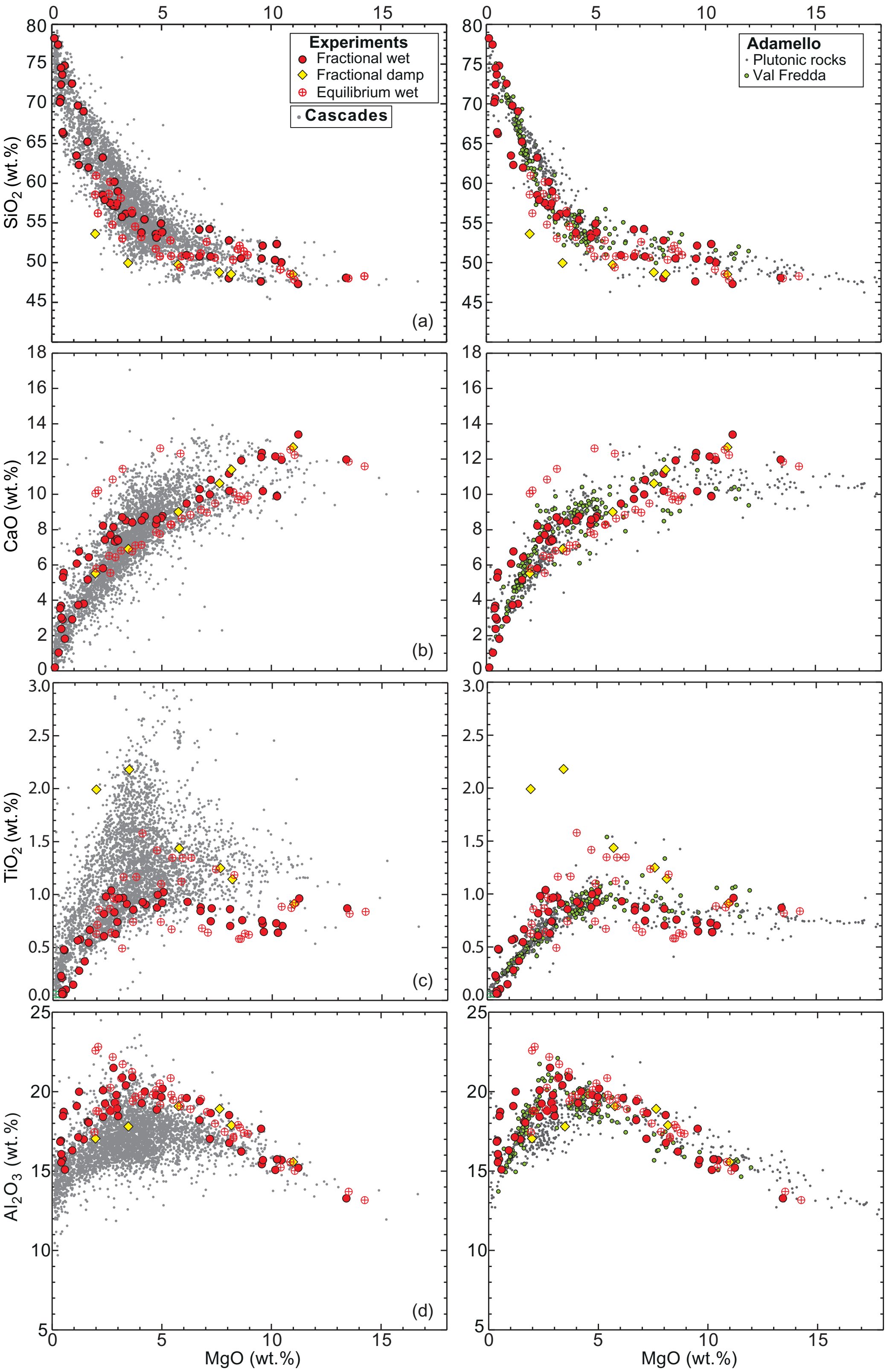

Fig. 23. Experimental liquid compositions compared with volcanic rocks from the Cascades (Du Bray *et al.*, 2006) and plutonic rocks from Adamello (Macera *et al.*, 1983; Ulmer *et al.*, 1983; Blundy & Sparks, 1992; Hürlimann *et al.*, 2016; P. Ulmer, unpublished data) plotted in wt % oxides. (a) MgO vs SiO_2; (b) MgO vs CaO; (c) MgO vs TiO_2; (d) MgO vs Al_2O_3. (For discussion, see text.)

follow the lower pressure experimental data. This difference between the Val Fredda series and all other Adamello data was noted previously (e.g. Ulmer *et al.*, 1983; Blundy & Sparks, 1992) and indicates that both high- and low-pressure fractionation control the evolution of Adamello plutonic rocks. The Cascades data show a different evolution and the majority of data plot below the experimental trends, raising the possibility that mixing plays a more important role than illustrated by CaO and SiO_2. It is important to note, however, that all the experimental series represent isobaric crystallization experiments, whereas natural liquids such as those for the Cascades probably result from polybaric crystallization (e.g. Grove *et al.*, 2005). Near-liquidus phase relations in a decompressing magma (or decreasing H_2O) indicate that the stability of plagioclase increases (e.g. Blundy & Cashman, 2001). This will probably lead to saturation in plagioclase preventing further enrichment of Al_2O_3 and could explain why peraluminous liquids are rare in natural datasets (e.g. Blatter *et al.*, 2013). In addition to mixing, the Cascades trend thus could also indicate an important role for polybaric fractionation during decompression, an interesting further avenue for experimental studies.

CONCLUSIONS

This study reports several series of experiments conducted at 1·0 GPa to evaluate and quantify the liquid lines of descent of calc-alkaline to tholeiitic, hydrous, subduction-related primary mantle magmas by equilibrium and fractional crystallization. The most pertinent results are as follows.

1. To produce intermediate andesitic/tonalitic derivative magmas from primary mantle melts, 40–80% of ultramafic cumulates have to be extracted. The amount is controlled by the extraction depth and composition of primary mantle melt and the process of crystallization. Fractional crystallization of Mg-rich basalt requires 15% of dunitic cumulates, followed by 45% of pyroxenite (cpx dominated) and 5% of cpx-hornblendite, whereas a primary basaltic andesite requires 30% of websterite followed by 10% cpx-hornblendite. Equilibrium crystallization under both oxidizing (NNO + 2) and reducing (graphite-saturated) conditions reaches intermediate andesite (high-fO_2) to trachy-basaltic (low-fO_2) liquids close to 1000°C after 80% crystallization of dunite, pyroxenites (cpx-dominated) and hornblendites.
2. Oxygen fugacity (fO_2) of hydrous, primitive, mantle-derived magmas increases through crystallization-differentiation owing to the significant expansion of the olivine (and to a lesser extent the cpx) stability field (>250°C, 1280–1000°C) relative to less hydrous magmas, resulting in efficient depletion in ferrous iron and a concomitant increase of ferric iron. The resulting fO_2 of the coexisting basaltic liquids increases by more than 3 log units from about NNO + 2 to NNO + 5·5 over the temperature range >1200–1040°C in the case of an oxidized starting composition, and increases by about 1·8 log units from NNO – 0·3 (= FMQ) to NNO + 1·5 for a primary magma in equilibrium with (pristine) asthenospheric mantle, offering an explanation for the more oxidized character of hydrous arc magmas as opposed to low-H_2O tholeiitic magmas where the olivine-stability field at similar conditions is much reduced (<70°C, 1300–1230°C). Enhanced amphibole fractionation at high pressure with respect to magnetite is consistent with the generally higher oxidation state of hydrous arc magmas leaving the lower crust.
3. Crystallization from andesite to rhyolite is controlled by amphibole + garnet + plagioclase extraction, resulting in a similar LLD for both initial starting compositions below 900°C, leaving 16–20 wt % residual liquid at the lowest temperatures (720–750°C). Crystallization under more oxidizing conditions generates peraluminous intermediate to acidic differentiates crossing the metaluminous–peraluminous divide between 56 and 60 wt % SiO_2. Crystallization of up to 11% garnet in the interval andesite–rhyolite will exert a strong control on some trace elements, in particular heavy rare earth elements, characteristic of such highly evolved magmas generated in the lower crust.
4. Melt fractions as a function of temperature display a near linear decrease for Mg basalts and a strongly non-linear evolution for the high-Mg basalt. However, rescaled for basaltic andesite at 1050°C the evolution from andesite to dacite, rhyodacite and rhyolite is very similar with crystallization rates of 14·2 ± 0·6 and 13·5 ± 1·0% per 100°C. The contrasting behavior at higher temperature is controlled by extensive olivine and pyroxenite fractionation with a rate of 36 ± 3% per 100°C followed by a low rate of 7·5 ± 0·8% per 100°C relative to the initial mass for the Mg-rich basalt. In contrast, equilibrium crystallization of the high-Mg basalt under reduced and oxidizing conditions reveals an evolution in three steps: a low rate of olivine-only crystallization (~10 ± 2% per 100°C), followed by a high crystallization rate (30–50% per 100°C) where pyroxenites and pyx-hornblendites form, and a final segment at lowest investigated temperatures (1060–980°C) with again a low crystallization rate (~14% per 100°C). The contrasting behavior of the melt fraction evolution of the different primary magmas potentially controls the compositions of liquids extracted from lower crustal magma reservoirs. The extraction of liquids is most efficient when the rigid percolation threshold (Vigneresse *et al.*, 1996) is reached, where dilute magmatic suspensions transform to crystal mushes around 50% crystallization (Caricchi *et al.*, 2007; Pistone *et al.*, 2013). This indicates that the high-Mg basaltic andesite will reach this threshold around 1000°C where the liquid is a

cpx + amph-saturated peraluminous andesite (58·5 wt % SiO_2), whereas the high-Mg basalt primary magma will reach this threshold around 1100°C with a two-pyroxene + spinel-saturated metaluminous, basaltic-andesite composition. Extraction of basic to intermediate magmas and ascent (decompression) accompanied by further crystallization will lead to a diversity of rising andesitic magmas. The further crystallization is controlled by lower pressure phase equilibria and mixing processes, widely documented in crystallizing plutonic complexes and erupted arc magmas.

5. The compositions of intermediate to SiO_2-rich magmas generated by crystallization differentiation at lower crustal conditions deviate from the bulk of plutonic (e.g. Peninsular batholith, California: Morton *et al.*, 2014); Adamello: Macera *et al.*, 1983) or volcanic (e.g. Cascades: Blatter *et al.*, 2013) rocks typically forming shallow-level complexes at convergent plate margins, in particular by their distinctly peraluminous character. Additional processes are required to obtain the typical, mostly metaluminous compositions of calc-alkaline magmas solidifying to tonalite–granodiorite–granite plutonic rocks or reaching the surface as andesite–dacite–rhyolite. Several mutually not exclusive processes are required, including the following. (a) Mixing of mantle-derived basic to intermediate differentiates (basaltic to basaltic andesite) with acidic magmas originating either from crystallization-differentiation from the former or from partial melting of (lower) crustal lithologies (e.g. Hildreth & Moorbath, 1988; Blatter *et al.*, 2013). (b) Ascent-driven crystallization of derivative basaltic to andesitic magmas (e.g. Blundy & Cashman, 2001) controlled by plag–opx–amph-dominated crystallization and solidification of the cumulates, ultimately forming amphibole-gabbros that are typical of many batholiths worldwide. Near adiabatic decompression of basaltic andesitic magmas inevitably results in saturation in plagioclase, thereby keeping the ascending magmas in the metaluminous field. (c) Crystallization of primary mantle-derived magmas at shallow levels ($\leq$0·4 GPa). Existing phase equilibria on basaltic compositions (e.g. Sisson & Grove, 1993; Blatter *et al.*, 2013; Nandedkar, 2013) reveal that derivative compositions remain metaluminous and compositions generally evolve towards the observed intermediate to acidic rocks. However, the paucity of mafic–ultramafic cumulates in the upper crust that would be necessary to balance the observed tonalite to granite compositions constituting the bulk of the upper crust indicates that this process is volumetrically minor. (d) It has been proposed that magmatic differentiation in arcs dominantly occurs in the lower crust (e.g. Müntener & Ulmer, 2006; in so-called ‘deep crustal hot zones’: Annen *et al.*, 2006). This model explains the general lack of mafic to ultramafic cumulates in the crust by foundering of the lower arc crust directly back into the upper mantle without requiring them to sink through the highly viscous continental crust (Kay & Kay, 1991; Glazner, 1994; Jull & Kelemen, 2001), but requires a fundamental understanding of the processes modifying the basaltic to andesitic derivative liquids upon extraction from their crystal mush in the lower crust and ascent to shallow crustal levels to obtain the observed compositions. Decompression and mixing during magma ascent (e.g. Eichelberger, 1975; Blundy & Cashman, 2001) in transcrustal plumbing systems are the most likely processes that explain arc plutonic and volcanic diversity.

ACKNOWLEDGEMENTS

We would like to acknowledge Eric Reusser for his help in EPMA and SEM analysis and micro-Raman spectroscopy. Constructive reviews by Michel Pichavant, Renat Almeev and Yoshi Tamura, and the editorial handling of Gerhard Wörner helped to sharpen the presentation and are gratefully acknowledged.

SUPPLEMENTARY DATA

Supplementary data for this paper are available at *Journal of Petrology* online.

FUNDING

This work has been supported by several Swiss National Science Foundation grants (20-50661.97, PDFMP2-123097/1, PDTMP2-123074 and 20020-156408/1) and the support of the Herbette foundation.

REFERENCES

Allen, J. C. & Boettcher, A. L. (1978). Amphiboles in andesites and basalts: II. Stability as a function of P–T–fO_2–fH_2O. *American Mineralogist* **63**, 1074–1087.

Alonso-Perez, R., Müntener, O. & Ulmer, P. (2009). Igneous garnet and amphibole fractionation in the roots of island arcs: experimental constraints on andesitic liquids. *Contributions to Mineralogy and Petrology* **157**, 541–558.

Amma-Miyasaka, M. & Nakagawa, M. (2002). Origin of anorthite and olivine megacrysts in island-arc tholeiites: petrological study of 1940 and 1962 ejecta from Miyake-jima volcano, Izu–Mariana arc. *Journal of Volcanology and Geothermal Research* **117**, 263–283.

Annen, C., Blundy, J. D. & Sparks, R. S. J. (2006). The genesis of intermediate to silicic magmas in deep crustal hot zones. *Journal of Petrology* **47**, 505–539.

Arndt, N. T. & Goldstein, S. L. (1989). An open boundary between lower continental crust and mantle: its role in crust formation and crustal recycling. *Tectonophysics* **161**, 201–212.

Atherton, M. P. (1990). The coastal batholith of Peru: the product of rapid recycling of ‘new’ crust formed within rifted continental margin. *Geological Journal* **25**, 337–349.

Baker, M. B., Grove, T. L. & Price, R. (1994). Primitive basalts and andesites from the Mt. Shasta region, N. California:

products of varying melt fraction and water content. *Contributions to Mineralogy and Petrology* **118**, 111–129.

Ballhaus, C. (1993). Redox state of lithospheric and asthenospheric upper mantle. *Contributions to Mineralogy and Petrology* **114**, 331–348.

Blatter, D. L., Sisson, T. W. & Hankins, W. B. (2013). Crystallization of oxidized, moderately hydrous arc basalt at mid- to lower-crustal pressures: implications for andesite genesis. *Contributions to Mineralogy and Petrology* **166**, 861–886.

Blatter, D. L., Sisson, T. W. & Hankins, W. B. (2017). Voluminous arc dacites as amphibole reaction boundary liquids. *Contributions to Mineralogy and Petrology* **172**, 27.

Blundy, J. D. & Cashman, K. (2001). Ascent-driven crystallization of dacite magma at Mount St Helens, 1980–1986. *Contributions to Mineralogy and Petrology* **140**, 631–650.

Blundy, J. D. & Holland, T. J. B. (1990). Calcic amphibole equilibria and a new amphibole–plagioclase geothermometer. *Contributions to Mineralogy and Petrology* **104**, 208–224.

Blundy, J. D. & Sparks, R. S. J. (1992). Petrogenesis of mafic inclusions in granitoids of the Adamello Massif, Italy. *Journal of Petrology* **33**, 1039–1104.

Bohlen, S. R., Essene, E. J. & Boettcher, A. L. (1980). Reinvestigation and application of olivine–quartz–orthopyroxene barometry. *Earth and Planetary Science Letters* **47**, 1–10.

Bose, K. & Ganguly, J. (1995). Quartz–coesite transition revisited—reversed experimental-determination at 500–1200°C and retrieved thermochemical properties. *American Mineralogist* **80**, 231–238.

Botcharnikov, R., Freise, M., Holtz, F. & Behrens, H. (2005). Solubility of C–O–H mixtures in natural melts: new experimental data and application range of recent models. *Annals of Geophysics* **48**, 633–646.

Bowen, N. L. (1928). *The Evolution of the Igneous Rocks*. Princeton, NJ: Princeton University Press.

Bowen, N. L. & Schairer, J. F. (1935). The system MgO–FeO–SiO_2. *American Journal of Science* **29**, 151–217.

Brooker, R. A., Holloway, J. R. & Hervig, R. L. (1998). Reduction in piston-cylinder experiments: the detection of carbon infiltration into platinum capsules. *American Mineralogist* **83**, 985–994.

Buddington, A. F. & Lindsley, D. H. (1964). Iron–titanium oxide minerals and synthetic equivalents. *Journal of Petrology* **5**, 310–357.

Callegari, E. (1983). Geological and petrological aspects of the magmatic activity at Adamello (Northern Italy). *Memorie della Società Geologica Italiana* **26**, 83–104.

Caricchi, L., Ulmer, P. & Peccerillo, A. (2006). A high-pressure experimental study on the evolution of the silicic magmatism of the main Ethiopian Rift. *Lithos* **91**, 46–58.

Caricchi, L., Burlini, L., Ulmer, P., Gerya, T., Vassalli, M. & Papale, P. (2007). Non-Newtonian rheology of crystal-bearing magmas and implications for magma ascent dynamics. *Earth and Planetary Science Letters* **264**, 402–419.

Carmichael, I. S. E. (1991). The redox states of basic and silicic magmas: a reflection of their source regions? *Contributions to Mineralogy and Petrology* **106**, 129–141.

Cawthorn, R. G. & O'Hara, M. J. (1976). Amphibole fractionation in calc-alkaline magma genesis. *American Journal of Science* **276**, 309–329.

Cawthorn, R. G., Strong, D. F. & Brown, P. A. (1976). Origin of corundum-normative intrusive and extrusive magmas. *Nature* **259**, 102–104.

Clemens, J. D., Stevens, G. & Farina, F. (2011). The enigmatic sources of I-type granites: the peritectic connexion. *Lithos* **126**, 174–181.

Dauphas, N., Craddock, P. R., Asimow, P. D., Bennett, V. C., Nutman, A. P. & Ohnenstetter, D. (2009). Iron isotopes may reveal the redox conditions of mantle melting from Archean to present. *Earth and Planetary Science Letters* **288**, 255–267.

Davidson, P. M. & Lindsley, D. H. (1985). Thermodynamic analysis of quadrilateral pyroxenes Part II. Model calculation from experiments and applications to geothermometry. *Contributions to Mineralogy and Petrology* **91**, 390–404.

Dessimoz, M., Müntener, O. & Ulmer, P. (2012). A case for hornblende dominated fractionation of arc magmas: the Chelan Complex (Washington Cascades). *Contributions to Mineralogy and Petrology* **163**, 567–589.

Di Muro, A., Villemant, B., Montagnac, G., Scaillet, B. & Reynard, B. (2006). Quantification of water content and speciation in natural silicic glasses (phonolite, dacite, rhyolite) by confocal microRaman spectrometry. *Geochimica et Cosmochimica Acta* **70**, 2868–2884.

Drummond, M. S. & Defant, M. J. (1990). A model for trondhjemite–tonalite–dacite genesis and crustal growth via slab melting: Archean to modern comparison. *Journal of Geophysical Research* **95**, 21503–21521.

Du Bray, E. A., John, D. A., Sherrod, D. R., Evarts, R. C., Conrey, R. M. & Lexa, J. (2006). Geochemical database for volcanic rocks of the Western Cascades, Washington, Oregon, and California. *US Geological Survey Data Series* **155**, 49.

Eggler, D. H. (1972). Amphibole stability in H_2O-undersaturated calc-alkaline melts. *Earth and Planetary Science Letters* **15**, 28–34.

Eichelberger, J. C. (1975). Origin of andesite and dacite: evidence of mixing at Glass Mountain in California and at other circum-Pacific volcanoes. *Geological Society of America Bulletin* **86**, 1381–1391.

Foden, J. D. & Green, D. H. (1992). Possible role of amphibole in the origin of andesite: some experimental and natural evidence. *Contributions to Mineralogy and Petrology* **109**, 479–493.

Frost, D. J. & Wood, B. J. (1995). Experimental measurements of the graphite C–O equilibrium and CO_2 fugacities at high temperatures and pressure. *Contributions to Mineralogy and Petrology* **121**, 303–308.

Glazner, A. F. (1994). Foundering of mafic plutons and density stratification of continental crust. *Geology* **22**, 435–438.

Goldstein, J. I., Newbury, D. E., Joy, D. C., Lyman, C. E., Echlin, P., Lifshin, E., Sawyer, L. & Michael, J. R. (2003). *Scanning Electron Microscopy and X-Ray Microanalysis*. Berlin: Springer.

Green, T. H. (1980). Island arc and continent building magmatism—a review of petrogenetic models based on experimental petrology and geochemistry. *Tectonophysics* **63**, 367–385.

Grove, T. L. (1993). Corrections to expressions for calculating mineral components in 'Origin of calc-alkaline series lavas at Medicine Lake Volcano by fractionation, assimilation, and mixing' and 'Experimental petrology of normal MORB near the Kane Fracture Zone: 22°–25°N, mid-Atlantic ridge'. *Contributions to Mineralogy and Petrology* **114**, 422–424.

Grove, T. L., Kinzler, R. J. & Bryan, W. B. (1992). Fractionation of mid-ocean ridge basalt (MORB). In: Morgan, J. P., Blackman, D. K. & Sinton, J. M. (eds) *Mantle Flow and Melt Generation at Mid-Ocean Ridges. American Geophysical Union, Geophysical Monograph* **71**, 281–310.

Grove, T. L., Parman, S. W., Bowring, S. A., Price, R. C. & Baker, M. B. (2002). The role of an H_2O-rich fluid component in the generation of primitive basaltic andesites and dacites from the Mt. Shasta region, N. California. *Contributions to Mineralogy and Petrology* **142**, 375–396.

Grove, T. L., Elkins-Tanton, L. T., Parman, S. W., Chatterjee, N., Müntener, O. & Gaetani, G. A. (2003). Fractional crystallization and mantle-melting controls on calc-alkaline differentiation trends. *Contributions to Mineralogy and Petrology* **145**, 515–533.

Grove, T. L., Baker, M. B., Price, R. C., Parman, S. W., Elkins-Tanton, L. T., Chatterjee, N. & Müntener, O. (2005). Magnesian andesite and dacite lavas from Mt. Shasta, northern California: products of fractional crystrallization of H_2O-rich mantle melts. *Contributions to Mineralogy and Petrology* **148**, 542–565.

Hall, L. J., Brodie, J., Wood, B. J. & Carroll, M. R. (2004). Iron and water losses from hydrous basalts contained in $Au_{80}Pd_{20}$ capsules at high pressure and temperature. *Mineralogical Magazine* **68**, 75–81.

Hernlund, J., Leinenweber, K., Locke, D. & Tyburczy, J. A. (2006). A numerical model for steady-state temperature distributions in solid-medium high-pressure cell assemblies. *American Mineralogist* **91**, 295–305.

Hildreth, W. & Moorbath, S. (1988). Crustal contributions to arc magmatism in the Andes of Central Chile. *Contributions to Mineralogy and Petrology* **98**, 455–489.

Holland, T. & Blundy, J. (1994). Non-ideal interactions in calcic amphiboles and their bearing on amphibole–plagioclase thermometry. *Contributions to Mineralogy and Petrology* **116**, 433–447.

Holloway, J. R. & Burnham, C. W. (1972). Melting relations of basalt with equilibrium water pressure less than total pressure. *Journal of Petrology* **13**, 1–29.

Hürlimann, N., Müntener, O., Ulmer, P., Nandedkar, R., Chiaradia, M. & Ovtcharova, M. (2016). Primary magmas in continental arcs and their differentiated products: petrology of a post-plutonic dyke suite in the Tertiary Adamello batholith (Alps). *Journal of Petrology* **57**, 495–534.

Iacono-Marziano, G., Morizet, Y., Le Trong, E. & Gaillard, F. (2012). New experimental data and semi-empirical parameterization of H_2O–CO_2 solubility in mafic melts. *Geochimica et Cosmochimica Acta* **97**, 1–23.

Jagoutz, O., Burg, J.-P., Hussain, S., Dawood, H., Pettke, T., Iiszuka, T. & Maruyama, S. (2009). Construction of the granitoid crust of an island arc part I: geochronological and geochemical constraints from the plutonic Kohistan (NW Pakistan). *Contributions to Mineralogy and Petrology* **158**, 739–755.

Jagoutz, O., Müntener, O., Schmidt, M. W. & Burg, J.-P. (2011). The roles of flux- and decompression melting and their respective fractionation lines for continental crust formation: evidence from the Kohistan arc. *Earth and Planetary Science Letters* **303**, 25–36.

Jakobsson, S. (2012). Oxygen fugacity control in piston-cylinder experiments. *Contributions to Mineralogy and Petrology* **164**, 397–406.

Jenner, F. E., O'Neill, H. S. C., Arculus, R. J. & Mavrogenes, J. A. (2010). The magnetite crisis in the evolution of arc-related magmas and the initial concentration of Au, Ag and Cu. *Journal of Petrology* **51**, 2445–2464.

Jull, M. & Kelemen, P. B. (2001). On the conditions for lower crustal convective instability. *Journal of Geophysical Research* **106**, 6423–6445.

Kägi, R., Müntener, O., Ulmer, P. & Ottolini, L. (2005). Piston-cylinder experiments on H_2O undersaturated Fe-bearing systems: an experimental setup approaching f_{O2} conditions of natural calc-alkaline magmas. *American Mineralogist* **90**, 708–717.

Kawamoto, T. (1996). Experimental constraints on differentiation and H_2O abundance of calc-alkaline magmas. *Earth and Planetary Science Letters* **144**, 577–589.

Kay, R. W. (1978). Aleutian magnesian andesites: melts from subducted oceanic crust. *Journal of Volcanology and Geothermal Research* **4**, 117–132.

Kay, R. W. & Kay, S. M. (1991). Creation and destruction of lower continental crust. *Geologische Rundschau* **80**, 259–278.

Kay, S. M. & Ramos, V. A. (2006). Evolution of an Andean margin: a tectonic and magmatic view from the Andes to the Neuquén Basin (35°–39°S lat.). *Geological Society of America Special Papers* **407**, 1–343.

Keller, C. B., Schoene, B., Barboni, M., Samperton, K. M. & Husson, J. M. (2015). Volcanic–plutonic parity and the differentiation of the continental crust. *Nature* **523**, 301–307.

Kelley, K. A. & Cottrell, E. (2009). Water and the oxidation state of subduction zone magmas. *Science* **325**, 605–607.

Korolyuk, Y. N., Usova, L. V. & Nigmatulina, E. N. (2009). Accuracy in the determination of the compositions of main rockforming silicates and oxides on a JXA-8100 microanalyer. *Journal of Analytical Chemistry* **64**, 1042–1046.

Kress, V. C. & Carmichael, I. S. E. (1991). The compressibility of silicate liquids containing Fe_2O_3 and the effect of composition, temperature, oxygen fugacity and pressure on their redox states. *Contributions to Mineralogy and Petrology* **108**, 82–92.

Kushiro, I. (1972). Effects of H_2O on the composition of magmas formed at high pressures. *Journal of Petrology* **13**, 311–344.

Kushiro, I. (1974). Melting of hydrous upper mantle and possible generation of andesite magma. An approach from synthetic systems. *Earth and Planetary Science Letters* **22**, 294–299.

Kushiro, I. (1975). On the nature of silicate melt and its significance in magma genesis: regularities in the shift of liquidus boundaries involving ol–opx and silica minerals. *American Journal of Science* **275**, 411–431.

Kushiro, I. (1990). Partial melting of mantle wedge and evolution of island arc crust. *Journal of Geophysical Research* **95**, 15929–15939.

Lattard, D., Sauerzapf, U. & Käsemann, M. (2005). New calibration data for the Fe–Ti oxide thermo-oxybarometers from experiments in the Fe–Ti–O system at 1 bar, 1000–1300°C and a large range of oxygen fugacities. *Contributions to Mineralogy and Petrology* **149**, 735–754.

Leake, B. E., Woolley, A. R., Arps, C. E. S., Birch, W. D., Gilbert, M. C., Grice, J. D., Hawthorne, F. C., Kato, A., Kisch, H. J., Krivovichev, V. G., Linthout, K., Laird, J., Mandarino, J. A., Maresch, W. V., Nickel, E. H., Rock, N. M. S., Schumacher, J. C., Smith, D. C., Stephenson, N. C. N., Ungaretti, L., Whittaker, E. J. W. & Guo, Y. Z. (1997). Nomenclature of amphiboles: report of the subcommittee on amphiboles of the International Mineralogical Association, commission on new minerals and mineral names. *American Mineralogist* **82**, 1019–1037.

Lee, C.-T. A., Leeman, W. P., Canil, D. & Li, Z.-X. A. (2005). Similar V/Sc systematics in MORB and arc basalts: implications for the oxygen fugacities of their mantle source regions. *Journal of Petrology* **46**, 2313–2336.

Lee, C. T. A., Cheng, X. & Horodyskyj, U. (2006). The development and refinement of continental arcs by primary basaltic magmatism, garnet pyroxenite accumulation, basaltic recharge and delamination: insights from the Sierra Nevada, California. *Contributions to Mineralogy and Petrology* **151**, 222–242.

Lee, C.-T. A., Luffi, P., Le Roux, V., Dasgupta, R., Albarade, F. & Leeman, W. P. (2010). The Redox state of arc mantle using Zn/Fe systematics. *Nature* **468**, 681–685.

Le Maitre, R. W., Bateman, P., Dudek, A., Keller, J., Lameyre, J., Le Bas, M. J., Sabine, P. A., Schmid, R., Sorensen, H., Streckeisen, A., Woolley, A. R. & Zanettin, B. (1989). *A*

Classification of Igneous Rocks and Glossary of Terms: Recommendations of the International Union of Geological Sciences Subcommission on the Systematics of Igneous Rocks. Oxford: Blackwell Scientific.

Le Voyer, M., Rose-Koga, E. F., Shimizu, N., Grove, T. L. & Schiano, P. (2010). Two contrasting H_2O-rich components in primary melt inclusions from Mount Shasta. *Journal of Petrology* **51**, 1571–1595.

Lindsley, D. H. (1983). Pyroxene thermometry. *American Mineralogist* **68**, 477–493.

Luth, R. W. (1989). Natural versus experimental control of oxidation state—effects on the composition and speciation of C–O–H-fluids. *American Mineralogist* **74**, 50–57.

Macera, P., Ferrara, G., Pescia, A. & Callegari, E. (1983). A geochemical study on the acid and basic rocks of the Adamello Batholith. *Memorie della Società Geologica Italiana* **26**, 223–259.

Meen, J. K. (1987). Formation of shoshonites from calcalkaline basalt magmas: geochemical and experimental constraints from the type locality. *Contributions to Mineralogy and Petrology* **97**, 333–351.

Melekhova, E., Annen, C. & Blundy, J. (2013). Compositional gaps in igneous rock suites controlled by magma system heat and water content. *Nature Geoscience* **6**, 385–390.

Mercier, M., Di Muro, A., Giordano, D., Metrich, N., Lesne, P., Pichavant, M., Scaillet, B., Clocchiatti, R. & Montagnac, G. (2009). Influence of glass polymerisation and oxidation on micro-Raman water analysis in alumino-silicate glasses. *Geochimica et Cosmochimica Acta* **73**, 197–217.

Miyashiro, A. (1974). Volcanic rock series in island arcs and active continental margins. *American Journal of Science* **274**, 321–355.

Morton, D. M., Miller, F. K., Kistler, R. W., Premo, W. R., Lee, C.-T. A., Langenheim, V. E., Wooden, J. L., Snee, L. W., Clausen, B. L. & Cossette, P. (2014). Framework and petrogenesis of the northern Penninsular Ranges Batholith, Southern California. In: Morton, D. M. & Miller, F. K. (eds) *Peninsular Ranges Batholith, Baja and Southern California. Geological Society of America, Memoirs* **211**, 61–143.

Munoz-Espadas, M.-J., Lunar, R. & Martinez-Frias, J. (2000). The garnet placer deposit from SE Spain: industrial recovery and geochemical features. *Episodes* **23**, 266–269.

Müntener, O. & Ulmer, P. (2006). Experimentally derived high-pressure cumulates from hydrous arc magmas and consequences for the seismic velocity structure of lower arc crust. *Geophysical Research Letters* **33**, L21308.

Müntener, O. & Ulmer, P. (2018). Arc crust formation and differentiation constrained by experimental petrology. *American Journal of Science* **318**, 64–89.

Müntener, O., Kelemen, P. B. & Grove, T. L. (2001). The role of H_2O during crystallization of primitive arc magmas under uppermost mantle conditions and genesis of igneous pyroxenites: an experimental study. *Contributions to Mineralogy and Petrology* **141**, 643–658.

Nandedkar, R. H. (2013). *Evolution of Hydrous Mantle-Derived Calc-Alkaline Liquids by Fractional Crystallization at 0·7 and 0·4 GPa—An Experimental Study*. PhD thesis, ETH Zurich, 232 pp.

Nandedkar, R. H., Ulmer, P. & Müntener, O. (2014). Fractional crystallization of primitive, hydrous arc magmas: an experimental study at 0·7 GPa. *Contributions to Mineralogy and Petrology* **167**, 101.

Nandedkar, R. H., Hürlimann, N., Ulmer, P. & Müntener, O. (2016). Experimental amphibole–melt trace element partitioning in andesitic to rhyolitic systems at mid- to lower crustal conditions. *Contributions to Mineralogy and Petrology* **171**, 71.

Newman, S. & Lowenstern, J. B. (2002). VolatileCalc: a silicate melt–H_2O–CO_2 solution model written in Visual Basic for Excel. *Computers and Geosciences* **28**, 597–604.

Nimis, P. & Ulmer, P. (1998). Clinopyroxene geobarometry of magmatic rocks Part 1: an expanded structural geobarometer for anhydrous and hydrous, basic and ultrabasic systems. *Contributions to Mineralogy and Petrology* **133**, 122–135.

Parkinson, I. J. & Arculus, R. J. (1999). The redox state of subduction zones: insights from arc-peridotites. *Chemical Geology* **160**, 409–423.

Pichavant, M. & Macdonald, R. (2007). Crystallization of primitive basaltic magmas at crustal pressures and genesis of the calc-alkaline igneous suite: experimental evidence from St Vincent, Lesser Antilles arc. *Contributions to Mineralogy and Petrology* **154**, 535–558.

Pichavant, M., Martel, C., Bourdier, J.-L. & Scaillet, B. (2002). Physical conditions, structure, and dynamics of a zoned magma chamber: Mount Pelée (Martinique, Lesser Antilles Arc). *Journal of Geophysical Research* **107**, doi: 10.1029/2001JB000315.

Pistone, M., Caricchi, L., Ulmer, P., Reusser, E. & Ardia, P. (2013). Rheology of volatile-bearing crystal mushes: mobilization vs. viscous death. *Chemical Geology* **345**, 16–39.

Rapp, R. P. & Watson, E. B. (1995). Dehydration melting of metabasalt at 8–32 kbar: implications for continental growth and crust–mantle recycling. *Journal of Petrology* **36**, 891–931.

Ratajeski, K. & Sisson, T. W. (1999). Loss of iron to gold capsules in rock-melting experiments. *American Mineralogist* **84**, 1521–1527.

Ridolfi, F. & Renzulli, A. (2012). Calcic amphiboles in calc-alkaline and alkaline magmas: thermobarometric and chemometric empirical equations valid up to 1,130°C and 2.2 GPa. *Contributions to Mineralogy and Petrology* **163**, 877.

Rudnick, R. L. (1995). Making continental crust. *Nature* **378**, 571–578.

Schwandt, C. S. & McKay, G. A. (2006). Minor- and trace-element sector zoning in synthetic enstatite. *American Mineralogist* **91**, 1607.

Sisson, T. W. & Bronto, S. (1998). Evidence for pressure-release melting beneath magmatic arcs from basalt at Galunggung, Indonesia. *Nature* **391**, 883–888.

Sisson, T. W. & Grove, T. L. (1993). Experimental investigations of the role of H_2O in calc-alkaline differentiation and subduction zone magmatism. *Contributions to Mineralogy and Petrology* **113**, 143–166.

Sisson, T. W., Ratajeski, K., Hankins, W. B. & Glazner, A. F. (2005). Voluminous granitic magmas from common basaltic sources. *Contributions to Mineralogy and Petrology* **148**, 635–661.

Taylor, S. R. & White, A. J. R. (1965). Geochemistry of andesites and the growth of continents. *Nature* **208**, 271–273.

Thompson, A. B., Matile, L. & Ulmer, P. (2002). Some thermal constraints on crustal assimilation during fractionation of hydrous, mantle-derived magmas with examples from central Alpine batholiths. *Journal of Petrology* **43**, 403–422.

Ulmer, P. (1986). Basische und ultrabasische Gesteine des Adamello (Provinzen Brescia und Trento, Norditalien). Dissertation, ETH Zürich, No. 8105.

Ulmer, P. (1988). High-pressure phase equilibria of calc-alkaline picrobasalt: implications for the genesis of calc-alkaline magmas. *Annual Report of the Director, Geophysical Laboratory, Carnegie Institution of Washington 1987–1988* 28–35.

Ulmer, P. (1989). The dependence of Fe^{2+}–Mg cation-partitioning between olivine and basaltic liquid on pressure, temperature and composition; an experimental study. *Contributions to Mineralogy and Petrology* **101**, 261–273.

Ulmer, P. & Luth, R. W. (1991). The graphite–COH fluid equilibrium in *P*, *T*, fO_2 space: an experimental determination to 30 kbar and 1600°C. *Contributions to Mineralogy and Petrology* **106**, 265–272.

Ulmer, P., Callegari, E. & Sonderegger, U. (1983). Genesis of the mafic and ultramafic rocks and their genetical relations to the tonalitic–trondhjemitic granitoids of the southern part of the Adamello batholith (Northern Italy). *Memorie della Società Geologica Italiana* **26**, 171–222.

Vigneresse, J. L., Barbey, P. & Cuney, M. (1996). Rheological transitions during partial melting and crystallization with application to felsic magma segregation and transfer. *Journal of Petrology* **37**, 1579–1600.

Villiger, S., Ulmer, P., Müntener, O. & Thompson, A. B. (2004). The liquid line of descent of anhydrous, mantle-derived, tholeiitic liquids by fractional and equilibrium crystallization—an experimental study at 1·0 GPa. *Journal of Petrology* **45**, 2369–2388.

Villiger, S., Ulmer, P. & Müntener, O. (2007). Equilibrium and fractional crystallization experiments at 0.7 GPa; the effect of pressure on phase relations and liquid compositions. *Journal of Petrology* **48**, 159–184.

Waters, L. E. & Lange, R. A. (2015). An updated calibration of the plagioclase–liquid hygrometer–thermometer applicable to basalts through rhyolites. *American Mineralogist* **100**, 2172–2184.

Zhang, Y. (1999). H_2O in rhyolitic glasses and melts: measurement, speciation, solubility, and diffusion. *Reviews of Geophysics* **37**, 493–516.